Spectra and Dynamics of Calcium Monochloride

by

Jason Otto Clevenger

Submitted to the Department of Chemistry
in partial fulfillment of the requirements for the degree of

Doctor of Philosophy in Physical Chemistry

at the

MASSACHUSETTS INSTITUTE OF TECHNOLOGY

February 2002

Author . . . .
Department of Chemistry
February 1, 2002

Certified by . . . .
Robert W. Field
Haslam and Dewey Professor of Chemistry
Thesis Supervisor

Accepted by . . . .
Robert W. Field
Chairman, Department Committee on Graduate Students

This doctoral thesis has been examined by a Committee of the Department of Chemistry that included

Professor Robert J. Silbey ——————————————————————————
(Chairman)

Professor Keith A. Nelson ——————————————————————————

Professor Robert W. Field ——————————————————————————
(Thesis Supervisor)

Spectra and Dynamics of Calcium Monochloride

by

Jason Otto Clevenger

Submitted to the Department of Chemistry
on February 1, 2002, in partial fulfillment of the
requirements for the degree of
Doctor of Philosophy in Physical Chemistry

Abstract

The alkaline earth monohalides (MX) represent an ideal molecule for studying molecular Rydberg states, as they are well described as by an ion-core containing two closed shell atomic ions (M^{2+},X^-) and an unpaired electron. The spectra and dynamics of Rydberg states allows the testing of theories of electronic structure and nuclear-electronic energy exchange. This thesis presents the results of a series of experimental studies on the least well-studied MX molecule, CaCl (calcium monochloride). The majority of these investigations were conducted in a specialized molecular beam apparatus described in some detail.

The spectroscopy of CaCl is challenging because of the onset of predissociation at $n^* \sim 3$. The reduction in ionization quantum yield associated with the predissociation greatly reduces our ability to record Rydberg state spectra, but provides opportunities to model the predissociation processes with the results of observed states. Such a model was accomplished with the $^2\Sigma^+$ repulsive state via a linewidth analysis, and with the $^2\Pi$ state with a qualitative model.

The experiments described here represent a significant step to understanding the dynamics of MX Rydberg states from a frequency-domain perspective, and should allow the development of future studies to completely characterize the predissociative processes in CaCl.

Thesis Supervisor: Robert W. Field
Title: Haslam and Dewey Professor of Chemistry

Acknowledgments

"I would like to thank the Nobel Academy..." oh, wait, wrong speech... As with most of my friends and colleagues, I waited until the very last minute to write this part of my thesis. While in many respects it is a sign of sloth and laziness, it also represents one of the most difficult passages of the entire work. I have so many people to thank, and I am sure that I will forget some. Nevertheless, here I go:

First of all, I would like to thank my advisor, Prof. Robert W. Field, for his undying enthusiasm for science and his unwavering support. His trust allowed me to rebuild the lab after the dark days of October 1996 with almost complete freedom. I can't imagine anyone else trusting a second year student with almost a million dollars of insurance money, or anyone who loves country music as much as he does.

I would like to thank the past members of the Field group with whom I have had regrettably brief interactions: Jon O'Brien, Jonathan Bloch, and Stephani Solina. Kevin Cunningham also counts as a 'past member', but our interactions were not necessarily brief, nor are they in the past, since we will be both working at Applied Materials. I admire Kevin's determination to do the work he wanted to do, in his own way.

Recent graduates of the group have been reminding me how much fun is in the real world. I wish Selen Altunata the best success in Washington, and I wish Michelle Silva the best in Colorado and everywhere else her brilliant mind takes her. Michelle and I shared a lot of the same stresses in graduate school, and I appreciate her friendship in innumerable ways.

To the current members of the group, I extend my warmest regards and the sincere wish that they have unimpeded progress to the exit door. Xing and I have spent many, many evenings in the lab wondering why things don't work the way they should, and without his help this thesis would not have turned out the same way. Not only do I respect Richard Duan's appetite for Boston's hottest chicken, but I respect him as a scientist and a person. Ryan Thom's promising career as a Jesuit may have been compromised in part by my presence, but nevertheless I have never met a man with

more broad-ranging interests or more single-minded focus, and I am impressed by him more each passing day. Serhan's incredible physical insight is only matched by his affinity for rum, and that alone is worthy of respect, and I expect to visit him someday in the Aegean. While Jeff, Kyle, and Dave have only just joined the group, I have seen enough of them to know that they will be tremendously successful here and beyond the hallowed halls of MIT. And even though he isn't an official member of the group, I send my best wishes to Scott Witonsky. We have weathered a number of changes in the basement of buildings 2 and 6.

A special note goes out to Herr Robert Seiler of ETH in Switzerland, who knows more about Star Trek than anyone I've ever met. I hope to meet up with him during his travels throughout the world, particularly in a few select countries in Asia. Er ist ein ganz toll Schmuck.

Another special mention must go to one of the world's most infamous postdocs, Dr. Sergey Panov. His genius was the main enabler of the experiments described in this thesis. His talent for design and construction is unsurpassed in my mind, and I learned a tremendous amount during his three year stay here. His love of Linux was infectious enough to cause me sleepless nights learning Red Hat apocrypha. Best of luck to him and his family.

I have been tremendously fortunate to have had interactions with a number of scientists who served as mentors or guides through my journey at the Institute. Dr. Steven Coy, Dr. Yaoming Liu, Dr. Mike McCarthy, Dr. Zygmunt Jakubek, Prof. Rob Lipson, Prof. Li Li, Prof. Christian Jungen, Prof. Frederic Merkt and Prof. Anthony Merer all deserve tremendous thanks.

For my former roommates at 148 Spring Street (Geoff, Tim, and Joe), I extend best wishes for their success. It goes without saying that I appreciate my previous and current roommate, Patricio Mendez, for not only being a fine person but a really great friend. My stay at the Insitute would have been very, very different without his presence, and through the years I not only got to know an Argentine poet but a true scholar and entrepreneur. I am sure he will be a tremendous success in whatever he attempts.

Any acknowledgement section worth its dot pitch will contain a reference to formative parental influence, and this will be no exception. To Elmo and Gloria, I thank them for their tremendous support and forbearance through this long process. It must come as a tremendous relief that now that I'm fully educated, I can pay my own car insurance. Thanks for believing in me.

Last, and certainly not least, I have to acknowledge the presence of my fiancee', Charmaine Clyde, in my life. While she has not yet had the chance to have the career that she wants, she nevertheless has graced my life through her courage and perseverance through incredible odds. Her story is inspirational, and her love is felt every day.

For My Parents and Charmaine

Contents

List of Figures

16

17

19

List of Tables

Chapter 1

Introduction

The spectroscopy of Rydberg states has a rich and varied history, beginning with the development of the simple formula by Balmer in 1885 which described the emission spectrum of hydrogen. That formula, now known as the Rydberg equation, sparked the birth of quantum mechanics. Rydberg spectroscopy of atoms, and increasingly molecules, is still important today as a fundamental tool for understanding the physical properties of matter.

The most salient feature of Rydberg spectroscopy is the existence of an infinite series of atomic (and molecular) states, which can be related to the simple electronic structure of the hydrogen atom by the Rydberg formula:

$$E_{nl\lambda} = IP - (\frac{\Re}{n - \mu_{l\lambda}})^2, n - \mu_{l\lambda} \equiv n^* \tag{1.1}$$

where IP is the ionization potential, $\Re$ is the universal (though weakly mass-dependent) Rydberg constant, n is the principal quantum number, and $\mu_{l\lambda}$ is the quantum defect. The existence of $\mu_{l\lambda}$ allows the Rydberg formula to be used for molecules as well as many-electron atoms. The quantum defect has an explicit dependence on l (the orbital angular momentum quantum number) and λ (the projection of the orbital angular angular momentum). It can also be a slowly varying function of energy [7]. The quantum defects, then, contain all of the information necessary to describe the electronic structure and dynamics of Rydberg states of any atom or molecule [8].
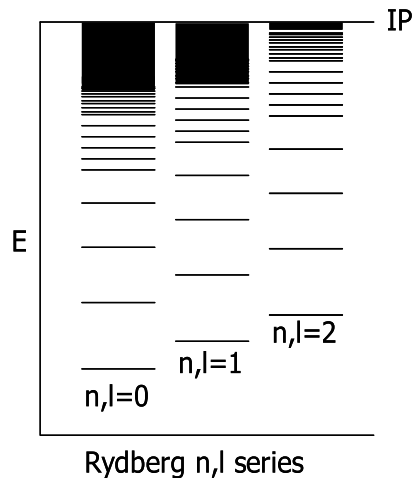
Figure 1-1: Schematic representation of Rydberg series converging on the ionization limit.

The Rydberg states of the alkaline earth monohalide molecules in particular have been extensively studied by spectroscopic and theoretical means [9–16]. These molecules have highly polar molecular-ion cores (MX$^+$), the properties of which can be understood in terms of two closed-shell polarizable atomic ions, M^{2+} and X$^-$. While the properties of the valence states of these molecules have been treated by Rice *et al.* using a ligand field model [17, 18] and by Törring *et al.* [19] using an electrostatic polarization model, the strongly polarized core mixes l even for nominally low-l "valence" states. Neither model can thus provide a complete description of the spectroscopic data, as often higher order l mixing must be considered, i.e. as a $s \sim p \sim d \sim f \sim g$ "supercomplex" [14, 15, 20].

While the low-l states are strongly mixed in the MX molecules, the picture changes for higher values of l. This may be understood from the effective potential of the hydrogen atom, which comes from the radial portion of the hydrogen atom Schrödinger equation:

$$V_{eff}(r) = -\frac{1}{r} + \frac{l(l+1)}{2r^2}. \tag{1.2}$$

The term in $1/r^2$ acts as a centrifugal barrier preventing the hydrogen electron from coming close to the core (in this case, a proton) as l increases. This is evident in Fig. 1-2, where the lowest n values for each l are shown up to $l = 4$. This picture can be directly superimposed on the MX molecules, of which CaCl is the main subject in this thesis. As l increases beyond a critical value (the effective radius of the CaCl$^+$ ion-core), the Rydberg electron is excluded from direct interaction with the core. This distinction defines two classes of Rydberg states, *core-penetrating* (low l, large $\mu_{l\lambda}$) and *core-nonpenetrating* (high l, small $\mu_{l\lambda}$). The core-penetrating Rydberg states are the ones most likely to be directly observed by direct or two step excitation from the electronic ground state, as it is difficult to reach high values of l with optical excitation steps alone (due to the fact that a photon carries a single unit of orbital angular momentum). However, since 'intermediate' values of l are often mixed in with lower-l components, core-nonpenetrating states can be accessed in some cases by direct excitation (e.g. the f-complex in CaF [21]) or by perturbations with core-penetrating levels, which accidentally lie near integer-n* [20, 21]. The core-nonpenetrating states, having no direct interaction with the ion-core, contain information about the long-range electrostatic properties of the ion-core (e.g. multipole moments) as well as dynamic properties of Rydberg electron $\longleftrightarrow$ ion-core energy and angular momentum exchange processes [20].

The effective potential of the hydrogen atom also allows insight into the unique properties of core-penetrating Rydberg states. For interactions inside the core, we can consider what happens to the n*-levels in the $1/r$ part of the hydrogen atom potential. It can be shown that the amplitude of the innermost lobe of the wavefunction scales as (n*$^{-3/2}$) as n* increases (see Fig. 1-3) [7]. This phenomenon, which is a by-product of the normalization procedure for the electronic wavefunction, corresponds to having the nodes for the first lobe of all n* occurring at nearly the same value of r [3]. This amplitude scaling property is important because it allows quantities involving matrix elements to be predicted throughout the entire range of n* for a given n,l series. This scaling property is exploited throughout this work; for example, it explains the evolution of the spin-orbit constant, A, in $^2\Pi$ Rydberg states (see Section
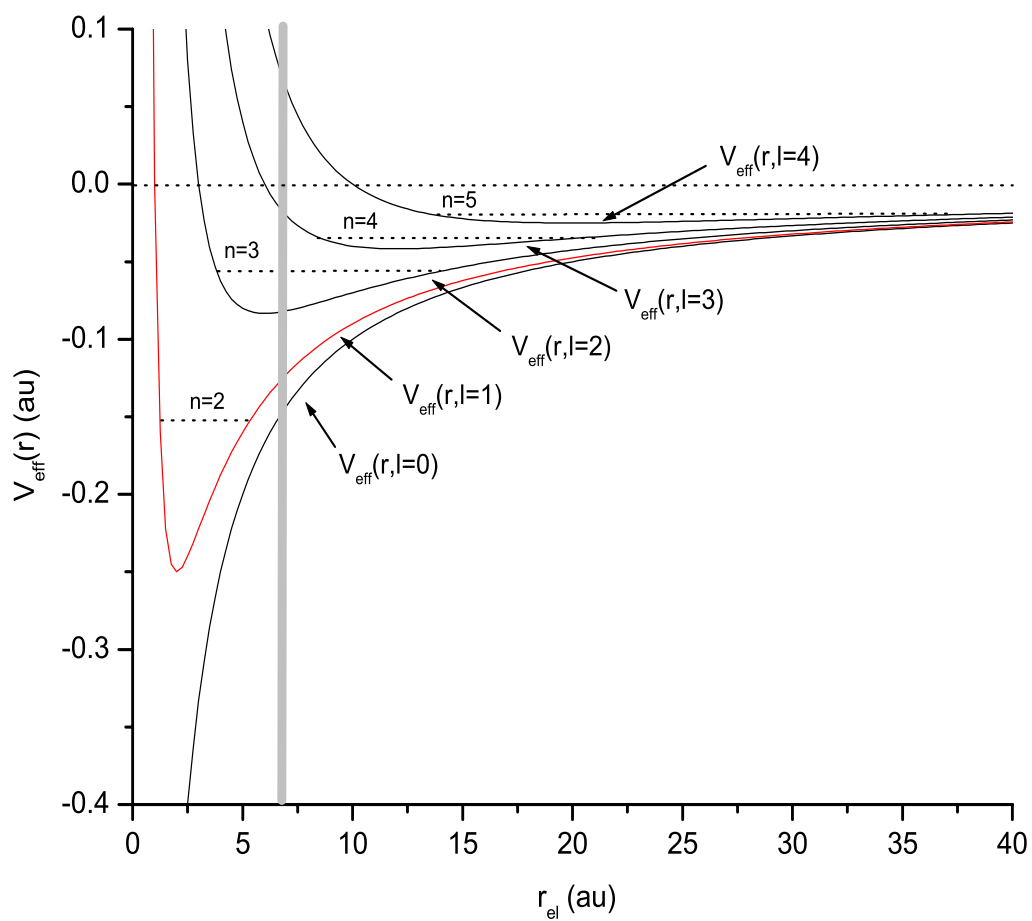
Figure 1-2: Effective potential of the hydrogen electron. Superimposed on this is the vertical gray line indicating the spatial extent of the CaCl$^+$ ion-core. High-l states become centrifugally excluded from the core, defining a separate class of *core-nonpenetrating* Rydberg states.
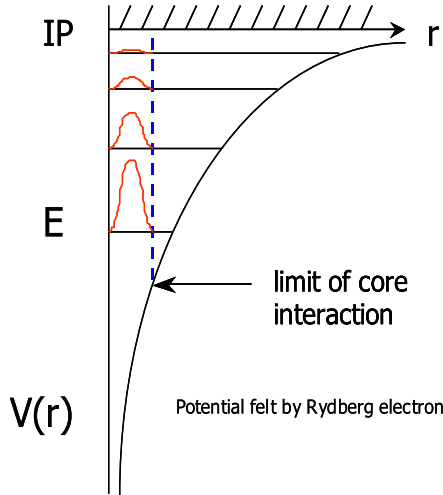
Figure 1-3: Effective potential of the hydrogen atom for l=0. The amplitude of the innermost lobe of the Rydberg wavefunction scales as $\text{n*}^{-3/2}$ for all n*. This convenient and unique property of Rydberg states allows global prediction of quantities governed by matrix elements (e.g. spin-orbit splittings, absorption coefficients, predissociation rates, etc.) from only a handful of measurements.

3.3.2) as well as the magnitude of the matrix element describing the predissociation of $^2\Sigma^+ \sim ^2\Sigma^+$ states (see Section 5.3).

This thesis focuses specifically on one member of the alkaline earth monohalide family, CaCl. Whereas CaF and BaF have been extensively studied by this group [9–11,13–16,20], considerably less is known about the Rydberg states of CaCl. Earlier studies of CaCl by our group through both ionization (REMPI) and fluorescence-based methods indicated that the low-n* (n* $\approx$ 3-7) Rydberg states are predissociated [16, 22]. Indeed, the main differences in the Rydberg spectra of CaF and CaCl arise from the fact that the dissociation limit of CaCl lies much farther below its first ionization limit than that of CaF: [IP$_1$ - D$_o$ = 2800 cm^{-1} (n* $\approx$ 6.26) for CaF, 15 300 cm^{-1} (n* $\approx$ 2.68 for CaCl). Thus we would expect the low-n* Rydberg states of CaCl to be extensively predissociated by the two repulsive or weakly bound $^2\Sigma^+$ and $^2\Pi$ states which dissociate to the $M(^1S)+X(^2P)$ neutral atoms (see Fig. 3-1).

Nevertheless, several experiments described in this thesis, when combined with the

pioneering theoretical and experimental work on CaF and BaF conducted by former members of this group and our colleagues in France, have allowed considerable insight into the spectra and dynamics of CaCl. This thesis will describe the results for the following experiments:

- Chapter 3 - Survey spectra from X $^2\Sigma^+$ ground state revealed a number of $^2\Sigma^+$ and $^2\Pi$ low-n* Rydberg series members previously undetected by fluorescence [16]. The observed energy positions allowed a qualitative determination of the $^2\Pi$ repulsive state position as well as determination of the quantum defect derivatives.

- Chapter 4 - OODR (Optical-Optical Double Resonance) spectra of low-n* Rydberg states allowed a window into CaCl dynamics with higher resolution, although only a few states could be directly observed by this method.

- Chapter 5 - The predissociation mechanism for CaCl $^2\Sigma^+$ states was determined from a linewidth analysis of ion-dip spectra previously recorded [22]. The position of the $^2\Sigma^+$ repulsive state curve reponsible for the predissociation was determined.

- Chapter 6 - OODR spectra of the autoionization region above the $v^+ = 0$ ionization potential recorded via the D $^2\Sigma^+$ state revealed a large number of $^2\Sigma^+$ states. These data were fitted via MQDT (Multichannel Quantum Defect Theory) techniques to determine quantum defects for $s \sim p \sim d$ mixed $^2\Sigma^+$ Rydberg states.

These experiments were preceded by the design and construction of a 3rd generation molecular beam apparatus by Dr. Sergey Panov and myself. The construction project lasted for the better part of two years, and is extensively described in Chapter 2. It is hoped that this machine, as well as the experiments described herein on CaCl, prove useful to future workers in our group.
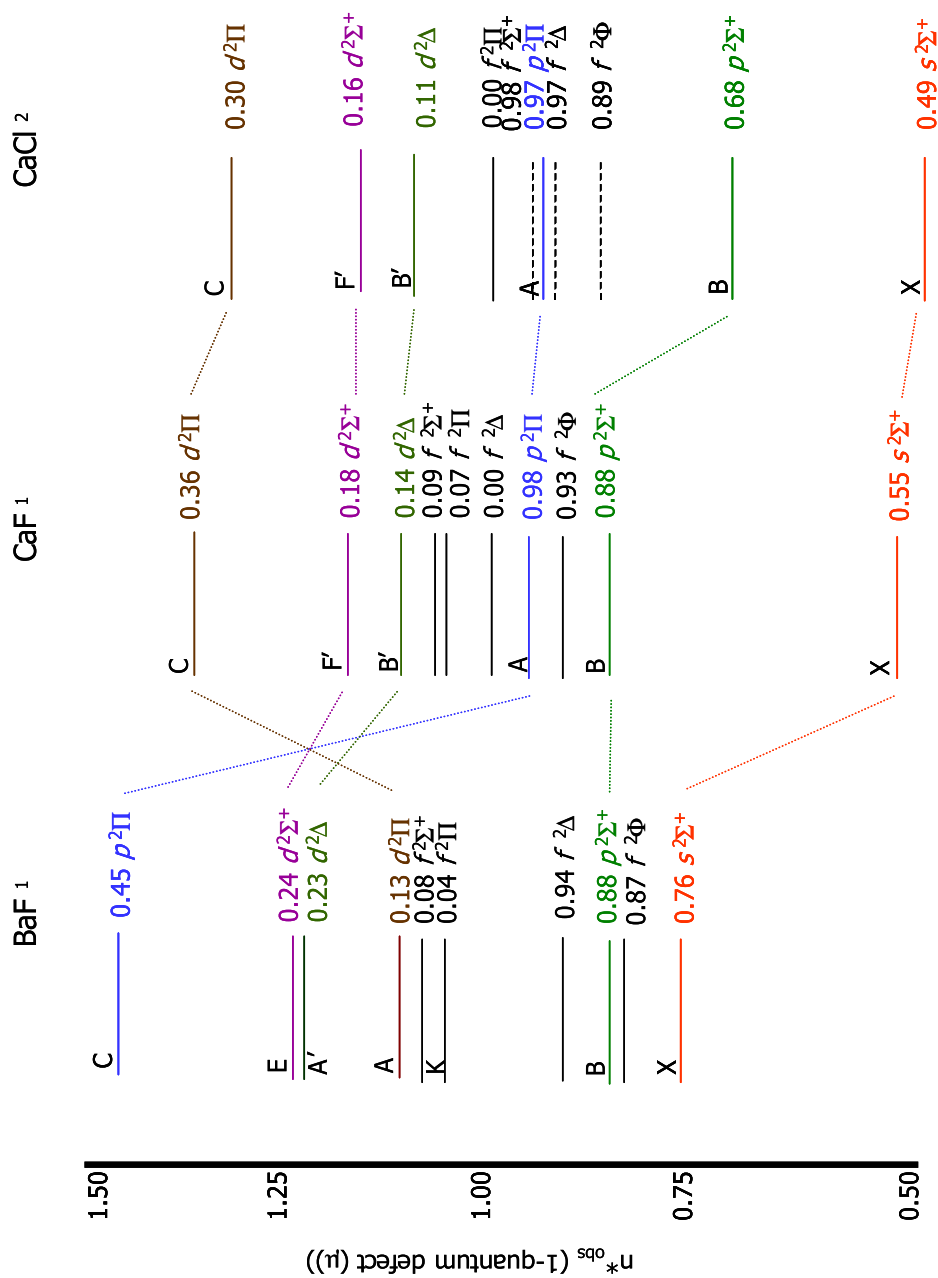
Figure 1-4: Experimental and theoretical values of quantum defects for Rydberg series of MX molecules. Dashed horizontal lines represent as yet undetected states (mostly core-nonpenetrating). Roman letters indicate the low-n* terminus of the specified series - e.g. the $s\ ^2\Sigma^+$ series has a quantum defect of (1-n*_{obs}) and terminates on the X state.

Chapter 2

Experimental Apparatus and Methods

Most of the experiments described in this thesis were conducted in a molecular beam chamber designed to be flexible and adaptable to a variety of configurations. In this section I outline the design principles and operating characteristics necessary for successful signal acquisition, and is intended as a reference source for future users. Results of molecular beam experiments performed on CaCl are discussed in subsequent chapters.

2.1 General Physical Description

The molecular beam apparatus in its present configuration consists of three stainless steel six-way crosses connected via gate valves to two diffusion pumps, which are in turn connected to mechanical roughing pumps. The six-way crosses are subdivided into "source" and "detection" chambers, as indicated in Fig. 2-11. The source chamber is the largest of the three crosses, with a nominal flange diameter of 14" (ISO 150, MDC part L1200-6), and is separated by a 10" ASA flanged electro-pneumatic gate valve (VRC LP series 94578-101) from a 4400W 10" diffusion pump (Varian VHS-10, 6600 l/s He pumping speed) charged with 1L of Varian Neovac SY oil. The VHS-10 pump is connected via QF40 2" ID diameter hose to an Alcatel 2100 rotary vane

mechanical pump (90 CFM air). The source chamber contains a homemade photoablation source connected to a General Valve Series 9 solenoid valve mounted on an x-y translatable stage approx. 4 cm from a conical solid nickel skimmer (0.5mm orifice diameter, Precision Instrument Services). The skimmer in turn is mounted on the gate valve which forms the boundary between the source and detector chambers. The detection chamber consists of two connected six-way crosses (MDC L0800-6) with 8" CF flange ports, and is pumped via a 1450W 5.25" diffusion pump (NRC Model unknown) through a liquid nitrogen trap (Cook Vacuum Products part LNT-4201LL). The detection-side diffusion pump uses 500 mL charges of Santovac 5 oil, which is well-known for its temperature stability, extremely low vapor pressure, and very high cost. The detection chamber is rough-pumped by an Alcatel 2063 rotary vane pump with a specified displacement of 53 CFM from 1-1000 Torr. Other active elements in the detection chamber include a Time-of-Flight/Mass Spectrometer, which will be described below, as well as a microchannel plate (MCP) ion detector. Vacuum pressure is monitored in both source and detection chambers by a series of thermocouple (Varian type 801, active range 1-1000 mTorr) and Bayard-Alpert ionization gauges (Duniway Stockroom I-075-P) connected to a suitable controller (Granville-Phillips 372-004, active range 10^{-3} Torr - 10^{-10} Torr). The base pressure with no gas load was typically $O(10^{-7})$ and $O(10^{-8})$ Torr for the source and detection chambers, respectively. Operating pressures with a typical gas load of 25 PSI introduced from the pulsed nozzle at 20 Hz were $O(10^{-4})$ Torr in the source side and $O(10^{-6})$ Torr for the detection side.

2.2 Vacuum and Molecule Production and Detection

2.2.1 Molecular Beams

Atomic and molecular beams have been used since the 1920s [23]. These beams were called "effusive" beams, because the gas behaves as a collection of individual particles,

with the number of collisions being reduced to near zero. This arises from using an orifice size small enough that $D \ll \lambda_o$, where D is the diameter of a circular orifice and λ_o is the mean free path of the gas at pressure P_b, which is the backing pressure of the gas reservoir [24]. A typical effusive molecular beam experiment consists of a multiple-chamber apparatus in which one side contains a sample that is heated to raise its vapor pressure. A small hole in the wall of the oven chamber allows some of the sample to enter the second chamber, which is at a higher vacuum. The sample molecules that enter the high-vacuum chamber have a velocity distribution determined by the Maxwell-Boltzmann distibution in the oven. Specifiable regions of this velocity distribution can be selected downstream in the detection chamber, with the disadvantage of losing a large fraction of the beam intensity with each selection element. Molecules in this type of beam also have the vibrational and rotational state distribution that correspond to the temperature of the oven, which can be several hundred Kelvins. An effusive molecular beam source is thus a valuable tool for studying highly excited rotational or vibrational states (hot bands) of molecules.

In 1951 Kantrowitz and Grey published a theoretical description of a proposed "supersonic jet" as a molecular beam source [25]. While their original goal was to increase the beam intensity, they noted that their source would produce a cooling of the translational and internal degrees of freedom of the molecules in the beam. The main feature of Kantrowitz's and Grey's proposal was the reversal of the inequality noted above with respect to the nozzle diameter and the mean free path. If $D \gg \lambda_o$, there will be many collisions as the gas flows through the orifice and through the expansion region downstream from the orifice. This hydrodynamic flow condition converts the enthalpy associated with random atomic motions into directed mass flow, causing the mass flow velocity u to increase [24]. It is this conversion of random motion to directed mass flow which causes the temperature to decrease. Other thermodynamic quantities are affected by this process; for example, the classical speed of sound, a, is defined as

$$(\frac{\gamma k T}{m})^{1/2}, \tag{2.1}$$

where γ is the heat capacity ratio C_p/C_v, k is the Boltzmann constant, T is temperature, and m is the mass. Since a is directly proportional to T, the local speed of sound decreases during the expansion process, and the Mach number ($M \equiv (u/a)$) increases. In an ideal expansion $M = 1$ for the most constricted point in the nozzle, but with additional expansion $M \gg 1$ [24]. This is the supersonic flow regime, and is the regime in which our present apparatus functions. The core of the expansion (the so-called "zone of silence") is the active region for downstream experiments. Skimmers are frequently employed to separate the cold core of the beam from the hot shock wave which defines the outer envelope of the expansion. In our case a conical skimmer with a 0.5 mm diameter orifice separates the source and detection chambers, where the detection chamber remains at 100 times lower pressure under load than the source chamber. In a conically skimmed beam, internal relaxation freezes and the molecular flow regime dominates, thereby minimizing multi-body collisions that would lead to molecular cluster formation [26]. Since the expansion process is dependent on the properties of the gas involved, heavier gases are more likely to form clusters. Early experiments carried out in our machine suggest that using Ar as a carrier gas is much more likely to promote cluster formation than He.

The development of the supersonic molecular beam was a boon to spectroscopists, who had previously been limited to studying molecules under "hot" (e.g. 300K) conditions of a room temperature or oven source. The opportunity to produce molecules with very low rotational temperatures O(15 K) allowed the recording of much simpler spectra than could be obtained by conventional techniques. These simpler spectra made spectral analysis of complicated molecules much more tractable. It should be noted that the translational and rotational cooling occur on a much faster timescale than vibrational cooling in a typical molecular beam. While it is true that the majority of the population will be in the ground vibrational state, there is often significant population in higher vibrational states. In CaCl, for example, we have observed transitions involving up to $v = 3$ in the $^2\Sigma^+$ ground state (further details in Chapter 3).

Another design consideration for construction of a supersonic molecular beam

is whether to use a continuous or pulsed source. Pulsed sources have a number of advantages over continuous ones in most applications. The primary attraction of a pulsed beam is especially obvious for experiments with pulsed lasers which have repetition rates $\leq$ 100 Hz. Since the gas flow need only be on when the laser light is present, pulsed sources demand less in the way of vacuum pump throughput to achieve the same amount of cooling. An additional advantage is that the transition point between continuous and molecular flow (which culminates in a disruptive shock wave called the Mach disk) is moved downstream from the gas nozzle by a factor O(100), greatly facilitating crossed-beam experiments [23, 26].

2.2.2 Pulsed Valve

The Series 9 Pulsed Valve (General Valve, Inc.) provides a versatile way of introducing high ($<$ 100 PSI) backing pressures of gas into a vacuum, but its design is not without disadvantages. The valve consists of a magnetically actuated poppet-and-spring mechanism which requires (1) sufficient rise-time for opening and closing (250 μs. each half-cycle, which effectively limits its maximum repetition rate to 35 Hz, and (2) suitable materials for poppets. To reap the benefits of using a pulsed molecular beam (i.e. lower background pressure and more effective molecular cooling), it is absolutely essential to have a leak-tight pulsed valve. We have tested a number of poppet materials, from Teflon to more exotic and considerably more expensive materials suited for high-temperature or corrosive environments such as PEEK (polyetheretherketone resin) and Vespel (polyimide). In general, the softer the poppet material, the more likely it is to deform over time, yet in the beginning of its life cycle it is more likely to form a better seal. The harder poppets are less likely to deform, but they also do a poorer job of sealing with high backing pressures ($>$30 PSI). The material we have found to have the most favorable combination of durability and sealing ability is Kel-F (chlorotrifluoroethylene), although even a Kel-F poppet must be replaced after every eight-ten hours of use. A leaking poppet will manifest itself with a greatly increased foreline pressure on the roughing pump thermocouple gauge (from $\approx$ 150 mTorr to $>$1000 mTorr), a strong degradation of any type of collected ion signal

(i.e. asymmetric or weak peaks with 10-25% of normal intensity), and often large oscillations in the ion gauge readings of source chamber pressure. Calcium fluoride production in particular is problematic due to buildup of a black powder (assumed to be a byproduct of the fluoroform Ca plasma interaction described below) inside the solenoid body that holds the poppet in place. If too much powder accumulates between the poppet and the solenoid body, the seal is compromised and the poppet must immediately be replaced.

2.2.3 Vacuum Considerations

A question that often arises in using a pulsed valve molecular beam source concerns the optimum backing pressure of gas to be used in a particular experiment. While that pressure will of course vary depending on the circumstances involved, there are limitations on the range of P_b imposed on the user by the mechanical and diffusion pumps. From the diffusion pump perspective, we can calculate the maximum permissible backing pressure by using the diffusion pump throughput and the velocity of He carrier gas (for a monatomic gas, $\sqrt{\frac{5RT}{3M}}$) [15]. The total gas flux is the product of the orifice backing pressure P_b, the gas velocity at the orifice, the orifice area, the pulse duration, and pulse repetition rate [15]:

$$Q_{noz} = P_b v A \tau r. \tag{2.2}$$

Since the flux into the source chamber cannot exceed the maximum throughput of the diffusion pump, we can easily calculate the maximum nozzle pressure:

$$P_b^{max} = \frac{Q_{noz}}{vA\tau r} = \frac{7.7 \,\mathrm{Torr}\,\mathrm{l}\,\mathrm{s}^{-1}}{(1.0 \times 10^5 \,\mathrm{cm\,s^{-1}})(2.0 \times 10^{-3} \,\mathrm{cm^2})(3.5 \times 10^{-4} \,\mathrm{s})(20 \,\mathrm{Hz})}. \tag{2.3}$$

$P_b^{max} = 7.2 \,\mathrm{atm} \approx 106 \,\mathrm{PSI}.$

More stringent limitations apply if if the use of a water baffle or a nitrogen trap is used, as either of these devices can effectively reduce the pumping speed by 50% [1].
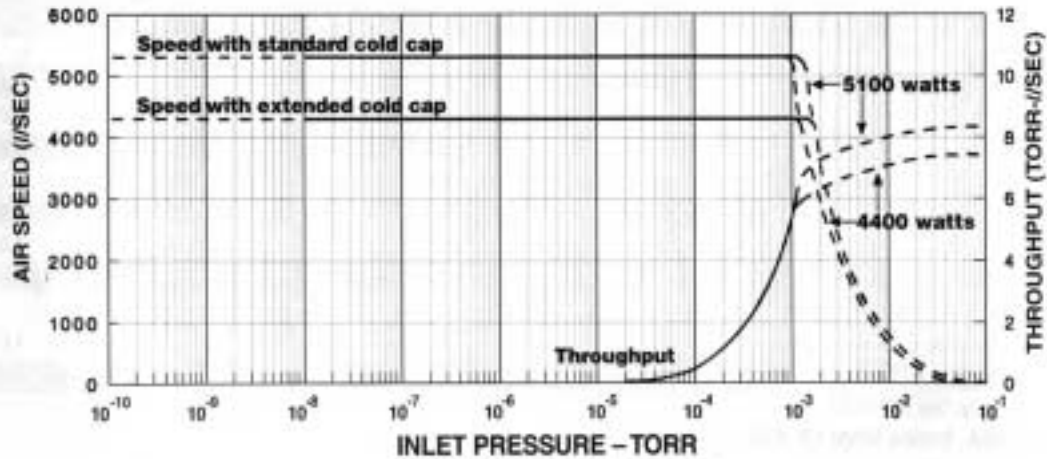
Figure 2-1: Pumping speed for Varian VHS-10 diffusion pump as a function of inlet pressure [1]. Our VHS-10 is presently fitted with 4400 W burners and standard cold cap. Mechanical roughing pumps and manifold layout must be carefully chosen to allow maximum gas throughput for both pumping stages.

Both of these devices greatly reduce the undesirable natural tendency of diffusion pumps to backstream oil into the chamber, but they do limit P_b.

The maximum diffusion pump throughput is also affected by the pumping speed of the mechanical roughing pump to which it is connected. From Fig. 2-1, we can see there is a crossover point between the effective pumping speed of the diffusion pump and that of the mechanical pump. If the gas load is sufficiently high, both pumps operate sub-optimally and total throughput is decreased.

An important aspect of diffusion/mechanical pump operation is the manner in which the diffusion pump is connected to the mechanical pump. In the viscous flow regime (i.e. mean free path $\ll$ than the dimensions of the pipe), the maximum conductance in a tube of circular cross section is given by [27]

$$C = 180 \frac{D^4}{L} P_{av} \, l \, s^{-1}, \tag{2.4}$$

where the diameter and length are in cm, and the average pressure P_{av} is in Torr. Since the conductance goes as the fourth power of the diameter of the connecting hose and the first power in the length, it would be advantageous to maximize the

diameter while minimizing the length of the connection. This fact was unappreciated in the first several months of beam machine operation, as the source chamber foreline pressure was typically 500 mTorr. This produced unacceptable diffusion pump oil backstreaming, coating surfaces inside the source chamber (including the optical windows) with a light layer of oil. The pump was moved from its original distance of 6 m to 1 m from the apparatus and the diameter of the PVC cord-reinforced connecting hose (Varian #HFP200) was enlarged from QF30 (1.5 in. ID) to QF40 (2.0 in. ID). This resulted in the reduction of the foreline pressure to a more acceptable 150 mTorr. The addition of a high-throughput roughing device such as a Roots blower would decrease the foreline pressure even further, provided it was installed close to the chamber. A better pump would have the additional effect of enhancing rotational cooling in the molecular beam.

Since the source chamber and detection chamber are connected through a very small orifice (.5 mm dia. conical skimmer) it is possible to maintain a higher vacuum in the detection side. This doubly-differentially-pumped scheme allows the skimmed beam to undergo a minimum of collisions with background gases in the detection chamber. The conical skimmer simply selects the gas molecules with momentum components along a chosen axis (in our case the horizontal axis of the laboratory). This beam axis can be interrogated in the detection side by a combination of laser and microwave radiation as will be discussed in subsequent chapters. Since the active detection elements in our apparatus use microchannel plates (MCP), the pressure must be low enough in the detection chamber ($< 10^{-5}$ Torr) to prevent these high-voltage biased devices from arcing. Great care must be taken, as even momentary exposure to high pressure ($\geq 10^{-4}$ Torr) can destroy an MCP stack. Since typical operating pressure in the detection chamber is 10^{-6} Torr, this is well within the MCP operationing range.

Since an MCP detector is an extremely efficient charged particle detector (it can be biased in such a way as to detect cations or anions), it is important to minimize the amount of contamination from additional molecular species in the chamber. One primary source of contamination is from diffusion pump oil, and even small amounts

of backstreaming can produce peaks in the mass spectrum that belong to any number of hydrocarbon by-products, especially if UV lasers are being used. The use of a liquid nitrogen trap and the best possible diffusion pump fluid is thus absolutely essential to minimize contamination and system pressure. Santovac 5 fluid, despite its cost (\$625/liter), allows consistent operation in the $10^{-6} - 10^{-8}$ Torr range. Future configurations of the apparatus could include a transition away from the venerable diffusion pump towards the much cleaner and lower-maintenance turbomolecular pump. This upgrade would only be practical on the detection side, where the pumping rates (<1200 l/s) are comfortably within the boundaries of current turbo pump technology.

2.2.4 Interlocks

An electronic interlock system utilizing voltage relays was designed to prevent or at least minimize danger to the apparatus and its auxiliary equipment in the case of a catastrophic failure. There are several modes of failure, and a few of them are outlined in Table 2.1 along with the interlock system response.

An interlock system cannot possibly provide complete protection, but the present one provides a reasonable level of security for the most common failure modes. One necessary enhancement to the interlock system involves protection in case of failure of the roughing pumps. This recently occurred (September 2001) with the detection chamber rough pump, causing massive contamination of the detection chamber by by-products of Santovac 5 combustion. Several days were expended to disassemble and thoroughly clean each component in the chamber, and the MCP stack in the TOF/MS detector was completely coated with oil and had to be replaced.

As with any high vacuum system, the inappropriate actuation of a valve can have disastrous consequences for the system, either by oil contamination or sudden destruction of sensitive detectors. Personnel must take extreme caution at all times to avoid mishaps.

Failure	Possible Outcome	Interlock Response
Cooling water for diffusion pump stops	Diffusion pump oil burns	Water flow interlock trips relay and pumps shut off
MCPs activated with pressure $> 10^{-4}$ mTorr	Immediate MCP destruction (arcing)	MCP power supply cannot be activated if $P > 10^{-4}$ or if diff. pump is not on
LN$_2$ supply exhausted	High backstreaming rate contaminates chamber, MCP lifetime reduced	LN$_2$ level sensor trips relay diff. pump & MCPs turned off
Source chamber gate valve opened with chamber at atmosphere	Massive chamber contamination with DP oil	Gate valve will not open if source chamber at atmosphere
Hard drive failure on data acquisition computer	Data lost	Data immediately sent to file server for backup
Campus TCP/IP network failure	Data for scan lost	Internal network switch provides network security and redundancy

Table 2.1: Catastrophic Failure Mode and Interlock Response

2.2.5   Photoablation

In many cases the target molecule of a spectroscopic investigation is neither a permanent gas nor sufficiently stable to allow storage in a gas mixture. This is particularly true of radical species such as the alkaline earth monohalides (MX), and any experimental work on this class of molecules necessitates *in situ* production.

In our apparatus, *in situ* molecule production is possible by direct reaction of Calcium plasma with a halogen carrier such as fluoroform (CHF_3) in the case of CaF or chloroform ($CHCl_3$) in the case of CaCl:

$$Ca^+ + CHX_3 \longrightarrow CaX + CHX_2^+. \tag{2.5}$$

The calcium plasma is produced by focusing approximately 5 mJ of 355 nm laser light via a 0.5 m focal length lens onto a 0.5 mm^2 spot on a rotating Ca rod in a method developed by Smalley [28]. The rod (0.125" in diameter and typically 2 in. long) is rotated inside the source chamber by a precision DC motor Pittman #8712-41) which completes approximately 2 revolutions per minute. The motor, rated at a max. continuous torque of 100 N·m at 41 RPM, is under full load with 19.1V. It is usually operated at half of this voltage to prolong its operating lifetime inside the vacuum chamber. The Mean Time Between Failures (MTBF) for a DC motor in our experience is 1.5 years, and the main failure mode, as one might expect, is overheating by ineffective heat dissipation. Calcium plasma production is synchronized to the opening of the pulsed valve, so that rapid thermal cooling of the hot metal atoms and reaction with the oxidant (if present) can occur in the small reaction channel (1 mm^2 diam. × 5 mm long) before expanding into the vacuum.

The precise amount of both reactants needs to be carefully controlled for optimum signal production. Adjustment of Ca plasma flux is easy to achieve by reducing the power of the Nd:YAG laser beam, either by introducing a mesh screen or defocusing the alignment lens mounted on an x-y translation stage. Too much Nd:YAG power can adversely affect CaX production by production of $(CaX)_x$ and $(Ca)_x$ clusters [15,28]. Misalignment of the tightly focused beam can also ablate aluminum from the

target rod housing assembly, although this can be minimized by an alignment check performed during routine adjustment of the rod position. Since the rod assembly, as presently constructed, does not have a translation feature, the Ca is ablated from the rod in a simple ring pattern. Ablation at the same rod location causes the furrow in the rod to grow deeper, eventually moving out of the focus spot of the laser. At this point Ca production becomes unstable and CaX production decreases. This instability can also be caused by defects or voids in the bulk Ca, which are by-products of the casting process used by the manufacturer (Alfa Aesar, 99.9% pure Ca ingot). A single target rod vertical position typically provides stable Ca production for 8-10 hours. Although a change in position necessitates breaking the vacuum in the source chamber, an experienced operator can change the rod position and have the system back under vacuum in less than ten minutes.

A more periodic signal fluctuation is caused by asymmetric placement of the machined target rod inside its holder. This manifests itself as an increase in signal during the half-cycle that the rod is slightly (≈ 0.001 in) closer to the laser focus spot and a decrease in signal when it is further away. This slow periodicity often manifests itself in the baseline of the resulting spectrum, obscuring weak features. Fortunately, the periodicity can be almost entirely eliminated by wrapping sufficient teflon tape around the target rod to ensure a snug fit in the rod holder. This technique compensates for the varying diameter of lathe-machined rods and renders use of a set screw unnecessary.

Regulation of halogen-containing species is also critical to CaX signal production. This condition is considerably easier to achieve in the case of CaF, where the halogen carrier of choice, fluoroform (Halocarbon 23), is a permanent gas at STP. After numerous trial and error attempts using mixtures of helium and varying amounts of fluoroform, an optimum concentration of 2% fluoroform (by volume) in He was discovered. Higher concentrations produced unacceptable $(CaF)_x$ clustering, and lower concentrations produced large amounts of excess Ca, as observed by the Time of Flight-Mass Spectrometer (TOF-MS) described in the next section.

Once this optimum concentration of fluoroform was discovered, it became desir-

44

able to produce the mixture in the largest feasible quantity. A special gas handling procedure was then developed to facilitate high pressure mixing. A tank of pure fluoroform (BOC VLSI grade 99.8% purity) was connected to a large (BOC 200 size) empty He cylinder under rough vacuum (≈ 1 mTorr). The regulator of the fluoroform cylinder was adjusted to provide 20 PSI and the valves for both the empty He cylinder and fluoroform were opened. After approximately one minute, the pressures had equilibrated in both tanks. The fluoroform valve was turned off, and a high-pressure (2500 PSI) high-purity He (BOC Grade 5) cylinder was connected to the manifold. By careful introduction of the high-pressure He, the mixture tank could be filled to a total pressure of 1000 PSI, giving a P_{CHCl_3} of 2%. One of these prepared mixtures typically lasts for several weeks of continuous operation.

Since chloroform is not a permanent gas at STP, additional techniques had to be developed to ensure a constant supply of reactant. At room temperature, chloroform has a substantial vapor pressure of 3 PSI [2]. Our first approach was to construct a gas manifold with a stainless steel bulb containing 50-100 mL of $CHCl_3$ inline (see Fig. 2-2). High pressure helium regulated at R1 would bubble through the chloroform, creating a mixture that was reduced in pressure by another regulator R2 before reaching the pulsed valve. R1 could in theory be adjusted through its working range to give a variable amount of chloroform. In our present setup R1's working range of 20-150 PSI would deliver chloroform concentrations of 2-13%. Early experiments indicated that even the lowest available concentration (2%) was causing quenching of the CaCl production channel after a period of approximately a half hour. This observation was interpreted as being analogous to conditions in a Broida-type oven, where the use of needle valves easily permits "overshooting" of the optimum oxidant concentration. A simple solution to the chloroform concentration problem presented itself upon examination of the chloroform vapor pressure dependence on temperature (see Fig. 2-3), where we can see that if the chloroform were cooled from room temperature to -10° C, the vapor pressure would decrease by a factor of 5 [2]. A water/methanol ice slurry cooled by liquid nitrogen would therefore allow a much greater controllable dynamic range of chloroform concentration than just using gas

regulators. After much trial and error, parameters for optimum CaCl production were determined: a regulator R1 pressure of 100 PSI and a water/methanol ice bath temperature of -5 to -10° C. This corresponds to a total chloroform concentration of 0.60-0.80%. The temperature of the bath in a 660 mL vacuum flask is relatively constant but must be recharged every two hours or so with a charge of LN_2 , while a chloroform charge of 75 mL lasts for three months of continuous use.

2.2.6 Time-of-Flight Mass Spectrometer

The Time-of-Flight Mass Spectrometer components were manufactured by R.M. Jordan Co. (model C-677 lens stack assembly) and modified from their original design to permit the use of pulsed-field ionization (see Figs. 2-5). During normal operation, ions formed by laser excitation of the molecular beam in the region between plate A1 and M (both held at a constant 1500 V) are repelled by a differential extraction pulse (+200V) applied to plate A1 $\approx$100 ns after the laser excitation pulse terminates. The ions are further accelerated by field plates M (1500 V) and A2 (1480 V) toward the MCP plate assembly 75 cm away, and are space-focused by Einsel lenses en route to direct maximum ion flux to the 5.0 cm^2 active area of the MCP plate assembly.

The MCP plates themselves (Burle Electro-optics #1396-1812) are discs of lead glass $\approx$0.75 mm thick and 5.2 cm^2 in diameter. They consist of $O(10^6)$ cylindrical channels with a diameter of 10 μm and an interchannel separation of 12 μm. Electrons emitted from the channel walls by ion impact are accelerated toward the other side of the plate by a differential electric field [29]. Secondary electron emission from the channel walls initiates an electron avalanche which is collected by an anode and then output through a 50Ω termination circuit to an oscilloscope for observation. To increase MCP gain, additional MCPs can be placed in series. To suppress ion feedback effects, MCP channels are biased at an angle of $\approx$ 5° to the surface normal [29]. When using multiple MCPs in series, these offset angles must be aligned in a "V" or "chevron" assembly to provide optimal ion feedback suppression for the entire stack (see Fig. 2-4). Our apparatus uses a 2-plate stack with a total gain $O(10^6)$ and subnanosecond rise time [30]. An grid 1 cm in front of the MCP stack is held
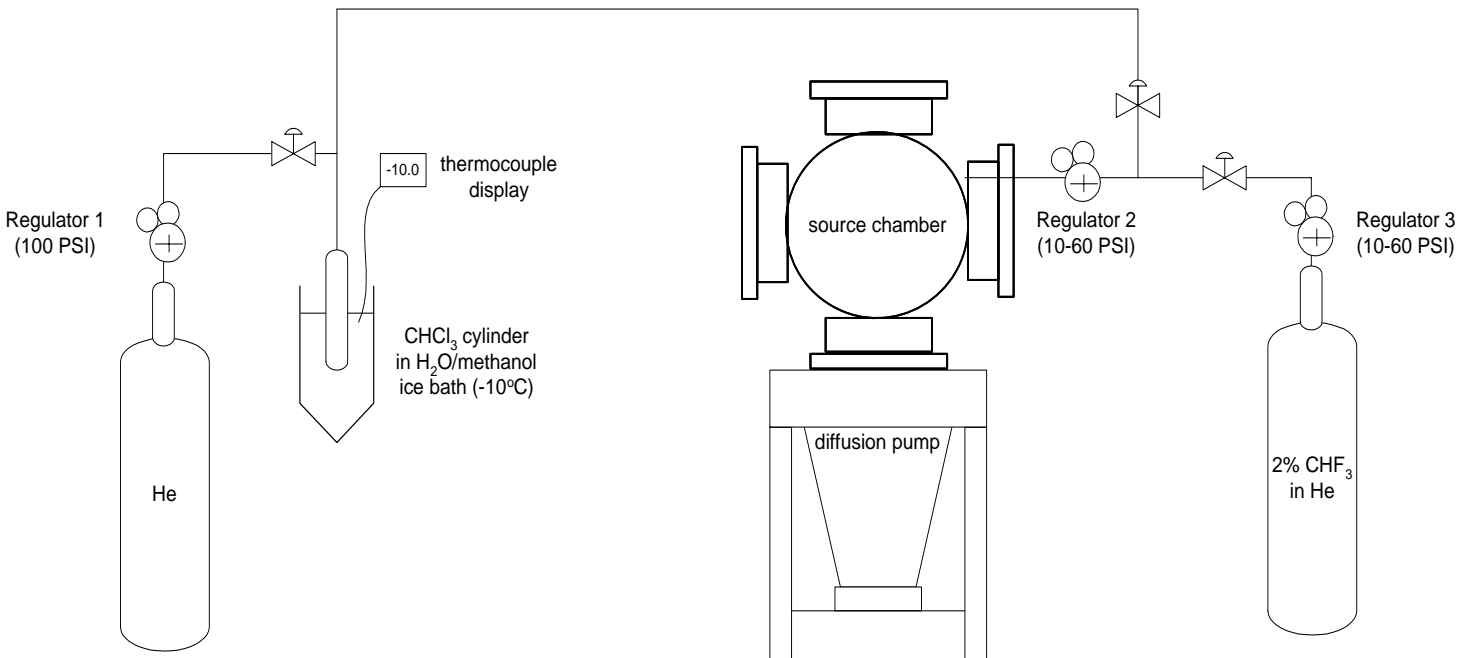
Figure 2-2: Gas layout for *in situ* production of CaCl and CaF.

Regulator 1
(100 PSI)

He

-10.0 thermocouple
       display

CHCl$_3$ cylinder
in H$_2$O/methanol
ice bath (-10ºC)

source chamber

diffusion pump

Regulator 2
(10-60 PSI)

Regulator 3
(10-60 PSI)

2% CHF$_3$
in He
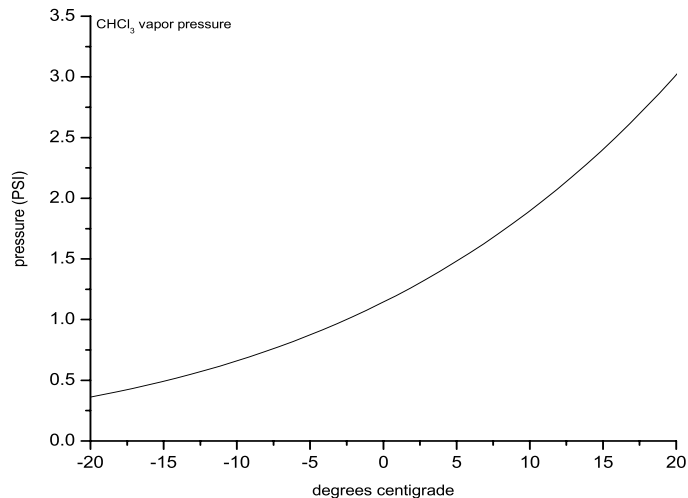
Figure 2-3: Chloroform vapor pressure vs. temperature from NIST Webbook data [2].

at ground potential to allow a field-free drift region for ions in the flight tube. The cylindrically symmetric flight tube can be biased to a few hundred volts, but is usually held at ground.

The ion extraction assembly, with its extraction (A1) and acceleration (M and A2) plates, is contained within a Ni-plated shroud, and the shroud together with the attached liner assembly define an axis normal to that of the molecular beam. The beam arrives in the extraction region (between plates A1 and M) through a conical skimmer attached to the shroud with an orifice of 3 mm diameter. The shroud allows additional protection against contamination from by-products of the ablation process and backstreaming diffusion pump oil, but the shroud/skimmer must be carefully aligned to intercept the molecular beam axis already defined by the 0.5 mm skimmer in the source chamber. Alignment is most easily established using a specially made plexiglas alignment flange, which fits on the end-on flange port normal to the beam. The alignment flange contains a small laser pointer (2 in length, <5 mW power at 610 nm, 3 x LR44 1.5 V power cells) embedded on a modified mirror mount (Newport #MM-2A) in its center. Complete system alignment is achieved by maximizing the laser brightness through the apertures defined by both skimmer nozzles with the

single MCP assembly (gain: 10^3)

+

ion

MCP 1

HV (<1000 V)

Anode Plate

Output Pulse
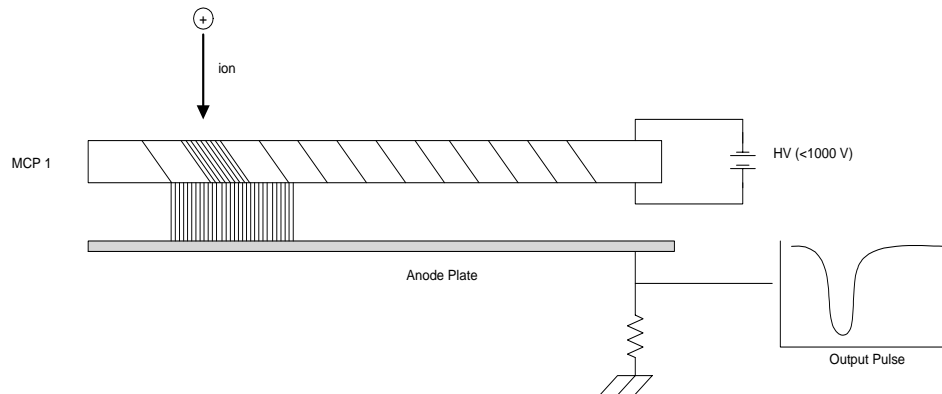
double MCP (chevron) assembly (gain: 10^6)

+

ion

MCP 1

HV (<1000 V)

MCP 2

HV (<1000 V)

Anode Plate

Output Pulse
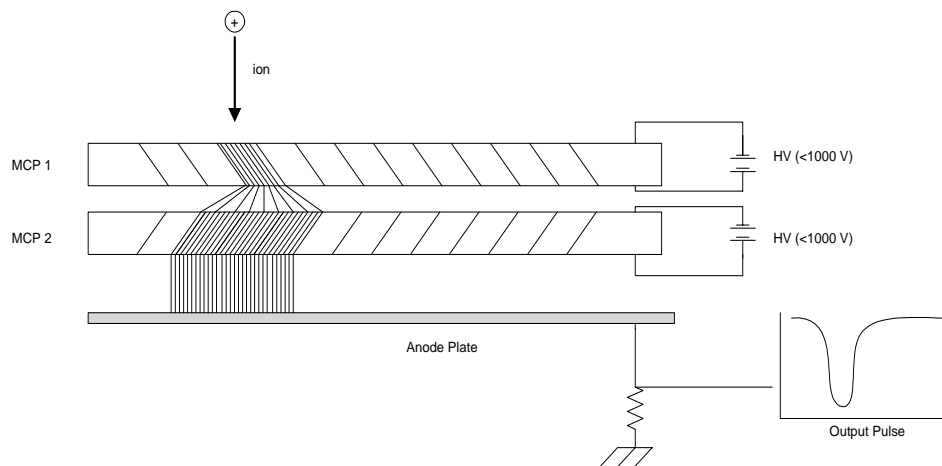
Figure 2-4: Multichannel Plate (MCP) assembly in single and double ("chevron") configuration. The specified gain in a chevron assembly is roughly double that of a single MCP. The chevron orientation of the MCP plate assembly, which is standard in R. M. Jordan TOF/MS detectors, is preferred for its suppression of ion-feedback effects (see text).

mcp stack

detector grid

liner

X-deflector

Einsel tube

focus Einsel tube

acceleration grid Einsel tube

extraction grid (A2)

repeller plate (A1)

skimmer

molecular beam axis

4.4 cm

75 cm

1.27 cm
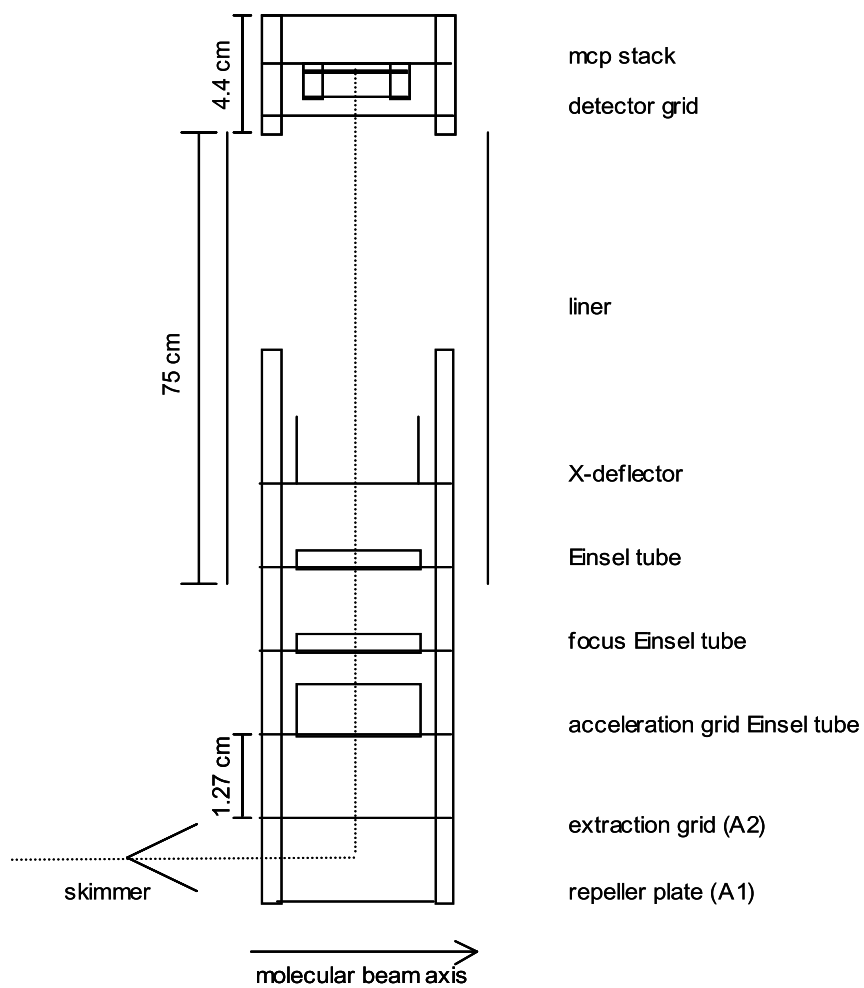
Figure 2-5: Schematic cross-section of R. M. Jordan Time-Of-Flight/Mass Spectrometer assembly as originally installed.

pulse-valve assembly removed (see Fig. 2-6). The x-y position of the pulse-valve mounting assembly is adjusted so that its center falls on the line established by the skimmer apertures.

The ions gain most of their acceleration between the acceleration grids A2 and ground grid G, although they may have some residual transverse velocity, which is compensated by deflection grids placed immediately after the extraction region. In a properly aligned TOF-MS system, only minimal compensation voltages (O <10V) should be necessary. It should be noted that the one of the most critical voltages for optimum signal acquisition is the Focus Einsel Tube (marked "VR1" on power supply, "FOC" on flange assembly). A nominal VR1 voltage of -90 to -100 V is required for optimum ion focusing, and small adjustments (+/- 3 V) must be performed very carefully to avoid loss of signal.

The design employed by R.M. Jordan Co. is based on the original suggestions of Wiley and McLaren [31]. In this design, the ion flight time is relatively insensitive to the exact point of ion formation in the extraction region. This technique, called "space focusing" allows high mass resolution ($\leq$300 m/z) and relative simplicity of construction [15,32]. Readers interested in the mathematics behind the space-focusing criterion are referred to the excellent summary by Gittins and the original paper by Wiley and McLaren [15,31].

To quantify the mass resolution of our constructed device as well as to determine the optimum ratio of extraction plate to acceleration plate voltages, experiments were performed on Xenon. A two-photon transition in a mixture of 3% Xenon in He at 252 nm was saturated with $\approx$2 mJ/pulse from a frequency-doubled Nd:YAG-pumped dye laser (Lambda-Physik Scanmate 2E). The excited Xe was ionized following resonant absorption of a third photon, which brought the total 3-photon energy above the Xe ionization potential of 97 834.4 cm^{-1}. The resulting Xe$^+$ mass spectrum, as captured from an oscilloscope (LeCroy model 9360), is shown in Fig. 2.2.

The seven major Xe isotopes are clearly visible (the ^{128}Xe isotope is a shoulder on the much more abundant ^{129}Xe isotope), and their intensities have representation proportional to their natural abundance (see Table 2.2). These experiments indicate
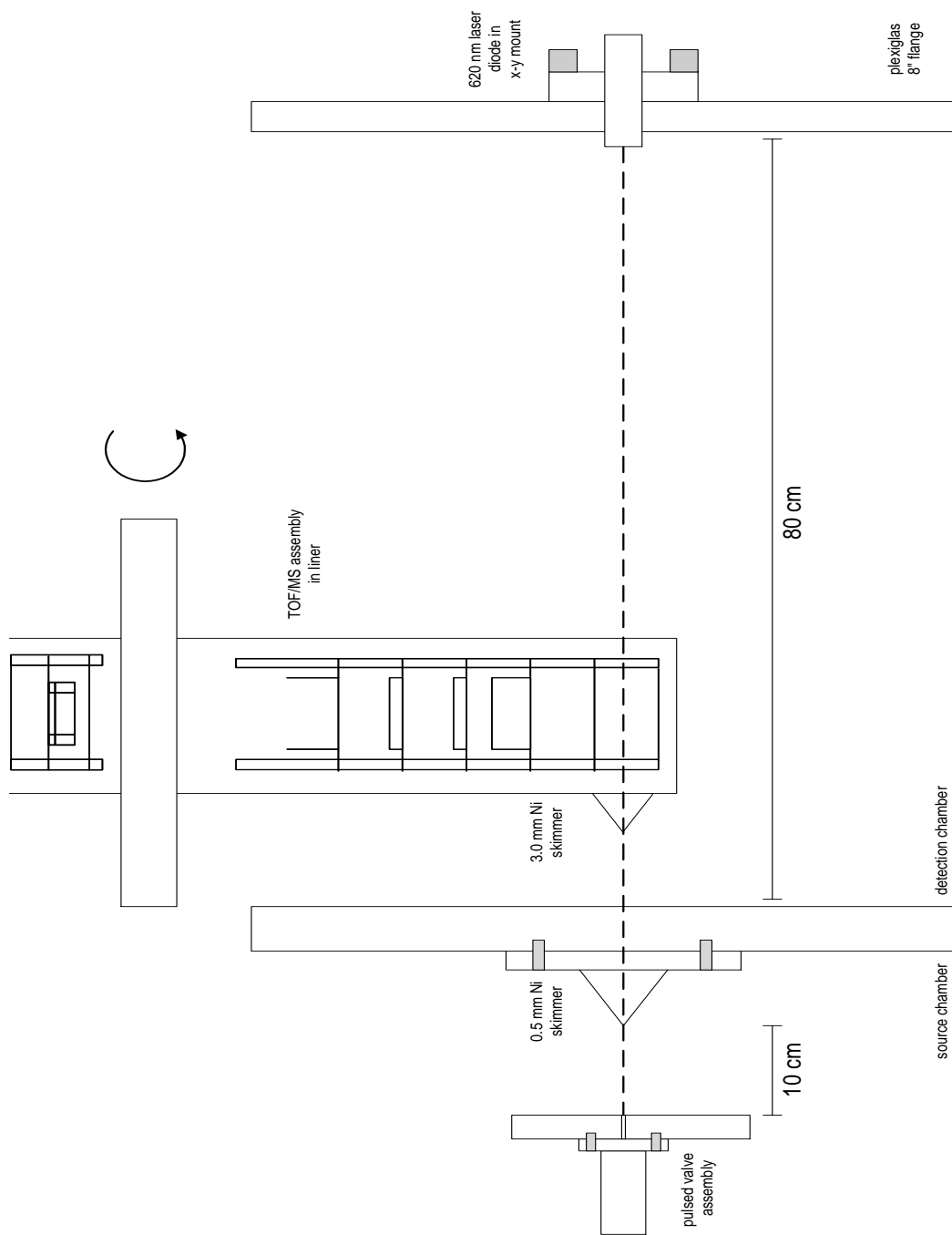
Figure 2-6: Schematic of molecular beam/detector alignment using red laser diode mounted on x-y flange. Alignment is facilitated by back-propagating the laser light through the two skimmer apertures to the pulsed valve nozzle opening. The TOF/MS assembly can be rotated on its flange to permit alignment with the fixed skimmer inside the source chamber.
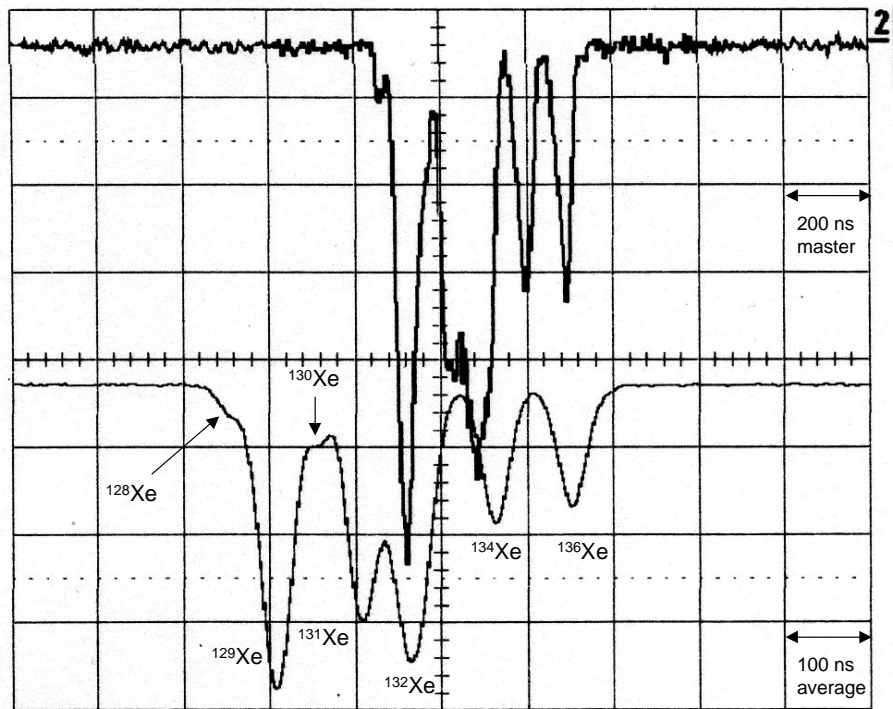
Figure 2-7: Mass spectrum of Xe as seen from oscilloscope. Top trace is main mass channel from one laser shot with horizontal grid divisions of 200 ns; bottom trace is 2× zoom of top trace with 40-shot averaging and grid divisions of 100 ns.

Table 2.2: Natural abundances of major (>1%) Xe isotopes.

Isotope	Natural abundance (%)
^{128}Xe	1.91
^{129}Xe	26.4
^{130}Xe	4.1
^{131}Xe	21.2
^{132}Xe	26.9
^{134}Xe	10.4
^{136}Xe	8.9

that the maximum m/z at which two adjacent mass peaks are resolvable is at least 140. The R. M. Jordan Co. instrument is designed for resolution of m/z $\leq$ 300, although this can be extended to 1000 under certain circumstances [33]. Since the target molecules in the majority of our experiments have m/z <80, a resolution of 140 is certainly sufficient. The optimum operating voltages for this experiment are summarized in Table 2.3. In our experience, these voltages can be used in a number of ion detection experiments with only small tweaks. The voltages themselves are provided by a high voltage power supply (R. M. Jordan model D-603) that was specifically designed to provide multiple HV outputs for a TOF/MS system. While the initial experiments used a continuously present extraction (A1-A2) voltage of *approx* 150 V, this may not always be desirable, as certain types of states (e.g. Rydberg states) would show a small Stark shift if laser excitation occurs when an electric field is present (150 V/ 1.27 cm plate spacing = 118 V/cm) [34]. To prevent Stark mixing, a high voltage pulsing circuit can be applied to repel the cloud of ions formed in the extraction region, only after the laser pulse has terminated. The R. M. Jordan Remote Pulser is capable of producing variable duration pulses with voltages of up to 400 V on top of a continuous HV bias input of $\leq$1500 V.

In its original configuration, the TOF/MS stack assembly was as shown on the left side of Fig. 2-9. An additional plate was later added to the stack (see right side of 2-9) to facilitate the use of pulse-field ionization (PFI). PFI is a technique used to ionize selectively high-lying electronic (Rydberg) states which lie near the

Table 2.3: Optimum TOF voltages for Xe (2+1) ionization

AREF power supply output	Volts
VA1 (Repeller Plate)	1250
VA2 (Extraction Grid)	1050
VXY (X-deflector Plate)	5
VR1 (Focus Einsel Tube)	-95
VR2 (Acc. Grid + Liner)	0
MCP Bias	-1500

first ionization potential (IP). The ionization potential can effectively be reduced by a factor proportional to the electric field strength, e.g. IP depression $= 6.1 \times \sqrt{F}$ [34,35]. For a field of 150 V/cm, the IP is depressed by approximately 75 cm^{-1}, which corresponds to a n* of $\approx$40 (see Fig. 2-8). Higher PFI voltages can be used, but if $F > 200V$ the standard system voltages no longer meet the space-focusing criterion of the TOF/MS system, as described earlier, and no signal will be detected. The additional plate (M) allows the collected ions to be refocused over a larger range of F by ensuring that they are adequately accelerated into the flight tube. In typical PFI operation, plates A1 and M are held at the same voltage (500 - 2000 V) while plate A2 is held at a fixed 1200 V. A custom HV pulser circuit designed by Dr. Stephen L. Coy provides a square wave pulse of variable length and amplitude (0 - 1000 V). Reliable space-focusing was demonstrated with pulse amplitudes as high as 500 V, with A1 and M at $\approx$ 700 V. This corresponds to an IP depression of $\approx$136 cm^{-1}, which would allow access to effective principal quantum numbers as low as $n^* \approx 28$ in CaCl.

A somewhat simpler method of performing PFI involves the use of a small, MCP-based detector that is placed normal to the molecular beam axis. Such a detector was designed and built by Dr. Sergey Panov, and is essentially a shielded MCP stack assembly with two grid plates for field ionization (see Fig. 2-10). When the small PFI system was operational, the grid plates for the main TOF/MS system were grounded to minimize external fields. Unfortunately, despite repeated attempts, no CaCl molecular signals were obtained with the small detector, although signals from
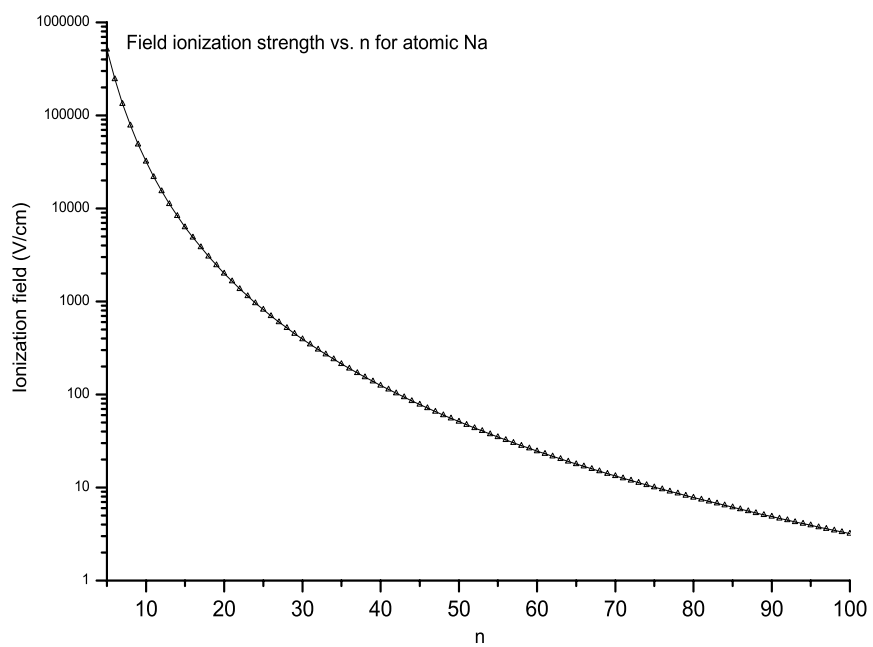
Figure 2-8: Electric field strength necessary to ionize atomic Na at various n levels, from Ref. [3].

original ion extraction
assembly

pulsed-field ionization
(PFI) modification

X-deflector

Einsel tube

focus Einsel tube

acceleration grid
Einsel tube

extraction grid (A2)

PFI acceleration grid (A2)

extraction grid (M)

repeller plate (A1)

0-10 V

90-100 V

500-1500 V

600-1500 V

1.27 cm

0-10 V

90-100 V

900-1500 V

400-1500 V

400-1500 V

440-1700 V

< 2 s

time

1.00 cm
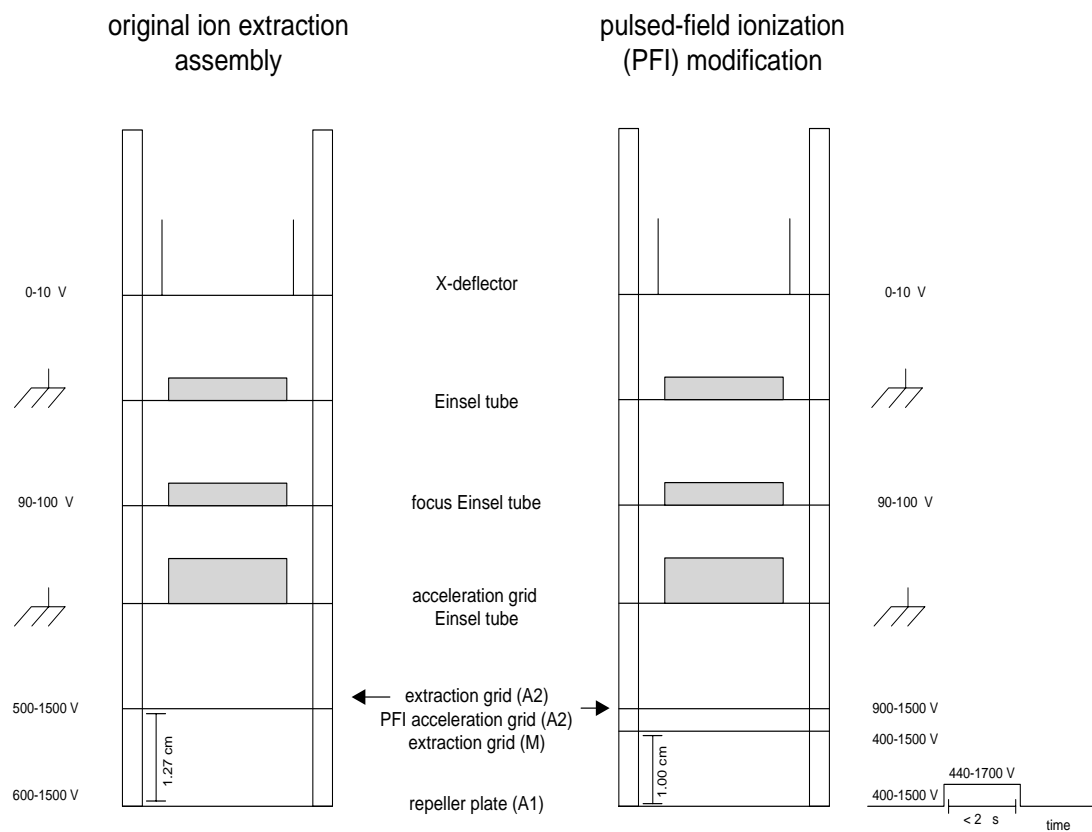
Figure 2-9: Original and modified ion extraction assembly. Plate M was added to the original R. M. Jordan design to facilitate pulse-field ionization (PFI) experiments.
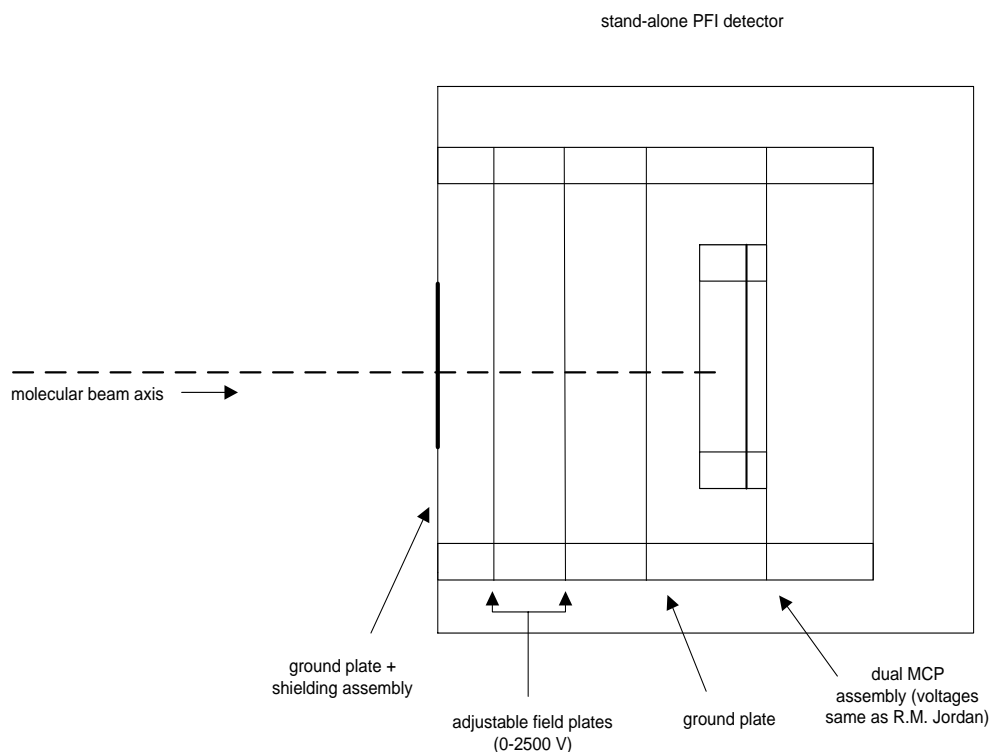
Figure 2-10: Compact PFI detector designed by Dr. Sergey Panov.

ablation by-products have been observed at high F. A number of theories have been advanced to explain the lack of molecular signal: (1) external field gradients which prematurely ionize the already highly excited Rydberg molecules; (2) rapid nonradiative decay into dissociative and autoionizating channels; and (3) misalignment of the molecular beam. Of these possibilities the second is currently considered the most likely candidate. The likelihood of beam misalignment is low considering the thoroughness of the alignment procedure (see above section). While some stray fields are likely present in the apparatus, careful grounding of surfaces should have minimized stray field production. If reason (2) is correct, this is a molecule-specific problem and would yield different results in another molecule which cannot predissociate, such as BaF.

2.2.7 Laser systems

Commercial pulsed laser systems were exclusively used in the experiments performed in this work. Their physical layout on the optical tables is shown in figure 2-11. Two Scanmate 2E dye lasers (0.12 cm^{-1} linewidth without intracavity etalon, 0.03 cm^{-1} with etalon) were simulataneously pumped by either the first harmonic (532 nm) or the second harmonic (355 nm) of a Spectra-Physics GCR-290 injection-seeded Nd:YAG laser operating at a fixed 20 Hz repetition rate. While the GCR-290 is capable of producing over 1 J per 5-7 ns pulse at 532 nm, the dye lasers are designed to handle a maximum $\leq$ 250 mJ/pulse, and were typically operated at half of this amount. The GCR-290 contains a cw-diode Nd:YAG laser used as an injection-seeding mechanism to promote single-mode operation and reduce shot-to-shot fluctuation [36]. According to Spectra-Physics, the GCR-290 has the best shot-to-shot stability when operated at maximum output power. In order to avoid the massive optical damage this would bring to the dye lasers if the full power were passed to them, small adjustments to the half-wave plate inside the GCR-290 were made. This changed the percentage of Nd:YAG fundamental (1064 nm) light allowed to go through the harmonic conversion process, and hence the total output power. The residual unneeded light was harmlessly dumped into a specially designed beam stop (Spectra-Physics #BD-1). Nd:YAG laser power was measured by a high-power pyroelectric detector developed by Ophir Optronics (model #30(150)A-P-HE) after being split by a high-power Nd:YAG 50-50 beamsplitter (CVI Optics Corp. #BS1-532-50-2037-45S).

One of the Scanmate 2E lasers was permanently equipped with a BBO-frequency doubling unit (Lambda Physik Scanmate UV extension) which allowed production of UV light in the 205-400 nm range. Another crystal tracking unit was purchased to allow the other dye laser the same capability, and can be integrated into the system as needed.

Each dye laser is controlled by a computer program written by Lambda Physik. Communications are passed through a fiber-optic cable between the standard DOS-equipped PC and a proprietary motor control logic unit inside the dye laser housing.
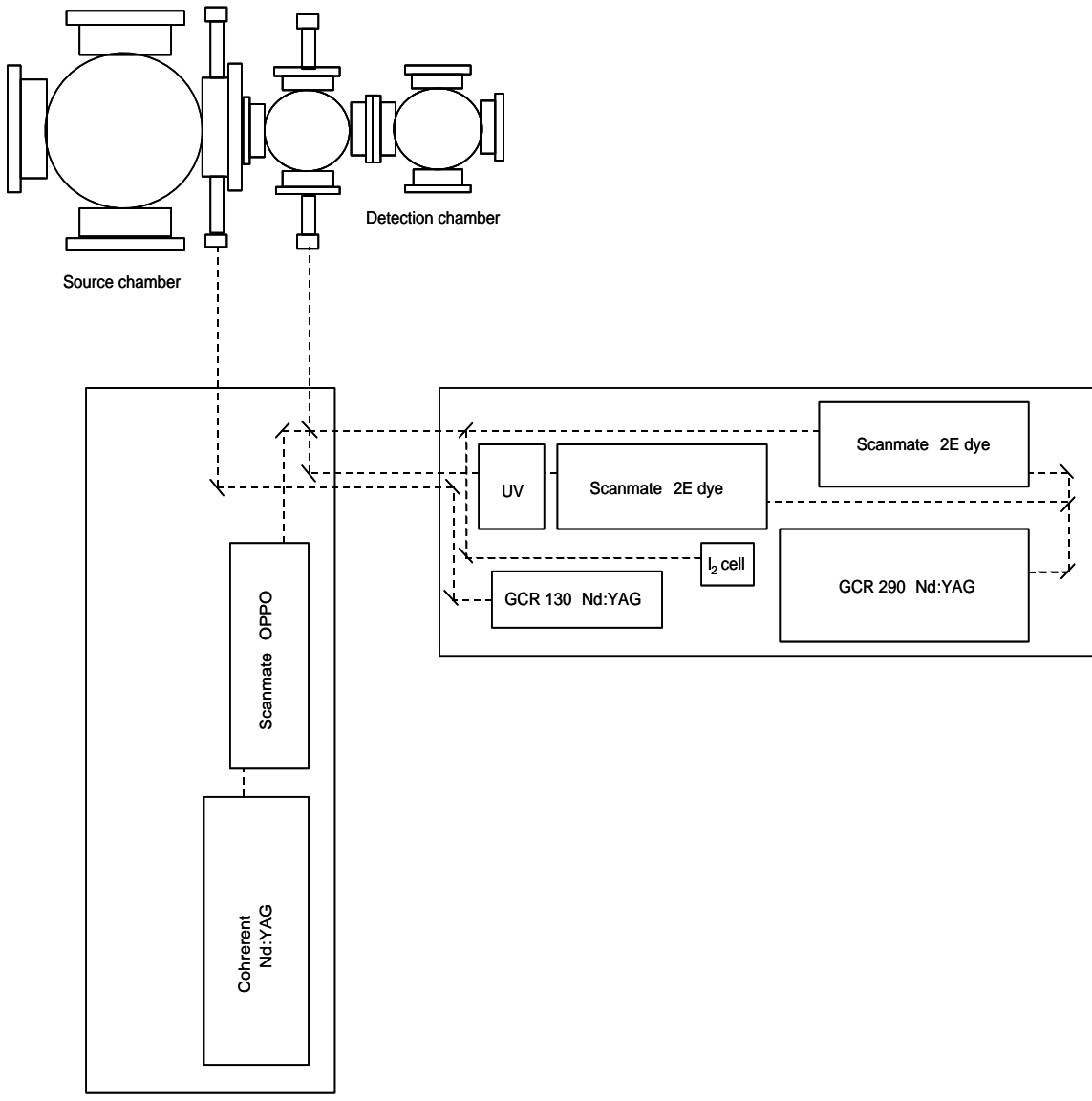
Figure 2-11: Physical layout of vacuum chamber and laser systems.

Great care must be taken to avoid damaging the fragile fiber optic connection cable, as it is fairly expensive to replace ($\approx$\$800). The only method to control the laser is through the provided software, and Lambda-Physik has refused to provide the source code [37]. So far this has not been a major limitation to the development of computer-controlled experiments (see next section). The Scanmate control software allows scanning over a specified wavelength range in either discrete steps (Burstscan mode) or in a particular length of time (Continuous scan). The Burstscan mode is very useful for data acquisition since the laser will wait for any desired number of trigger pulses before advancing to the next resolution element.

The output from each of the dye lasers is passed through an identical adjustable telescope assembly on a 20-cm long railing, which allows the beam diameter to be easily expanded to allow maximum overlap in the molecular beam chamber in the case of double-resonance experiments or focused tightly when hunting for an elusive ion signal. The telescope lenses have an f_1 of -50 cm and an f_2 of 6 cm (15 cm for the "probe" laser). The 3-inch VUV grade CaF_2 (Janos Optics #A1405V761) windows on the molecular beam ports will pass laser light of wavelength down to 125 nm.

Absolute calibration of laser frequency is achieved by comparing a simultaneously acquired I_2 fluorescence excitation spectrum to a standard reference atlas [38]. A small amount of either the pump or probe laser light is picked off by a transparent wedge and passed through an adjustable iris to an anodized aluminum block which houses a sealed quartz tube that contains I_2 crystals. The fluorescence signal is recorded at the bottom of the aluminum block by a Hamamatsu R928 photomultiplier tube biased at -600V and is monitored by oscilloscope (LeCroy #LC574A).

In addition to the Lambda-Physik Scanmate 2E dye lasers, the laboratory also has a Lambda Physik OPPO (Optical Parametric Power Oscillator) system which is essentially a modified Scanmate dye laser. The OPPO contains a short (10 cm) optical cavity containing a BBO crystal and two highly reflective mirrors instead of a typical dye amplifier stage. The pump beam in this case is the third harmonic of a Coherent Infinity 40-100 variable repetition rate Nd:YAG laser. The parametric process proceeds on the basis that the cavity that contains a nonlinear crystal is

resonant at both "signal" and "idler" frequencies, and the relationship between the two frequencies is described by:

$$\frac{1}{\lambda_{pump}} = \frac{1}{\lambda_{signal}} + \frac{1}{\lambda_{idler}}. \tag{2.6}$$

Since the pump frequency is fixed, only one of the other frequencies needs to be changed to affect the other. The seeding wavelength for the signal process is provided by a standard Scanmate dye oscillator and pre-amplifier stage, and the typical output energy of 100 μJ/pulse easily allows this wavelength to become the dominant resonance in the cavity. Since the oscillator/pre-amplifier stage is restricted to dyes in the visible range below $\approx$600 nm, the resultant idler frequency is limited in the infrared to a range of $\approx$1000-2500 nm. While the OPPO system requires a fair amount of experience to successfully align, it is nevertheless a valuable tool for providing additional resonance steps in the visible or infrared.

Photoablation of target metal rods (as described in a previous section) is accomplished by focusing the third harmonic (355 nm) of a Spectra-Physics GCR-130 laser operating at 20 Hz. Even though the GCR-130 is rated at the lowest power output of the entire Spectra-Physics GCR line, it easily manages 100 mJ/pulse at 355 nm, which is more than sufficient to pump a single dye laser (although it should be noted that the GCR-130 does not have the injection seeder present in the GCR-290). The GCR-130 is typically operated at 15 mJ/pulse to ablate Ca, and it has been observed by us and others that more power does not necessarily increase product ion signal [15]. The GCR-130 as originally purchased was only able to produce the second harmonic (532 nm), but the appropriate crystals and beam separators for third harmonic generation were acquired in the event that the GCR-130 would be needed as an emergency back-up for pumping a dye laser. This capability could also be advantageous in its present use, since according to Prof. Michael Duncan the use of UV light for photoablation is preferred over other frequencies [39]. The explanation for that observation is unknown, but our initial experience indicated that 532 nm photoablation is indeed less stable than 355 nm, and the third harmonic has been used ever since.

2.2.8 Timing, Computer Control, and Data Collection

The rate limiting step for data collection in our apparatus is the 20 Hz duty cycle of the Spectra-Physics Nd:YAG lasers. To successfully acquire signal, a number of events must be synchronized to occur with each laser pulse:

- Firing of flashlamp for photoablation laser

- Firing of flashlamp for pump and probe laser

- Opening of pulse valve

- Extraction pulse for collection of ions in TOF-MS.

These steps are summarized in the system master timing diagram in Fig. 2-12, and are controlled by programmable delay generators (Stanford Research Systems model DG535). These devices are extremely simple to use and form the heart of the experiment. It is difficult to overstate the importance of these devices in the overall experimental setup. Since conditions for optimal signal production can change by tens of microseconds on a given day, it is essential to have a reliable and convenient way of shifting the relevant delays.

The output signal from the MCP stack assembly at the end of the TOF-MS and the I_2 reference signal are input into a 1 GHz digital oscilloscope (LeCroy model #LC574A) for visualization. The MCP signal is often amplified through use of a high-speed low-noise voltage amplifier (FEMTO Messtechnik GmbH model DHPVA) with variable gain (10-60 dB or 3x to 1000x). The FEMTO amplifier is remarkable for its low noise (2.6 nV/$\sqrt{\text{Hz}}$) and gain flatness (0.15 dB) over a large bandwidth range (DC to 200 MHz).

The LeCroy oscilloscope is used for data collection as well as visualization. A computer program ("SPSCAN") written by Dr. Sergey Panov sends commands through a GPIB controller card (National Instruments #GPIB-PCI) to the GPIB bus on the oscilloscope. The control software performs the following sequence of events:

- Computer reads input time gates for each desired mass channel from datafile *gatesrc*

μs

2000

1000

0 (T_o)

380 μs

T_o + 1050 μs
pulsed valve
trigger pulse

pulsed valve
output profile

T_o + 1280 μs
ablation Nd:YAG
lamp trigger

light output
(trig +188 μs)

T_o + 1460 μs
dye laser/Nd:YAG
lamp trigger

light output
(trig +188 μs)

T_o + 1646 μs
TOF/Electric field
pulse sweep

T_o + 1650-55 μs
Ions detected
via MCP
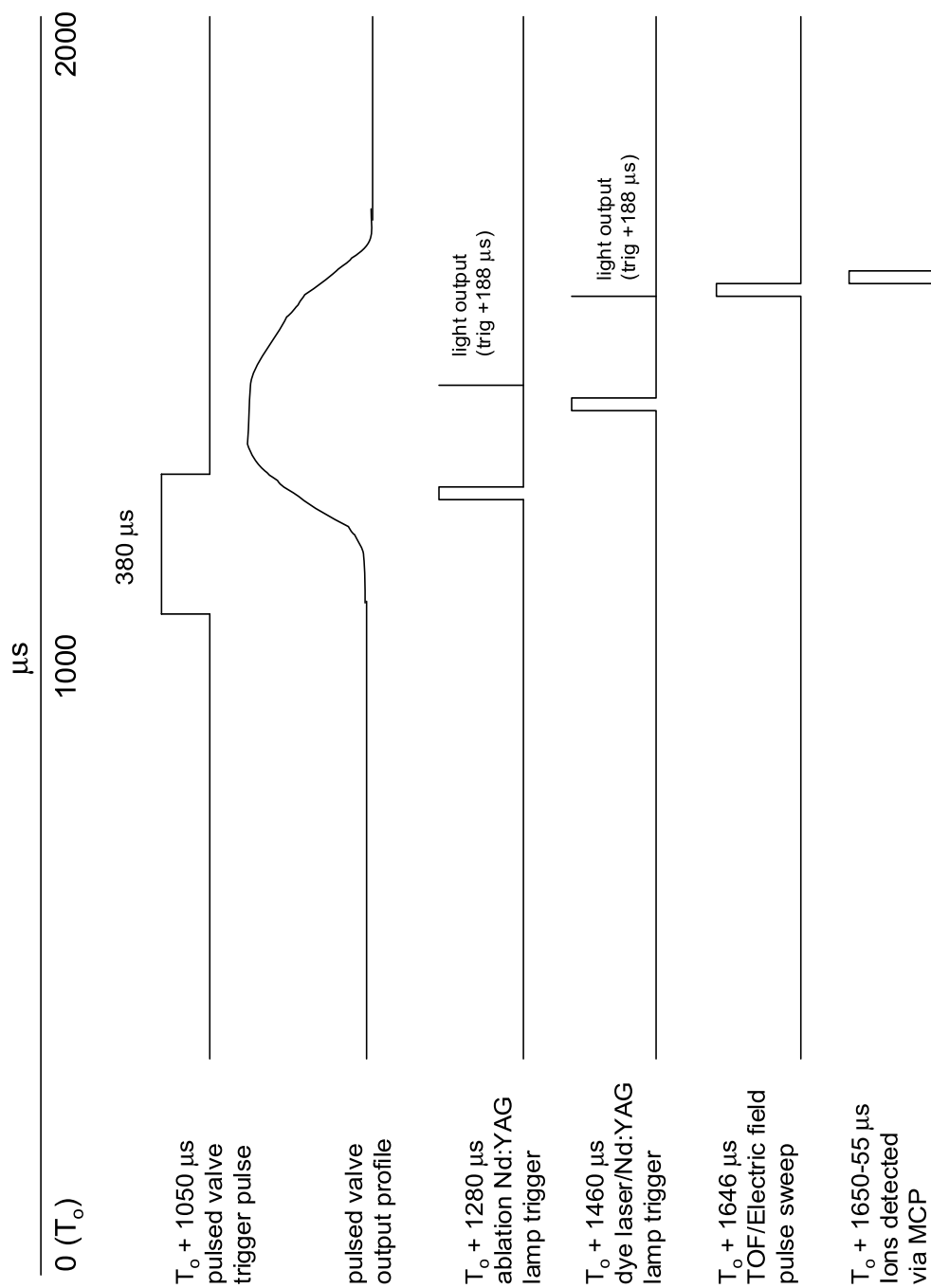
Figure 2-12: Master system timing diagram for REMPI-TOF/MS system. 20 complete cycles occur per second. T_o is defined to be the master clock of the DG535 delay generator. Delays can vary $\pm$ 1% depending on pulsed valve characteristics.

64

- Computer tells oscilloscope to enter remote control mode

- Computer tells oscilloscope to begin averaging of input time gates over a period of n (usually 40) trigger pulses (i.e. laser shots)

- Oscilloscope sends signal that n pulses have been received

- Computer asks oscilloscope for result of averaging n pulses

- Computer sends TTL pulse through parallel port to Scanmate 2E control computer to advance to next resolution element in Burstscan mode

- Appends the average intensity for each mass channel for each step to output datafile with index based on input start, stop, and step data supplied by user in datafile *scanrc*

- Computer ends oscilloscope remote control connection after required number of scan steps have been completed

This arrangement works well provided that certain tasks are performed before-hand: (1) All of the mass channels to be monitored must be visible on the oscilloscope screen before beginning remote control; (2) The peak intensity of the mass channel does not go beyond the scale presently on the screen; 3) The user has used the time cursor feature to determine the appropriate time gate for a particular mass channel and input this data into datafile *gatesrc*; (4) The averaging (Math) mode has been activated for each of the target input channels (e.g. TOF/MS and I_2); (5) the scan parameters have been input into the Scanmate control computer and the laser is ready to accept TTL pulses in Burstscan mode.

An additional feature of this data acquisition technique involves the method by which the data is stored. The data acquisition computer running Linux has a direct connection via our internal TCP/IP network to the group file server, and the data file is actually written on the file server itself during a scan using the Network File System (NFS). This situation provides many advantages: (1) the data file itself is backed up immediately on the file server's multiple-hard drive mirroring (RAID)

array; (2) the data file is immediately available for visualization with any standard plotting program, e.g. *gnuplot* or *Origin*; (3) our group network is configured in such a way that the connection would be maintained even with catastrophic failure of the chemistry department network.

Sample input and output files for SPSCAN are provided in Appendix A.

2.3   Initial Molecular Beam Experiments

A number of initial experiments were performed in the beam apparatus to determine its operational characteristics. The general idea was to begin observations of atoms and gradually work up to molecules, initially produced without photoablation. In order, these "stepping-stone" experiments consisted of:

(1) Xe Resonance-Enhanced Multi-Photon Ionization (REMPI) for TOF/MS mass resolution determination (discussed in section 2.2.6).

(2) Cl_2 photolysis + Cl REMPI

(3) NO A $^2\Sigma^+$ - X $^2\Pi$ REMPI (for determination of extent of rotational cooling without photoablation)

(4) CaCl D $^2\Sigma^+$ - X $^2\Sigma^+$ REMPI (for determination of extent of rotational cooling with photoablation)

2.3.1   Chlorine Photolysis

To determine the temporal separation of chlorine peaks in our TOF/MS spectrum as well as the relative ease of ionizing atomic chlorine, an experiment was designed to scan through a transition of atomic Cl. The halogen carrier in this case was a mixture of 2.5% Cl_2 in N_2, so ionization of atomic chlorine was necessarily proceeded by photolysis of the chlorine molecule by focused dye laser UV output at energies ≈ 1.5mJ/pulse:

$$Cl_2 + UV \longrightarrow 2Cl. \tag{2.7}$$
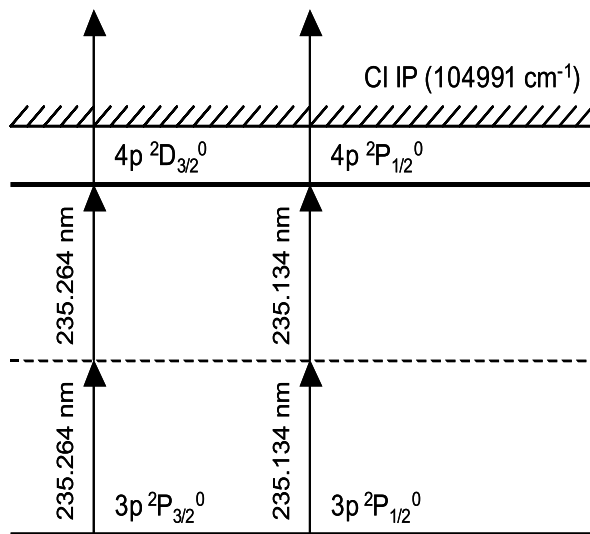
Figure 2-13: (2+1) REMPI transitions for Cl showing excitations from ground level $^2P^0_{3/2}$ and spin-orbit-excited level $^2P^0_{1/2}$ to 4p levels.

The ionization of atomic Cl occurs by two-photon-allowed absorption at a resonance line followed by a absorption of a third photon which takes the total energy above the chlorine ionization limit (104 991 cm^{-1}) [40, 41]. This one-color three-photon Resonance-Enhanced Multi-Photon Ionization (REMPI) technique is a well-known, highly versatile way of producing atomic and molecular ions [42]. The resultant spectrum, which includes the observed 4p $^2P^0_{1/2}$ ← 3p $^2P^0_{1/2}$ and 4p $^2D^0_{3/2}$ ← 3p $^2P^0_{3/2}$ transitions, is shown in Fig. 2-14.

2.3.2 REMPI of NO

The NO A $^2\Sigma^+$ - X $^2\Pi$ transition of has been extensively studied in molecular beams [43–45]. Our goal in using it was to optimize experimental parameters for molecule detection as well as to determine the effective rotational temperature T_{rot} in our

235.134 nm
$4p\,^2P^{\,0}_{1/2} - 3p\,^2P^{\,0}_{1/2}$

235.264 nm
$4p\,^2D^{\,0}_{3/2} - 3p\,^2P^{\,0}_{3/2}$

laser wavelength (nm)
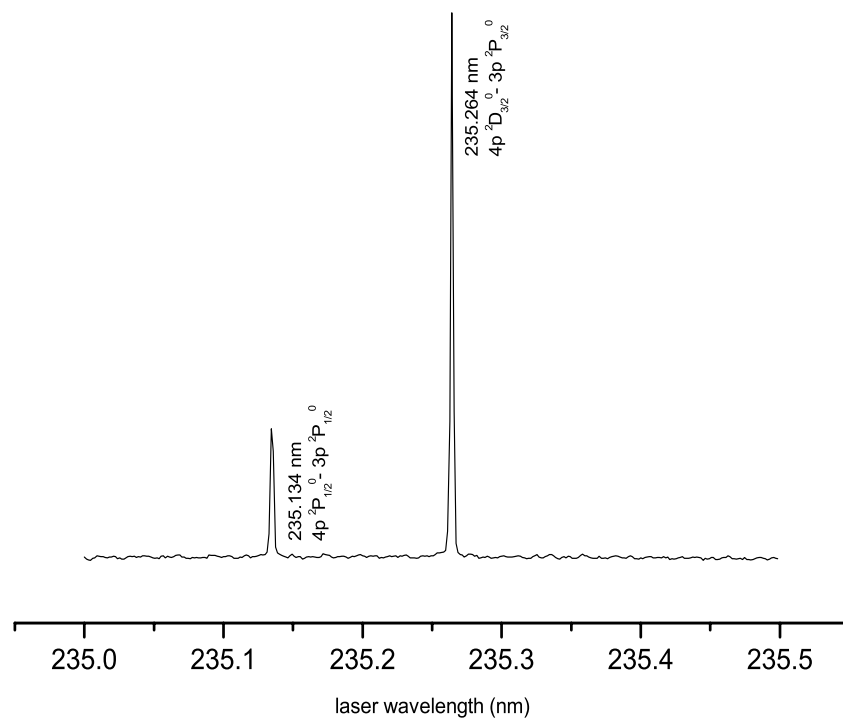
Figure 2-14: (2+1) REMPI spectrum of Cl. Transition energy is 2× laser wavelength.
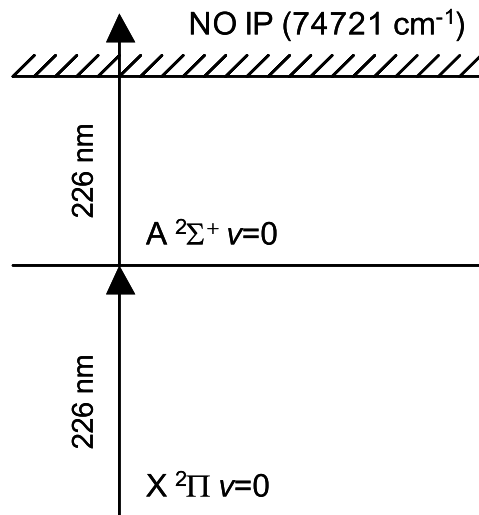
Figure 2-15: Energy level diagram for the $A\ ^2\Sigma^+$ - $X\ ^2\Pi$ transition of NO.

molecular beam for a molecule not produced by photoablation. The level scheme for this experiment involved a one-color two-photon ionization to the (0,0) band near 226 nm (see Fig. 2-15). Experimental spectra were computed using the program SPECSIM with the known constants for the A and X states at T_{rot} of 1,2,5 and 100 K [46,47]. The closest agreement with our observed spectrum is at 5 K (see Fig 2-16). The UV laser power used in this experiment was $\approx$1 mJ/pulse.

2.3.3   REMPI of CaCl

The $D\ ^2\Sigma^+$ - $X\ ^2\Sigma^+$ system of CaCl had been previously studied by our group in a first-generation molecular beam machine designed and built by Dr. Chris Gittins in the early 1990s [15,22]. Our goal was to optimize the photoablation technique described in Section 2.2.5 for a molecule of research interest. The $D\ ^2\Sigma^+$ state was chosen for the initial CaCl experiments for the following reasons: (1) $^2\Sigma^+$ - $^2\Sigma^+$ transitions are easily
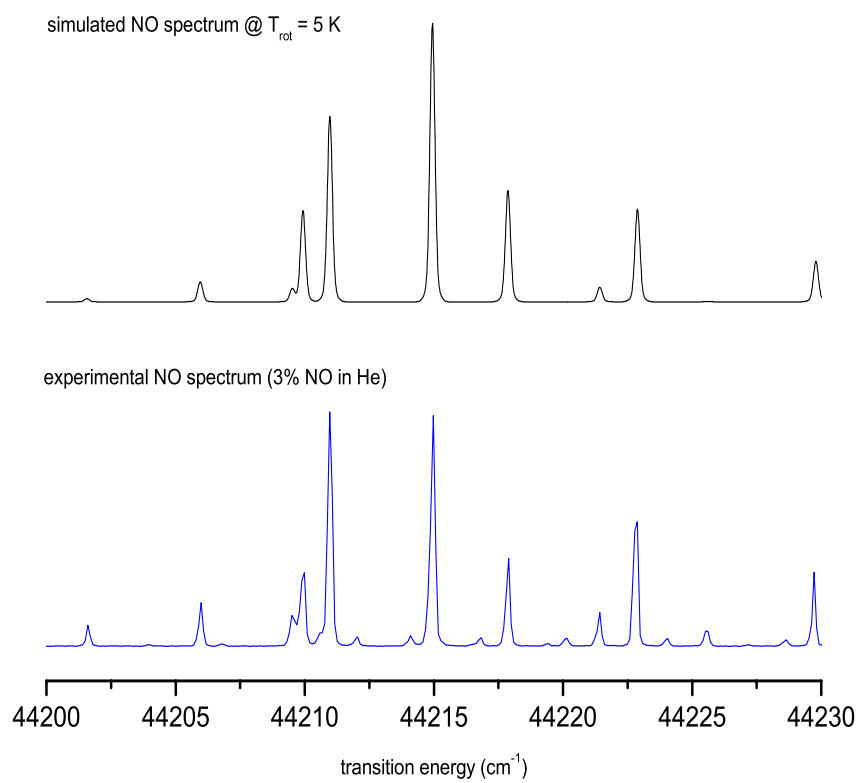
Figure 2-16: REMPI spectrum of the A $^2\Sigma^+$ - X $^2\Pi$ transition of NO.
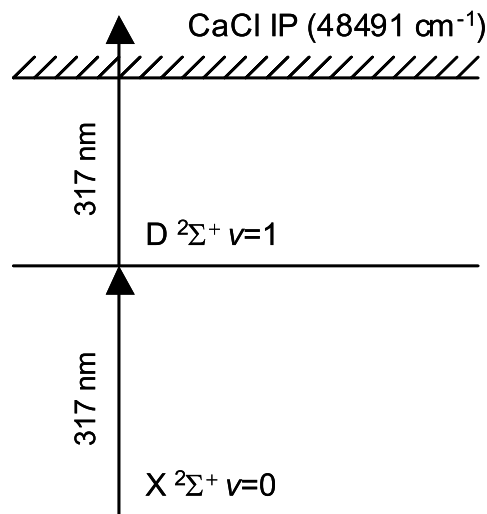
Figure 2-17: Energy level diagram for the $D\ ^2\Sigma^+$ - $X\ ^2\Sigma^+$ (1,0) transition of CaCl.

understood; (2) the $D\ ^2\Sigma^+$ state is considerably higher than halfway to the ionization potential of CaCl (48 491 cm^{-1}), facilitating ioniziation by straightforward one-color two-photon (1+1) REMPI (see Fig. 2-17); (3) successful signal optimization would allow immediate acquisition of new spectroscopic data for CaCl via the D-state for OODR (Optical-Optical Double Resonance) experiments as well as direct excitation to electronic states in the D-state energy region.

The optimum Nd:YAG laser power at 355 nm for Ca photoablation was eventually determined to be 7 mJ/pulse. The optimization of CHCl$_3$ concentration was discussed in Section 2.2.5. The optimal TOF/MS voltage parameters were very similar to those used for earlier experiments (see Table 2.3).

Experimental spectra were computed using the program SPECVIEW with the known constants for the D and X states at various values of T$_{rot}$ [6,48]. SPECVIEW differs from the earlier program SPECSIM in the ability to interactively change the

71

values of the relevant spectroscopic constants "on-the-fly" to quickly match the experimental spectrum. The closest agreement for our observed spectrum is at 15 K (see Fig. 2-18). We would expect the effective T_{rot} for CaCl to be higher for NO since the photoablation process requires hot Ca plasma to react with a halogen carrier to form CaX molecules, and it is likely that the cooling process would not be as complete for products formed in this manner. Spectra obtained at 15 K are nevertheless very useful for OODR experiments, as will be discussed in subsequent chapters.

CaCl theoretical spectrum @ T_{rot} = 15K

R_{21} (N")

CaCl experimental spectrum

transition energy (cm^{-1})
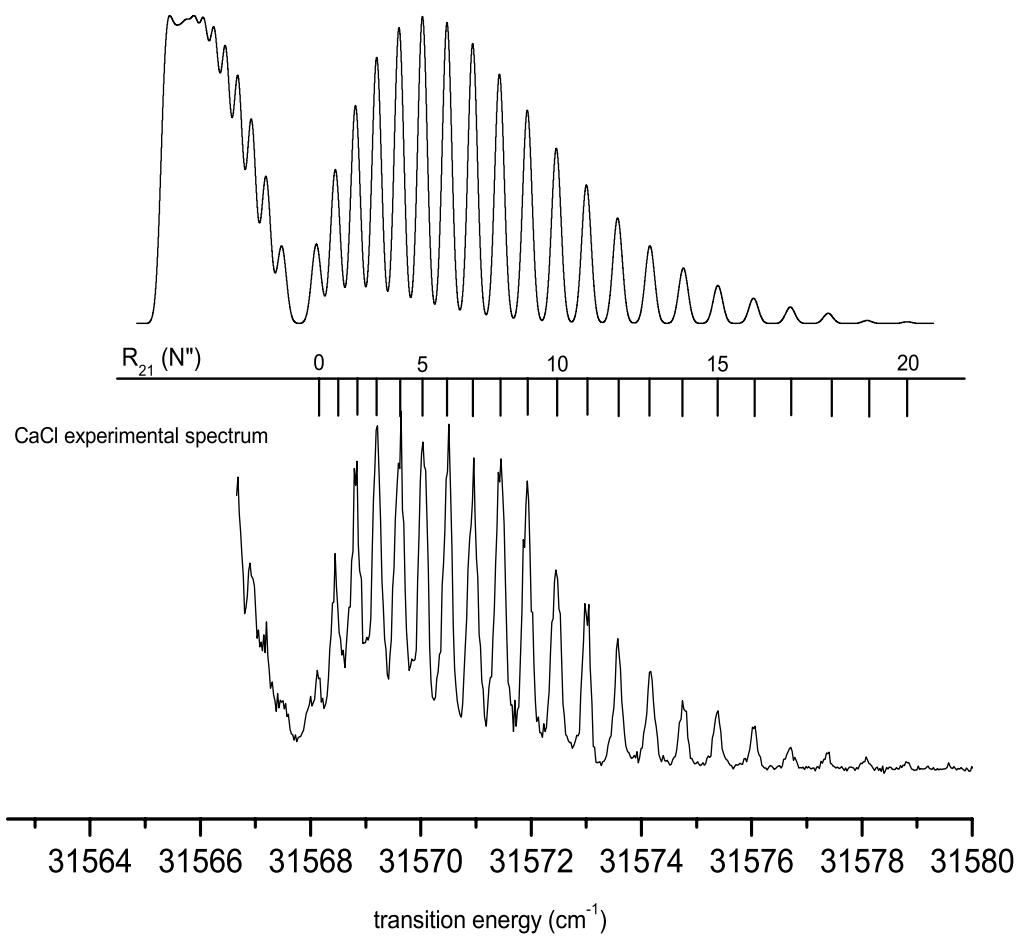
Figure 2-18: (1+1) REMPI spectrum of the Ca^{35}Cl D $^2\Sigma^+$ - X $^2\Sigma^+$ (1,0) transition with rotational assignments for R-branch.

Chapter 3

CaCl Survey Spectra in the n* = 3-7 Region

3.1   Introduction

Earlier studies of CaCl by our group through both ionization (REMPI) and fluorescence-based methods indicated that the low-n* (n* $\approx$ 3-7) Rydberg states are predissociated [16, 22]. Indeed, the main differences in the Rydberg spectra of CaF and CaCl arise from the fact that the dissociation limit of CaCl lies much farther below its first ionization limit than that of CaF: [IP$_1$ - D$_o$ = 2 800 cm^{-1} (n* $\approx$ 6.26) for CaF, 15 300 cm^{-1} (n* $\approx$ 2.68 for CaCl). Thus we would expect the low-n* Rydberg states of CaCl to be extensively predissociated by the two repulsive or weakly bound $^2\Sigma^+$ and $^2\Pi$ states which dissociate to the $M(^1S)+X(^2P)$ neutral atoms (see Fig. 3-1).

The experimental results, as reported in the earlier studies, are largely fragmentary below n* $\approx$ 5.75. We would normally expect (and do observe at higher-n*) Rydberg states corresponding to one of six core-penetrating series (see Table 3.1). After the completion and optimization of the 3rd generation molecular beam apparatus detailed in the previous chapter, a systematic study of the low-n* region was initiated to quantify, if possible, the extent and mechanisms of the predissociation.
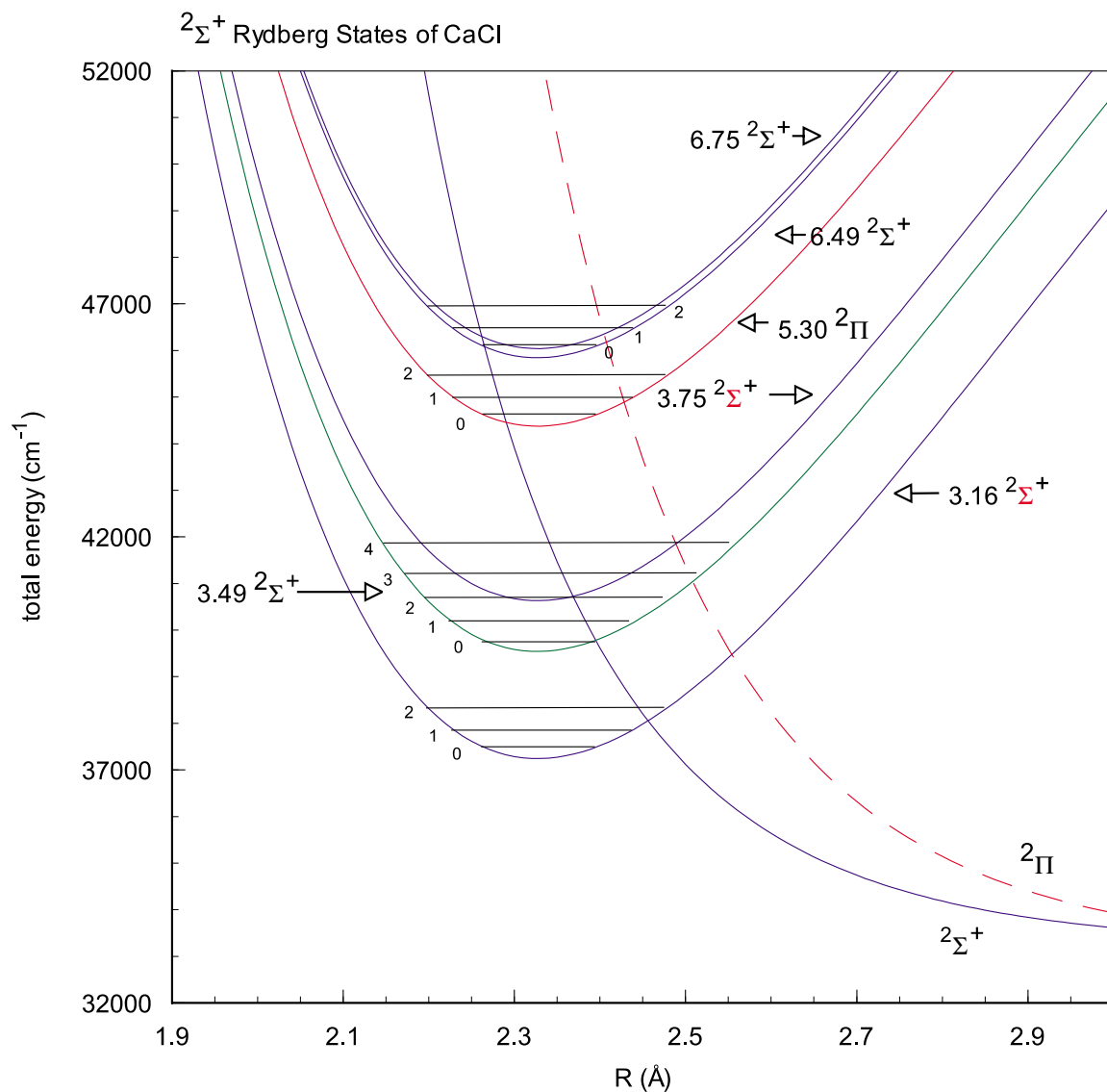
Figure 3-1: Diabatic potential energy curves for selected $^2\Sigma^+$ Rydberg states and repulsive states. The position of the $^2\Sigma^+$ repulsive state was determined by a linewidth analysis described in Chap. 5, while the position of the $^2\Pi$ repulsive state is qualitative and based on electron repulsion arguments and observed vibrational levels of $^2\Pi$ states (see Fig. 3-2 and Section 3.3.2)

.
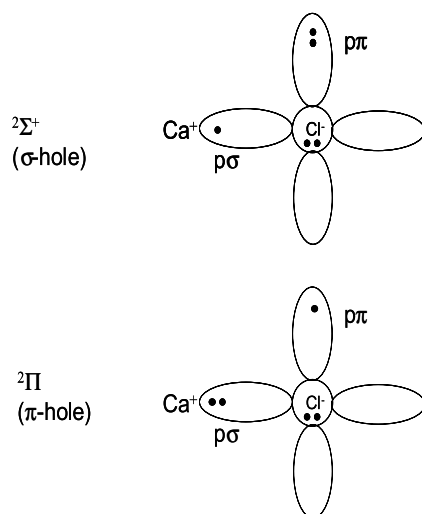
Figure 3-2: Molecular orbital representation of $3p\pi^{-1}$ and $3p\sigma^{-1}$ hole configurations of CaCl giving rise to $^2\Pi$ and $^2\Sigma^+$ repulsive states which dissociate to $M(^1S)$ + X (^2P) neutral atoms. The $^2\Pi$ repulsive state is expected to be more repulsive than the $^2\Sigma^+$ repulsive state in the n* = (3 - 8) region since the electron density pointing toward Ca is larger for the π^{-1} configuration.

3.2 Experimental Details

To simplify experimental matters, (1+1) and (1+1') ionization schemes were chosen to access Rydberg states directly from the $X\ ^2\Sigma^+$ ground state (see Fig. 3-3). Sufficient energy for ionization was acquired through absorption of a second UV photon (two-photon one-color REMPI) or through absorption of a second fixed-wavelength (typically 545 nm) photon (two-color two-photon REMPI). Scanning of the entire n* $\approx$ 3-7 region required generation of UV laser light over the range 215 - 268 nm (37 250 - 46 500 cm^{-1}), and was accomplished by the use of a frequency doubling unit equipped with BBO crystals in a Scanmate 2E dye laser. Two different BBO crystals were required to cover the entire range. Typical pulse energies were 500 μJ/pulse for the UV laser and 300 - 700 μJ/pulse for the 545 nm visible laser. A fairly coarse step size of 0.010 nm (in UV output) was used in the Burstscan mode scans of the Scanmate dye laser. This choice of step size corresponded to a resolution element of $\approx$0.40 cm^{-1}, and was considered to be an acceptable compromise between scan duration over such a large energy region and a desire to extract the most spectroscopic information possible. Since the rotational constants for the Rydberg states and the electronic ground state are small and similar (0.164 cm^{-1} and 0.152 cm^{-1}, respectively) the bands are expected to be rather compact. It was never a goal to extract rotational information from these survey spectra; they were intended to serve as a "road map" which would track the extent of predissociation and be useful for future experiments.

With typical UV laser energies of 500 μJ/pulse, it was also possible to ionize directly residual Ca atoms in the laser excitation region. This was often observed under typical operating conditions with UV laser light because of the relatively low ionization potential of Ca(49 304.8 cm^{-1}) and the presence of Ca as a by-product of the CaCl photoablation process. One goal of the experiment was to directly observe Ca atoms formed from the CaCl predissociation process. We would expect in this case that the signal in the Ca mass channel would either directly mirror the structure in the CaCl mass channel or perhaps contain molecular features that would be entirely
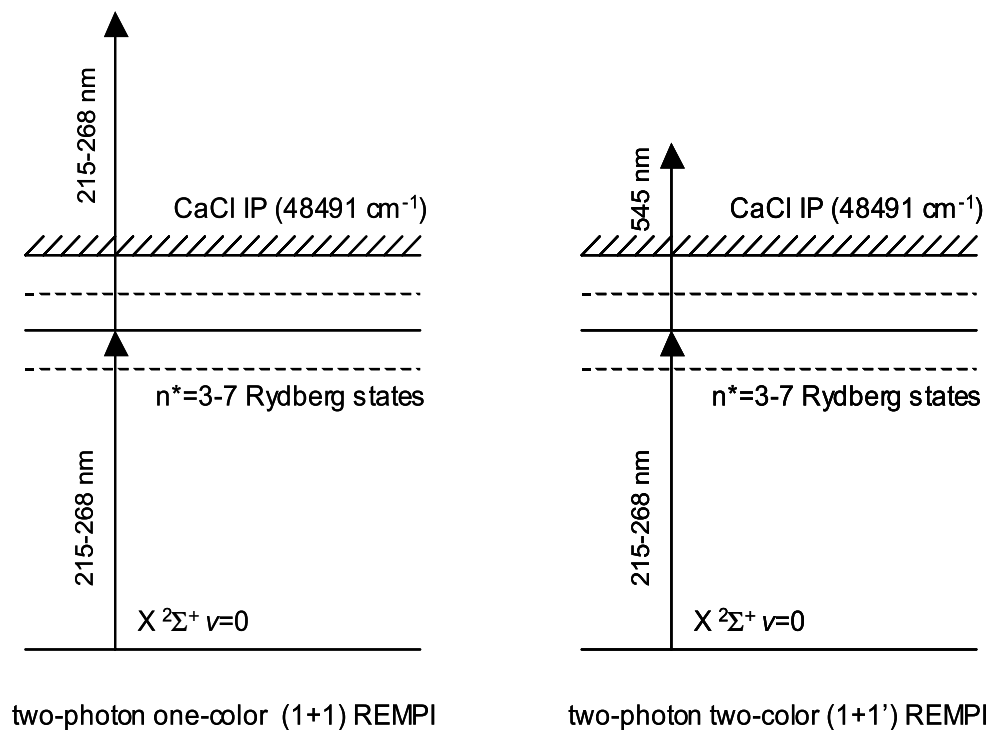
Figure 3-3: Energy level diagrams for pumping schemes used for observation of low-n*
Rydberg series.

missing from the CaCl channel. This effect was observed in a small number of spectral regions through the low-n* region, but Ca-detected molecular features proved to be difficult to reproduce, due to day-to-day fluctuations in the molecular beam and laser flux (see Section 3.3 for more details).

The Time-of-Flight/Mass Spectrometer operating voltages were within the typical operating ranges summarized in Table 2.3. The pulsed extraction electric field was not used in these experiments; a constant differential of ($\approx$100 V/cm) between A1 and A2 was present during the laser excitation pulse.

Unlike other molecular beam experiments discussed in this work, the spectra were calibrated using Ca atomic lines observed during the course of the scans. Often several lines were present in a typical scan; due to the excellent linearity of the Scanmate laser,

Table 3.1: Core-penetrating CaCl Rydberg series with dominant l character [5].

$n^*{}_{obs}(mod1)$	series terminus state	partial atomic character
$0.49\ ^2\Sigma^+$	X	$0.96s + 0.27d$
$0.75\ ^2\Sigma^+$	B	$0.97p + 0.20d + 0.11f$
$0.16\ ^2\Sigma^+$	F'	$0.88d + 0.30f$ - $0.28s$ - $0.21p$
$0.97\ ^2\Pi$	A	$0.99p$ - $0.09d$
$0.30\ ^2\Pi$	C	$0.96d + 0.26f + 0.10p$
$0.11\ ^2\Delta$	B'	$0.99d + 0.16f$

multiply measured spectral features from overlapping scans are typically reproduced within a deviation of no more than one resolution element, or ≈ 0.4 cm^{-1}.

Since chlorine has two comparably abundant isotopes, ^{35}Cl and ^{37}Cl, we were able to simultaneously acquire Time-of-Flight data for Ca^{35}Cl and Ca^{37}Cl, with roughly the (3:1) intensity ratio expected from the natural abundance ratio. The availability of data for both isotopomers proved extremely valuable in establishing assignments for the observed vibrational bands.

3.3   Results and Discussion

3.3.1 $^2\Sigma^+$ states

A surprising number (≈ 97) Rydberg vibrational bands were discovered during our $\approx 10\ 000$ cm^{-1} survey search. The majority of them belong to the $0.49\ ^2\Sigma^+$ series. The n* = 3.49 state stands out for having by far the largest number of observed vibrational bands (see Table 3.3.1). Initially assignments of quantum numbers as high as $v = 9$ in the excited state were considered improbable at best, despite the confirming evidence from the Ca^{35}Cl/Ca^{37}Cl isotope shifts. Several reasons have since been advanced for why the n* = 3.49 state has so many observed vibrational bands. Computed Franck-Condon factors, which typically show a very strong $\Delta v = 0$ preference for Rydberg-valence transitions, show considerable non-diagonal vibrational overlap for the D-X transition see Fig. 3-4). This observation is relevant here since the $D\ ^2\Sigma^+$ state is the n* = 2.49 member of the $0.49\ ^2\Sigma^+$ series, and is expected
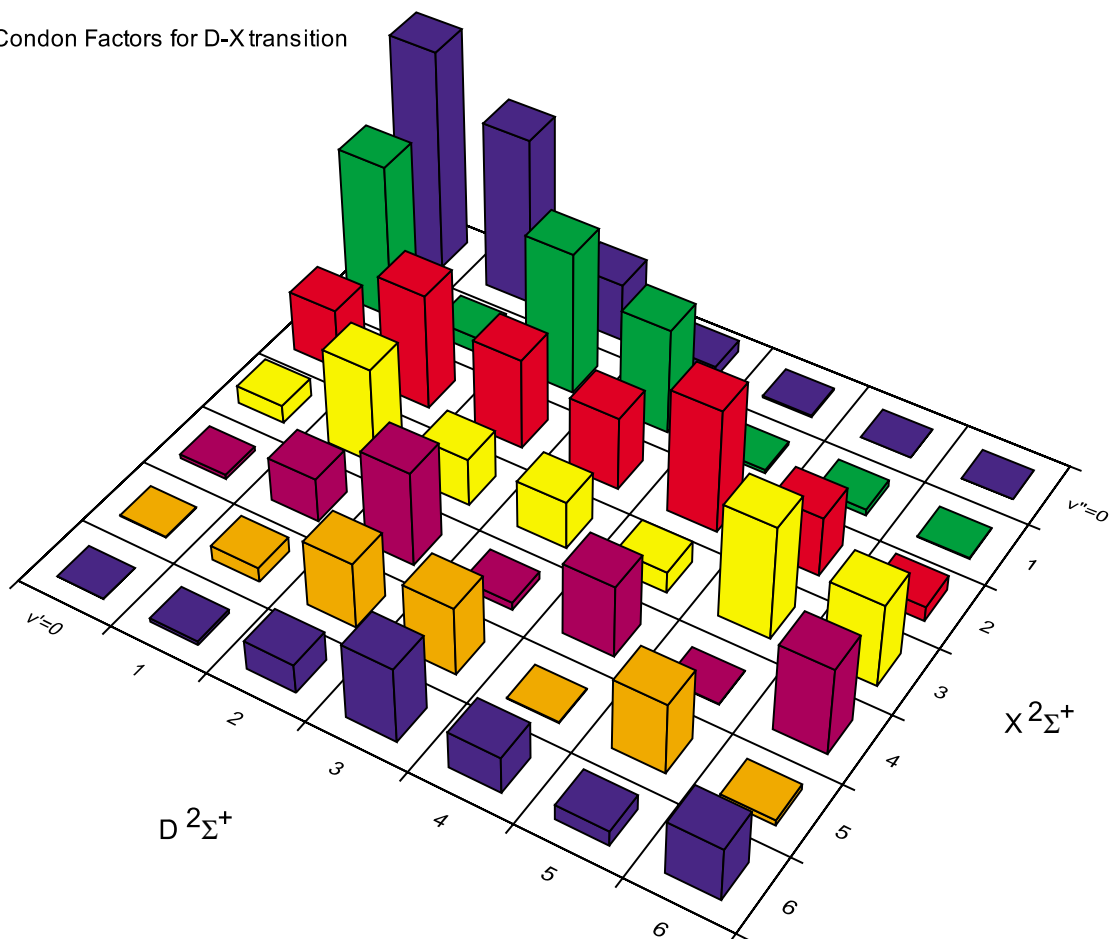
Figure 3-4: Franck-Condon Factors for the D $^2\Sigma^+$ - X $^2\Sigma^+$ trnasition in CaCl. Transitions to n* = 3.49 $^2\Sigma^+$ - X $^2\Sigma^+$ are expected to show similarly non-diagonal (i.e. non $\Delta v = 0$) intensities.

to have rotational and vibrational constants similar to those of the n* = 3.49 state. Recent calculations of transition dipole moments for Rydberg-valence transitions by our theoretical collaborators (Prof. Ch. Jungen and Saïd Roauafi) in Orsay, France show that the strongest dipole moments are for the lowest (n*≤4.49) members of the 0.49 $^2\Sigma^+$ - D $^2\Sigma^+$ transition [49]. Since the ground state is also part of the 0.49 $^2\Sigma^+$ series, similar trends in the dipole moments would be expected for 0.49 $^2\Sigma^+$ - X $^2\Sigma^+$ transitions. Results of the dipole moment calculations from Jungen *et al.* for $^2\Sigma^+$ and $^2\Pi$ series are shown in Figs. 3-5 and 3-6.
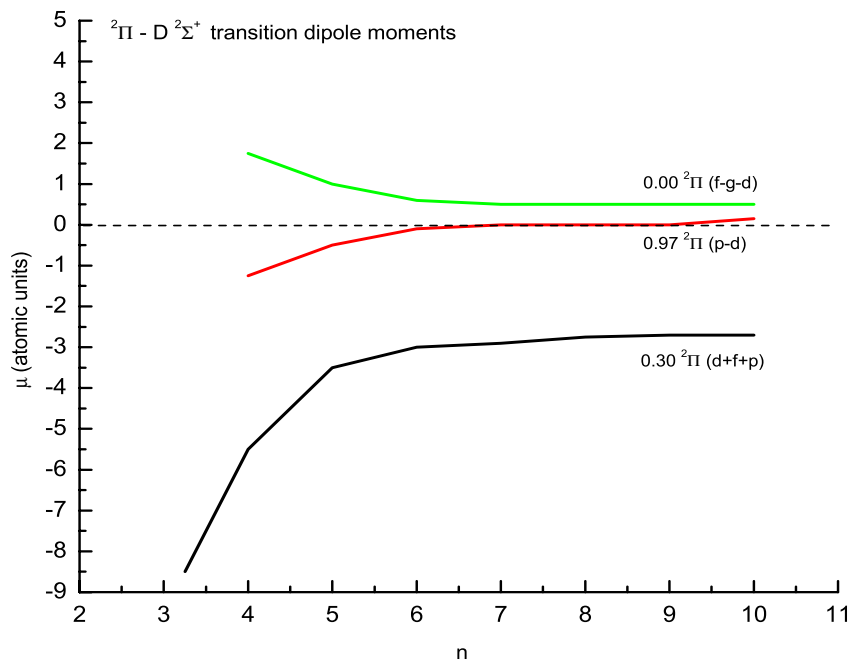
Figure 3-5: Transition dipole moments for $^2\Pi$ states calculated with R-matrix theory [4].

Where the amount of data was sufficient, least-squares fits of band origins to standard vibrational constants were attempted. The fitting procedure uses the standard Dunham type expression to determine the upper state zero-point energy (T_e) and vibrational constants $(\omega_e, \omega_e x_e)$:

$$T_{v'} = T_e + \omega'_e(v' + 1/2)\rho - \omega'_e x_e(v' + 1/2)^2\rho^2 + \dots \quad (3.1)$$

In this case ρ is the mass-dependent parameter $([\mu/\mu']^{1/2}$ for fitting data from two isotopomers, with $Ca^{35}Cl$ being the reference isotope $(\mu_{ref} = 18.64966)$ and $Ca^{37}Cl$ the "child" isotope $(\mu_{child} = 19.202940)$ [50].

Although the bandheads were, in most cases, fairly easy to measure from our spectra, the most accurate constants are obtained by finding the rotationless band origin, v_o. Herzberg offers the following formula to determine the difference between
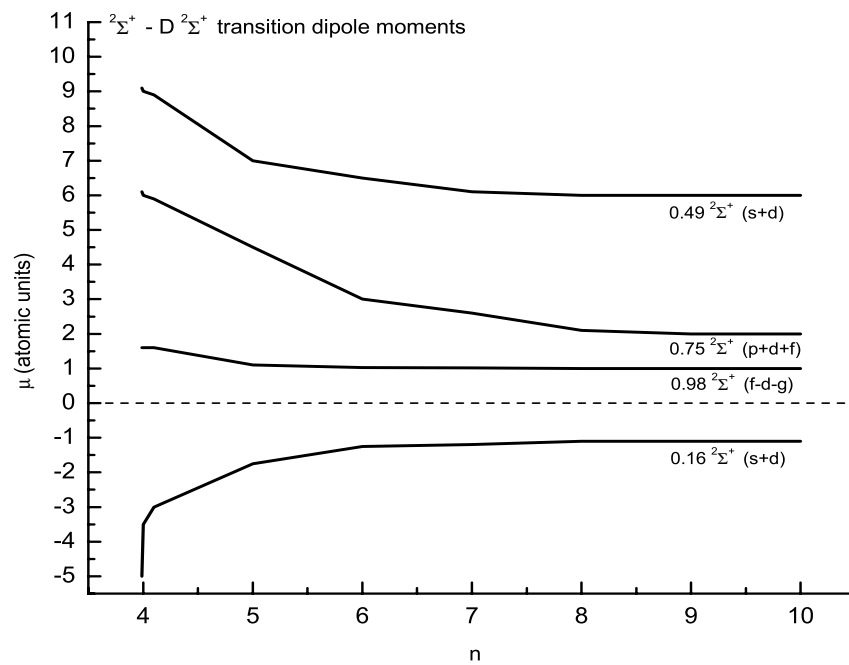
Figure 3-6: Transition dipole moments calculated with R-matrix theory. Transitions from the D (2.49 $^2\Sigma^+$) state to other n.49 Rydberg states have particularly large transition moments [4].

the bandhead and the band origin:

$$\nu_{bandhead} - \nu_{bandorigin} = -\frac{B_{v'} + B_{v''}}{4(B_{v'} - B_{v''})} \tag{3.2}$$

This equation requires information about the rotational constants for both the lower and upper states. While the lower state is quite well known, the molecular constants for the Rydberg states are less so. A previous analysis by this laboratory determined a value of $B_e = 0.164$ ($\pm$ 0.002) cm^{-1} for Ca^{35}Cl Rydberg states with n* ≥ 6.49 [22]. It was decided to use this value of B_e as the starting point for a band contour analysis using the SPECVIEW program [48]. Fig. 3-12 illustrates a typical SPECVIEW simulation of an intense feature in our survey spectra.

In this case, the n* $= 3.49$ band was found to have a very similar B_v value to the n* $= 6.49$ band (hardly distinguishable considering the 5% estimated error in a typical contour analysis). Eq. 3.2 is straightforward to apply after the B'_v value is determined, and yields $\nu_{bandhead} - \nu_{bandorigin} \approx 2.1$ cm^{-1}. A similar band contour analysis was performed on each fitted band listed in Tables 3.3.1, 3.3.1, and 3.3.1. When a determination of B_v was not possible, the value of 2.1 cm^{-1} as determined above was subtracted from the bandhead measurement to yield the band origin used in the fit.

The results of the least-squares analysis allow us to compare the ω_e values for the three n* $= 3$ core-penetrating $^2\Sigma^+$ series (see Table 3.7). The vibrational constants for these n* $= 3$ states differ by no more than 3%. Since vibrational and rotational constants are expected to stabilize beyond the "valence" range (n*$\geq$4, where the radius of the Rydberg orbit is large enough that the electron has minimal interaction with the ion core), another useful comparison can be made to the high-n* (CaCl$^+$) value of the vibrational constant for the 0.49 $^2\Sigma^+$ series provided by earlier studies at higher n* [22]. One can see from Fig. 3-7 that the value of the vibrational constant has reached 98% of its asymptotic value by n* $= 3.49$.

A more analytical approach can also be applied that explains the difference between the low-n* vibrational frequencies in terms of n*-scaling of the quantum defect
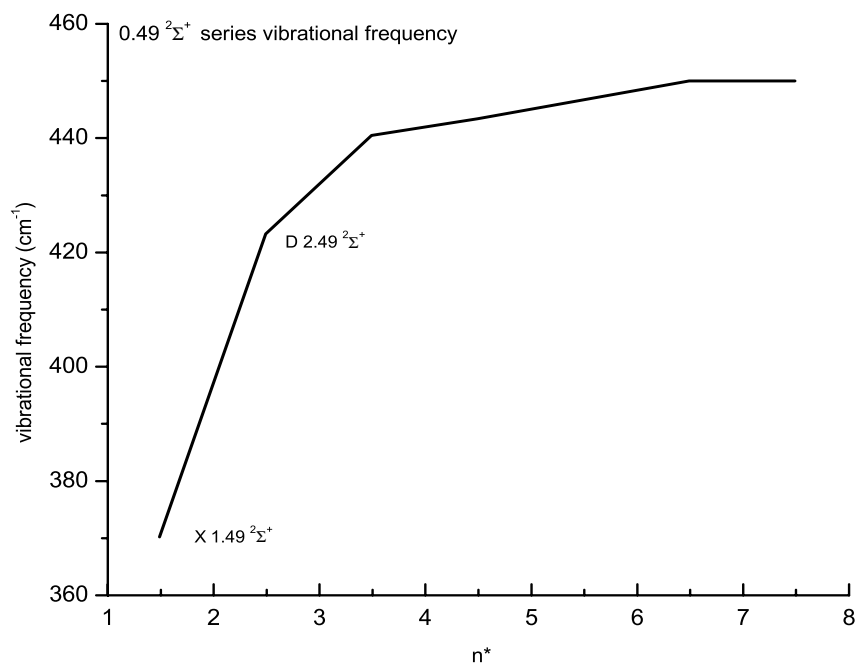
Figure 3-7: Vibrational frequencies of the 0.49 $^2\Sigma^+$ Rydberg series as a function of n*. The lowest-n* members show the largest deviation from the asymptotic CaCl$^+$ value of the vibrational frequency as expected from n*-scaling of the quantum defect derivative.

Table 3.2: Values of X $^2\Sigma^+$ state constants held fixed in least squares fitting of band origins [6].

Parameter	Value (cm^{-1})
ω_e	370.201
$\omega_e x_e$	1.3732
$\omega_e y_e$	9.3×10^{-3}
$\omega_e z_e$	-4.8×10^{-4}

Table 3.3: Assignment of observed vibrational band origins in the n* = 3.16 $^2\Sigma^+$ - X $^2\Sigma^+$ Transition from (1+1) REMPI spectra of CaCl. Band origins are reported in cm^{-1} with absolute uncertainty of $\pm$ 1 cm^{-1} (1-σ). The variance of the fit was 0.85.

		$Ca^{35}Cl$				$Ca^{37}Cl$	
v'	v''	Band origin v_0	Residual	v'	v''	Band origin v_0	Residual
0	0	37469.9	0.05	0	0	37468.3	-0.07
1	0	37915.4	0.31	1	0	37907.8	-0.30
2	0	38355.9	-0.95	2	0	38345.4	1.0
3	0	38795.3	1.02	3	0	38773.8	-1.1

derivative, $d\mu/dR$. Following the derivation first applied by Herzberg and Jungen [54] and refined by Jakubek *et al.* [20], we can express the potential curve for a Rydberg state as

$$U(R) = U^+(R) - \frac{\Re}{[n - \mu(R)]^2}, \tag{3.3}$$

where $U^+(R)$ is the potential curve of the molecular ion, $\Re$ is the Rydberg constant, n is the principal quantum number, and $\mu(R)$ is the quantum defect function, which is expected to be a slowly varying function of R. The lowest vibrational level of the potentials can be approximated by a harmonic oscillator expanded about R_e:

$$U(R) = U(R_e) + \frac{k}{2}(R - R_e)^2 + \dots \tag{3.4}$$

and

Table 3.4: Assignment of observed vibrational band origins in the n* = 3.49 $^2\Sigma^+$ - X $^2\Sigma^+$ Transition from (1+1) REMPI spectra of CaCl. Band origins are reported in cm^{-1} with absolute uncertainty of ± 1 cm^{-1} (1-σ). The variance of the fit was 0.93.

		Ca^{35}Cl				Ca^{37}Cl	
v'	v''	Band origin v_0	Residual	v'	v''	Band origin v_0	Residual
0	2	38832.4	0.41	0	2	38841.4	-0.63
1	3	38906.6	-1.05	0	1	39200.9	-0.74
0	1	39196.6	-0.18	1	2	39271.9	-1.56
1	2	39269.7	-0.05	0	0	39564.7	0.88
0	0	39564.8	0.45	1	1	39632.2	-0.87
1	1	39634.9	0.34	2	2	39700.7	-1.54
2	2	39704.3	0.54	3	3	39769.9	-1.46
3	3	39773.9	-1.00	1	0	39996.2	1.01
4	4	39842.9	-2.00	2	1	40061.7	-0.16
1	0	40002.7	0.59	4	3	40192.3	-0.44
2	1	40070.5	0.93	2	0	40425.4	1.37
4	3	40203.4	-1.10	3	1	40487.4	-0.62
2	0	40438.1	1.01	4	2	40552.0	0.12
3	1	40503.0	1.08	3	0	40852.2	2.03
4	2	40566.4	0.23	4	1	40912.9	1.48
5	3	40629.2	0.02	5	2	40971.8	-0.83
3	0	40871.0	1.65	5	1	41332.1	-0.16
4	1	40932.7	1.22	6	1	41750.8	0.43
5	2	40994.0	0.61				
6	3	41054.1	-1.22				
4	0	41298.4	-0.56				
5	1	41360.1	1.86				
6	2	41416.9	-0.64				
7	3	41476.2	-0.43				
8	4	41535.7	-0.04				
9	5	41595.2	0.56				
5	0	41726.0	0.28				
6	1	41782.3	-0.02				
7	2	41838.6	-0.25				
8	3	41895.1	-0.15				
9	4	41951.7	0.18				

Table 3.5: Assignment of observed vibrational band origins in the n* = 3.75 $^2\Sigma^+$ - X $^2\Sigma^+$ Transition from (1+1) REMPI spectra of CaCl. Band origins are reported in cm^{-1} with absolute uncertainty of ± 1 cm^{-1} (1-σ). The variance of the fit was 0.36.

		Ca^{35}Cl				Ca^{37}Cl	
v'	v''	Band origin v_0	Residual	v'	v''	Band origin v_0	Residual
0	1	40398.0	-0.94	0	0	40766.2	0.29
0	0	40767.0	0.65	1	0	41195.4	-0.02
2	0	41636.9	-0.01	3	0	42051.1	0.16
3	0	42070.1	-0.16				

Table 3.6: Results of least squares fits for $^2\Sigma^+$ - X $^2\Sigma^+$ band origins for three Rydberg series. (1-σ) error in parentheses.

State (n*)	T_e (cm^{-1})	ω_e (cm^{-1})	$\omega_e x_e$ (cm^{-1})
3.16	37429.0 (1.1)	450.5 (1.3)	2.2 (0.3)
3.49	39529.1 (0.4)	440.5 (0.2)	1.47 (0.02)
3.75	40732.8 (0.7)	437.1 (1.0)	0.61 (0.27)

$$U^+(R) = IP + \frac{k^+}{2}(R - R_e^+)^2 + \dots. \tag{3.5}$$

If we expand $\mu(R)$ in a Taylor series about $R = R_e$ and apply Eqs. 3.4 and 3.5, Eq. 3.3 can be rewritten as

$$U(R) = \frac{k^+}{2}(R - R_e^+)^2 + IP - \frac{\Re}{n^{*2}} - \frac{2\Re}{n^{*3}}\frac{d\mu}{dR}(R - R_e^+) - \frac{3\Re}{n^4}(\frac{d\mu}{dR})^2 - \frac{\Re}{n^3}\frac{d^2\mu}{dR^2}(R - R_e^+)^2. \tag{3.6}$$

By differentiating U(R) and equating the derivative to zero, we can find R$_{en*}$:

$$\frac{dU_{n*}}{dR} = 0 = [k^+ - \frac{6\Re}{n^{*4}}(\frac{d\mu}{dR})^2 - \frac{2\Re}{n^{*3}}\frac{d^2\mu}{dR^2}](R_{en*} - R_e^+) - \frac{2\Re}{n^{*3}}\frac{d\mu}{dR}, \tag{3.7}$$

and by differentiating this result we obtain k$_{n*}$, the force constant:

$$\frac{d^2U_{n*}}{dR^2} = k_{n*} = k^+ - \frac{6\Re}{n^{*4}}(\frac{d\mu}{dR})^2 - \frac{2\Re}{n^{*3}}\frac{d^2\mu}{dR^2}. \tag{3.8}$$

We can substitute k^+ by the following (and convert to spectroscopic units):

$$\tilde{k}^+ = k^+ \frac{10^{-16}}{hc} = \frac{4\pi^2 c 10^{-16}}{N_o h} \tilde{\omega_+}^2 \tilde{\mu} = 0.02966013 \cdot \tilde{\omega_{e+}}^2 \tilde{\mu} \tag{3.9}$$

where N_o is Avagadro's number, c is the speed of light in cm/s, h is Planck's constant in erg/s, $\tilde{\omega_{e+}}$ is the vibrational frequency of the ion in cm^{-1}, and $\tilde{\mu}$ is the molecular reduced mass in amu. The units of $\tilde{k}^+$ are then cm^{-1}/Å^2.

Rearranging Eq. 3.9, we have

$$(R - R_e^+) = \frac{\frac{2\Re}{n^{*3}} \frac{d\mu}{dR}}{\tilde{k}^+ - \frac{6\Re}{n^{*4}} \left(\frac{d\mu}{dR}\right)^2 - \frac{2\Re}{n^{*3}} \frac{d^2\mu}{dR^2}} \tag{3.10}$$

where we notice that the terms in n^{*3} and n^{*4} must be small when compared to $\tilde{k}^+$, giving

$$(R - R_e^+) = \frac{\frac{2\Re}{n^{*3}} \frac{d\mu}{dR}}{\tilde{k}^+} \tag{3.11}$$

Substituting for $\tilde{k}^+$ and rearranging, we have

$$(R - R_e^+) = \frac{2\Re}{0.02966013 \cdot \tilde{\omega_+}^2 \tilde{\mu}} \frac{1}{n^{*3}} \frac{d\mu}{dR} \tag{3.12}$$

Noting that for CaCl, $\tilde{\omega_+} = 450$ cm^{-1} and $\tilde{\mu} = 18.64960$, this can be simplified to

$$(R - R_e^+) = 1.959371 \cdot \frac{1}{n^{*3}} \frac{d\mu}{dR} \tag{3.13}$$

or in rearranged in terms of $\frac{d\mu}{dR}$,

$$\frac{d\mu}{dR} = 0.5103678 \cdot n^{*3} (R - R_e^+) \tag{3.14}$$

This equation can be used to calculate the quantum defect derivatives for a particular Rydberg series if its R_{en^*} is known (R_{en^+} is 2.3477 Å [22]). Table 3.8 shows calculated quantum defects for Rydberg series terminus states which have known values of R_{en^*}. One of the most interesting results from this calculation is the anomalously large value of $\frac{d\mu}{dR}$ for the C $^2\Pi$ state, which is also the case for the C state of CaF [15]. An

89

The chart shows data points with a fit curve. The y-axis is labeled $\omega_{en+} - \omega_{en*}$ and the x-axis is labeled n*. Annotation on the chart reads:

fit model: $(221.9287/n*^3)(d^2\mu/dR^2)$
$(d^2\mu/dR^2) = 1.88 +/- 0.09$ Angstrom^{-2}
$\chi^2_{red} = 2.0$
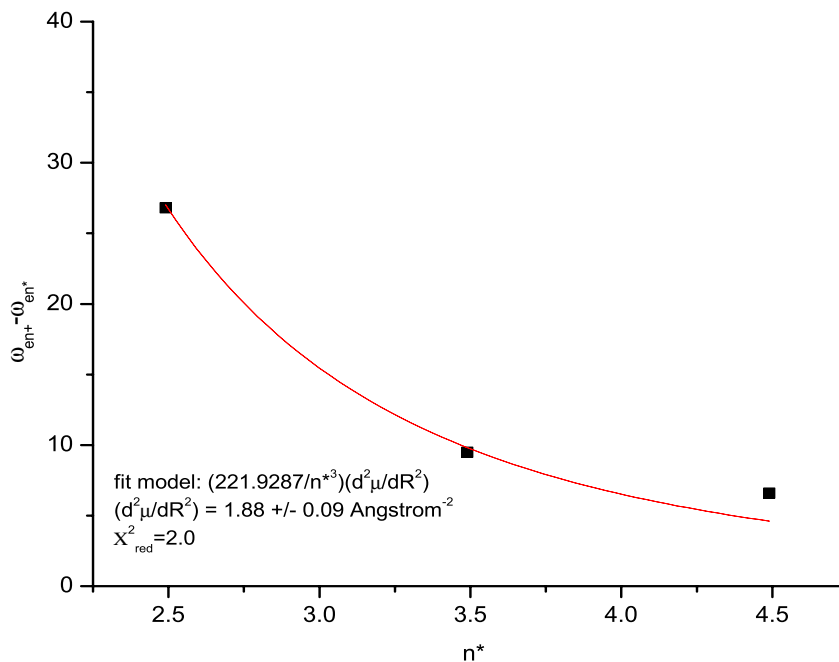
Figure 3-8: Differences of vibrational constants for observed members of the 0.49 $^2\Sigma^+$ Rydberg series and CaCl$^+$ as a function of n* and the second quantum defect derivative. The value for the X terminus state was ignored for this fit, as core-penetration effects reach a maximum at lowest-n*.

ab initio quantum chemistry study of CaF showed that not only is the C $^2\Pi$ state "reverse" polarized toward the F$^-$ ligand (as opposed to the A $^2\Pi$ state, which is stabilized by the "normal" backside polarization behind the Ca^{+2}), but that it also has significant F $2p\pi$ character, making it the least ionic bond in CaF [15, 55]. A similar analysis for CaCl would certainly yield the same conclusion, and explains the special nature of the C $^2\Pi$ state.

While the equation derived above relates the change in R$_e$ to n* and the quantum defect derivative, it would be more convenient for comparison of vibrational frequencies at different n* to develop a formulation that directly relates ω_{en*} and ω_{en+}. This can be done by combining Eqs. 3.9 and 3.10:

90

$$\tilde{\omega_e^+} - \tilde{\omega_{en^*}} = 1.862503 \times 10^6 \frac{1}{\tilde{\omega_{e+}}\tilde{\mu}} \left(\frac{3}{n^{*4}} \left(\frac{d\mu}{dR} \right)^2 + \frac{1}{n^{*3}} \frac{d^2\mu}{dR^2} \right).$$

<div align="right">(3.15)</div>

This result allows us to calculate the first and second quantum defect derivatives from measured values of $\tilde{\omega}_e$. The most extensive data set we have for the variation of $\tilde{\omega}_e$ with n* is for the 0.49 $^2\Sigma^+$ series as described above. A fit was carried out on the data shown in Fig. 3-7 and Table 3.7. The results from the fit are shown in Fig. 3-8. The most surprising result from this fitting procedure was a 7x improvement of χ^2_{red} by dropping the $1/n^{*3}$ term. The $1/n^{*3}$ term alone does a much better job of simulating the observed vibrational frequency differences. While we know of no *a priori* reason why this should be so, we decided to drop the $1/n^{*3}$ term. The determined value of the second quantum defect derivative for the 0.49 $^2\Sigma^+$ series is 1.88 ±0.09 $\mathring{A}^{-2}$.

The significance of determining values for the quantum defect derivatives comes from their power to predict other molecular properties such as autoionization rates and perturbation matrix elements [20,54]. It is not an overstatement to say that most of the dynamics in a Rydberg molecule are encapsulated by the quantum defect and its derivatives.

3.3.2 $^2\Pi$ states

With the remarkable observation of ninety-two band origins in nine electronic states, the three core-penetrating $^2\Sigma^+$ series clearly dominate the CaCl survey spectra from the X $^2\Sigma^+$ state. The paucity of observed $^2\Pi$ states is surprising. Since the transition dipole calculations for the two core-penetrating $^2\Pi$ series indicate a weaker (by a factor of ≈3 for μ^2 for the 0.30 $^2\Pi$ series and ≈30 for the 0.97 $^2\Pi$ series as compared to the 0.49 $^2\Sigma^+$ series) but certainly not forbidden transition moment (see Figs. 3-6 and 3-5), the most likely explanation for the absence of $^2\Pi$ states in our spectra is predissociation that prevents their detection by standard multi-photon ionization techniques.

While predissociation also occurs in the $^2\Sigma^+$ states, the repulsive predissociating state responsible has been determined to be $^2\Sigma^+$ (the $^2\Sigma^+ \sim ^2\Sigma^+$ electrostatic-based
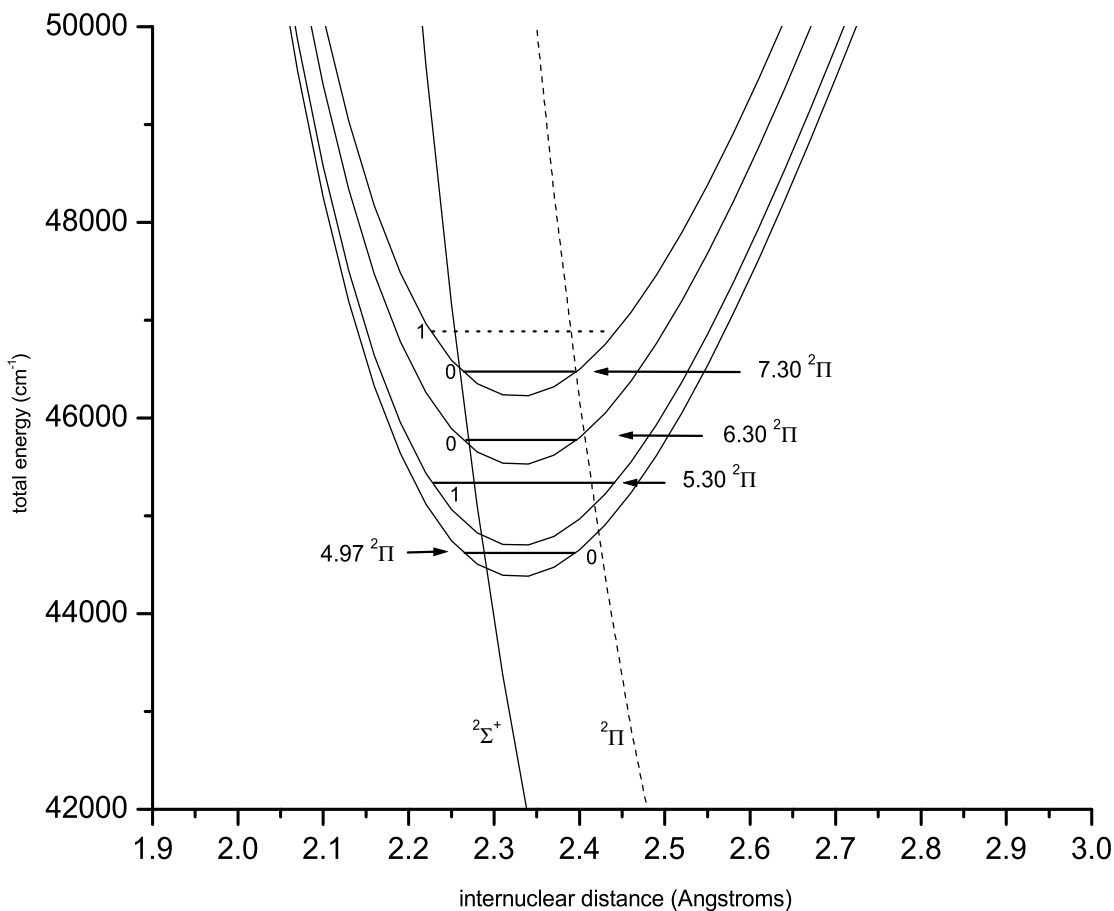
Figure 3-9: Potential energy curves for observed bound $^2\Pi$ Rydberg states and $^2\Pi$ and $^2\Sigma^+$ repulsive states. The $^2\Pi$ repulsive curve is expected to be steeper than $^2\Sigma^+$, and its intersection of the $^2\Pi$ Rydberg potential curves may never approach R_e^+, even as n*$\to$ ∞. The repulsive $^2\Sigma^+$ curve was determined by a linewidth analysis (see Chap. 5), while the $^2\Pi$ curve was constructed to be in qualitative agreement with the vibrational levels observed in our survey spectra.

predissociation mechanism is described in detail in Chap. 5). For Rydberg $^2\Pi$ states, there are a few possibilities for the predissociation mechanism. The first case would be a heterogeneous predissociation involving a J-dependent matrix element such as that caused by a gyroscopic interaction [56]. The selection rules for a gyroscopic perturbation are $\Delta\Omega \pm 1, \Delta\Lambda \pm 1$, $\Delta S = 0$, and $\Delta\Sigma = 0$ [56]. The only suitable candidate for this interaction is $^2\Sigma^+$. This J-dependent $^2\Pi \sim^2\Sigma^+$ interaction could conceivably cause a reduction in ionization quantum yield to the predissociation channel with increasing J [56], allowing only a handful of low-J lines, if any, to remain visible in our survey spectra. The resolution of these spectra, however, is not high enough to determine whether the rotational contour of the observed bands is formed by a handful of predissociation-broadened low-J lines or from a "normal" jet-cooled (J_{max} = 25) band profile. In any event, this type of heterogeneous interaction is typically smaller than the homogeneous ones (typically electrostatic or spin-orbit interactions), and would likely not account for the almost complete wipe-out of all of the $^2\Pi$ states in the n* = 3-7 region.

A more reasonable candidate for the Rydberg $^2\Pi$ state predissociation is the electrostatic interaction with the $^2\Pi$ repulsive state, which is expected to be more repulsive than the $^2\Sigma^+$ repulsive state because of the increased electron density pointed toward the Ca π^{-1} hole states (see Fig. 3-1 and 3-2). This $^2\Pi \sim^2\Pi$ interaction is governed by a two-electron matrix element in an analogous manner to the $^2\Sigma^+ \sim^2\Sigma^+$ interaction described in Chap. 5. While the survey spectra recorded in this experiment do not have sufficient resolution for a linewidth analysis of the type performed for the $^2\Sigma^+$ repulsive state, the presence of $^2\Pi$ states in our survey spectra can be used to qualitatively determine the position of the crossing point between the $^2\Pi$ repulsive state and the manifold of $^2\Pi$ Rydberg states. Since we observe the $v = 1$ level for the n* = 5.30 $^2\Pi$ state and $v = 0$ levels for n* = 6 and 7 of the 0.30 $^2\Pi$ series, this indicates the curve could be crossing into the Rydberg state manifold near the

outer turning point for the $v = 1$ level of the n* = 5.30 state (see Fig. 3-9) [1] As the repulsive state crosses through the manifold of higher-n* $^2\Pi$ states, it would be expected to dramatically reduce the ionization quantum yield for vibrational levels with significant wavefunction density near the crossing point R_c, which is consistent with the lack of observations involving $v > 0$ for n* > 5. This argument, however, does not explain the fact that we did not observe the $v = 0$ level of the 5.30 $^2\Pi$ state, which should be unaffected by the repulsive state if this explanation were correct. We also know that the 5.30 $^2\Pi$ $v = 1$ level itself is partially affected by the predissociation, since molecular features were reproduced in the Ca atomic channel see Section 3.3.3 and Fig. 3-15). Thus the qualitative arguments used here must be considered some-what speculative. Further high-resolution work must be carried out to completely characterize the $^2\Pi \sim ^2\Pi$ interaction.

Band contour simulations have been performed on the three distinct types of band contours assigned as $^2\Pi$ states in our survey spectra. The band contours of three $^2\Pi$-$X\,^2\Sigma^+$ vibrational bands are remarkably different (see Figs. 3-10, 3-11, and 3-12). The gross differences between these band contours can largely be explained by changes in the spin-orbit coupling constant A. The spin-orbit multiplet splitting of Rydberg states may originate from either the Rydberg electron or the ion core, but for CaCl, the ion-core is $^1\Sigma^+$ and contributes nothing toward spin-orbit. It can be shown that the spin-orbit contribution from the Rydberg orbital is proportional to $\langle r^{-3} \rangle$ [56]:

$$\langle r^{-3} \rangle = \frac{1}{n^{*-3}(l+1)(l+(1/2)l} \propto (n^*)^{-3}. \tag{3.17}$$

Therefore we would expect that states within the same Rydberg series will have A values $\propto (n^*)^{-3}$. Figure 3-13 shows the results of scaling the known values of A from the A (0.97 $^2\Pi$ series terminus) and C (0.30 $^2\Pi$ series terminus) states. From

---

[1]The $^2\Pi$ curve was constructed with the following one parameter model:

$$E(cm^{-1}) = \frac{C_{12}}{R^{12}} + D_e \tag{3.16}$$

where C_{12} has the units Å^{12} cm^{-1} and $D_e = 33\ 171$ cm^{-1} +/- 1048 cm^{-1} for CaCl [47]. The value of C_{12} used here is 4.75×10^{-8}. The resultant curve is shown in Fig. 3-9.

the calculation, we can see that a large change (roughly 11 cm^{-1}) in the value of A is expected from n*≈4 to n*≈6. The best simulation to the experimental data for the n* = 4.97 (2,0) state has $A = 9$ cm^{-1}, while the simulation for the n* = 6.30 (0,0) state has $A = 2$ cm^{-1}. One can see from Fig. 3-12 that the spin-orbit coupling has collapsed so much by n* = 6 that the band profile at this resolution looks very similar to that for a $^2\Sigma^+$ state. While not perfect, the spin-orbit scaling argument allows a qualitative understanding of the band contours.

While the spin-orbit scaling is a useful tool for identifying $^2\Pi$ states in our spectra, the lack of confirming isotope shifts for any of the states makes any vibrational assignment tentative. The fragmentary appearance of $^2\Pi$ states seems to indicate the occurrence of changes in the predissociation rate from the $^2\Pi \sim {}^2\Pi$ repulsive interaction. Full confirmation of $^2\Pi$-continuum induced predissociation of $^2\Pi$ states would necessarily require additional experiments, preferably by a high-resolution technique such as OODR (Optical-Optical Double Resonance).

3.3.3 Direct observation of predissociation

One of the goals of this survey spectrum project was to observe direct CaCl predissociation into the atomic Ca mass channel, which is simultaneously monitored in our TOF/MS apparatus. The results were largely disappointing since few features of molecular origin were reproducibly observed in the atomic Ca mass channel. Nevertheless, the fact that molecular features were present at all gives hope that additional experiments would be able to increase the reproducibility and the signal level for such transitions. Evidently, there is a subtle competition between excitation and ionization rates of dissociation-broadened transitions on the one hand, and reduction of the quantum yield from ionization owing to predissociation on the other hand.

Two examples of assigned molecular features that were observed in the Ca channel are shown in Figs. 3-14 and 3-15. The 5.30 $^2\Pi$ state evident in the atomic channel of the latter figure is considerably more intense than the 3.49 $^2\Sigma^+$ state. It should be noted, however, that while the Ca-atomic detected features were reproducible for the predissociated $^2\Sigma^+$ states, they were much less so for $^2\Pi$ states. In fact, the 5.30
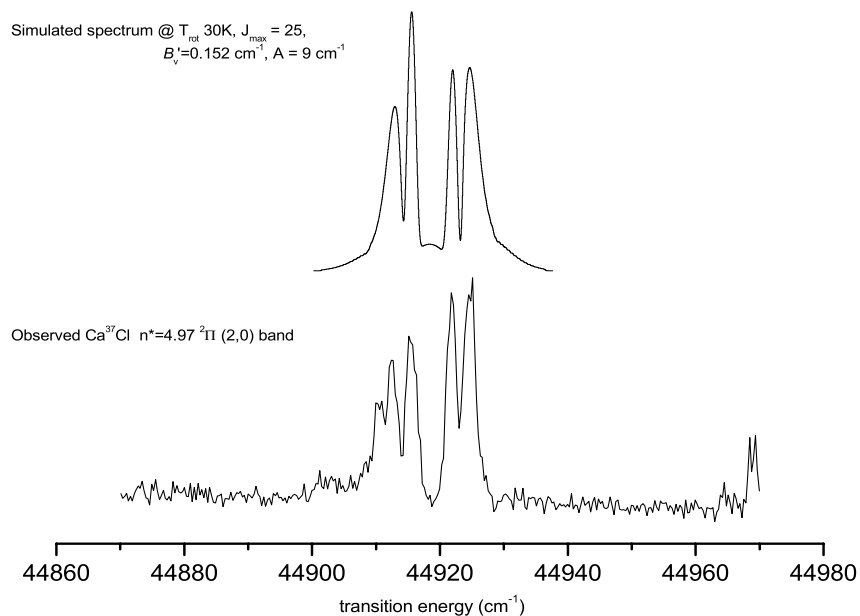
Figure 3-10: The $n^* = 4.97$ $^2\Pi$ - X $^2\Sigma^+$ (2,0) band for the $Ca^{37}Cl$ isotopomer, with simulated spectrum.

$^2\Pi$ state (1,0) band was only visible in the molecular mass channels under restrictive conditions; i.e., with the two-photon two-color (1+1') scheme (UV + 545 nm photons) rather than with the two-photon one-color (1+1) scheme (2 UV photons).

Other features were observed in the calcium channel that seemed to be of molecular origin, although they could not be assigned as CaCl vibrational bands. One particularly puzzling unassigned feature is shown in Fig. 3-16. The reproducible features seem to show degraded bandhead structure, although no reasonable n^* assignments could be made. As is seen in Fig. 3-16, there is no obvious correspondence between the atomic and molecular mass channels. While this could be expected in energy regions where the predissociation rate becomes large enough to completely obliterate features from a fluorescence or ionization based spectrum via a reduction in quantum yield, the low-n^* ($n^* \approx 3.85$) presence of such features prevents immediate assignment to vibrational bands of CaCl Rydberg series.
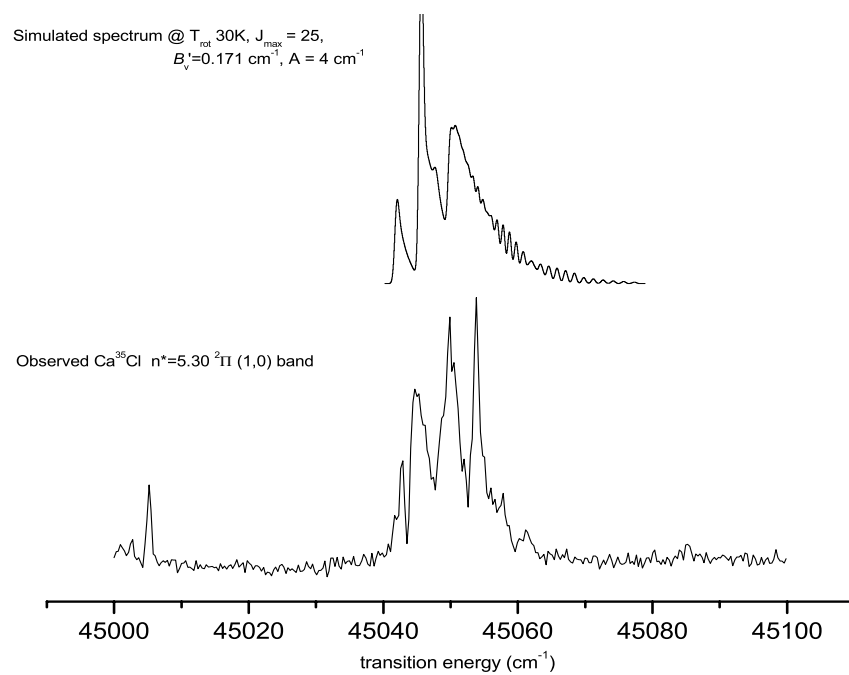
Figure 3-11: The n* = 5.30 $^2\Pi$ - X $^2\Sigma^+$ (1,0) band for the Ca^{35}Cl isotopomer, with simulated spectrum.

Simulated spectrum @ T_{rot} 25K, J_{max} = 25, B_v'=0.161 cm^{-1}, A = 2 cm^{-1}

Observed Ca^{35}Cl n*=6.30 $^2\Pi$ (0,0) band

transition energy (cm^{-1})
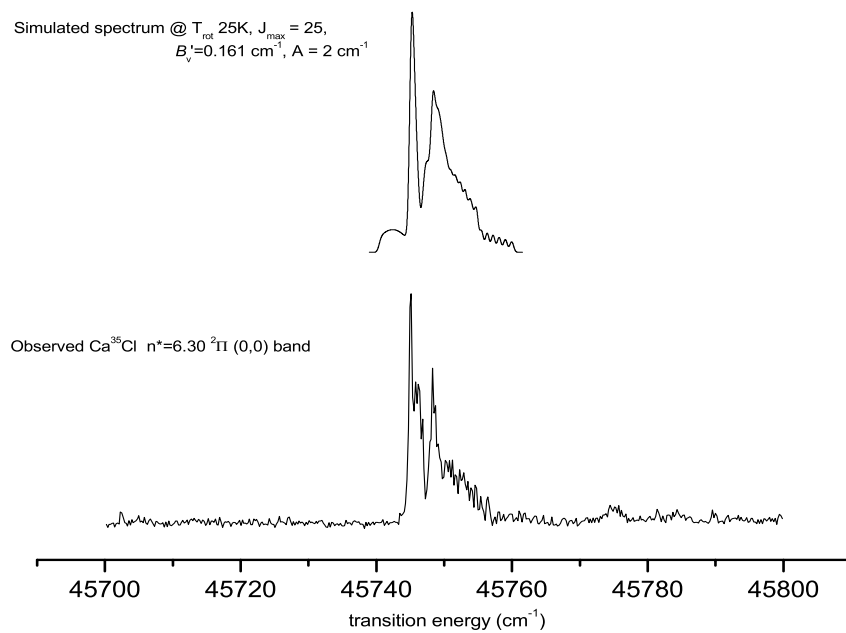
Figure 3-12: The n* = 6.30 $^2\Pi$ - X $^2\Sigma^+$ (0,0) band for the Ca^{35}Cl isotopomer, with simulated spectrum.
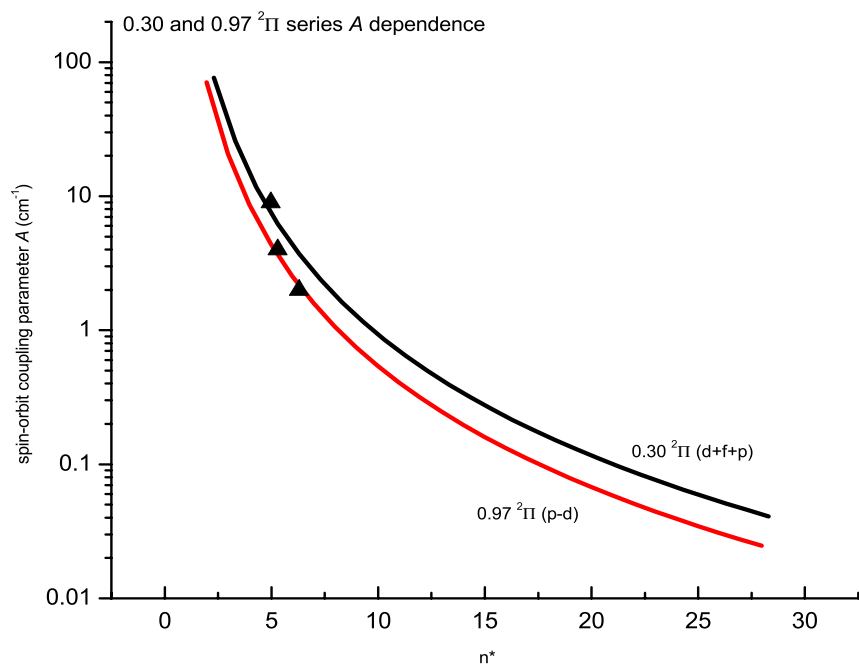
Figure 3-13: Evolution of the spin-orbit parameter A with n* as derived from n*$^{-3}$ scaling. The triangles represent values of A determined from the band contour analysis of the 4.97, 5.30 and 6.30 $^2\Pi$ states.

3.4 Conclusion

Over a period of several months, more than 10 000 cm^{-1} were scanned via two-color one-photon and two-color two-photon REMPI from the X $^2\Sigma^+$ ground state of CaCl. A number of vibrational bands belonging to known core-penetrating CaCl Rydberg series were observed and assigned based on their band contour, and where available, additional isotopomer data. Least-squares fits were performed on the vibrational band data for both isotopomers when the number of bands was sufficient. Comparisons of these fitted vibrational constants to known constants for the ground state of neutral CaCl and the ion CaCl$^+$ show the expected trend of low-n* states to the CaCl+ limit with increasing n* and allowed a determination of the quantum defect derivative, $(\mathrm{d}\mu/\mathrm{d}R)$.

Out of the 97 assigned vibrational bands from these data, only five were assigned to states of other than $^2\Sigma^+$ symmetry, and all of these five were assigned as $^2\Pi$ states. The $^2\Pi$ state transitions in the n* = 3-7 range, although allowed from electric dipole considerations, are predissociated by a $^2\Pi$ repulsive state which terminates on the same ground state separated atom limit as the CaCl X $^2\Sigma^+$ ground electronic state. The energy positions of the five observed $^2\Pi$ states allowed a qualitative determination of the position of the $^2\Pi$ repulsive state curve crossing. A full treatment of the $^2\Pi \sim ^2\Pi$ predissociation mechanism would require further experiments at higher resolution in the appropriate energy regions indicated by the survey spectra.
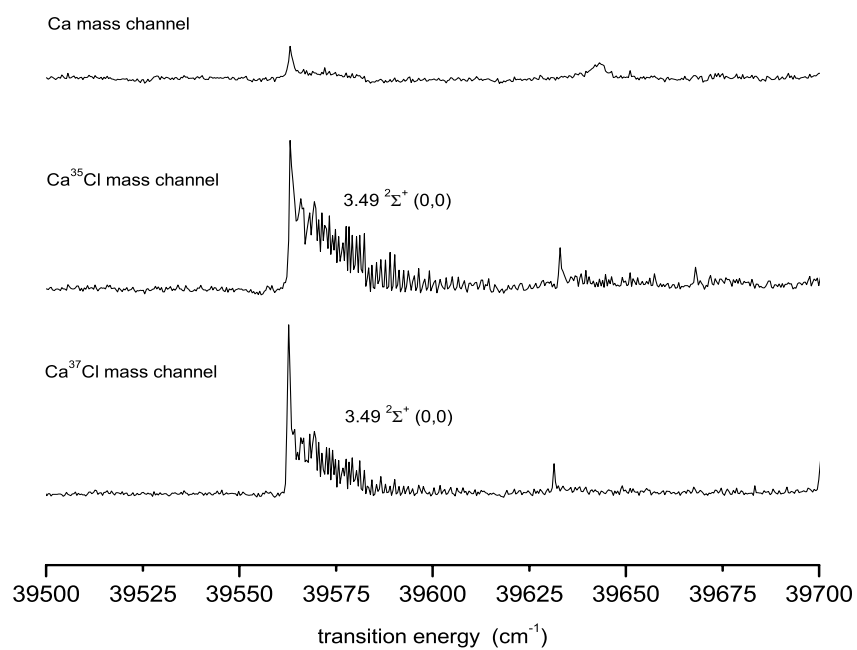
Figure 3-14: Spectrum showing calcium, $Ca^{35}Cl$, and $Ca^{37}Cl$ mass channels. A weak silhouette of some of the molecular features is evident in the calcium channel.

Ca mass channel

Ca^{35}Cl mass channel

5.30 $^2\Pi$ (1,0)

5.75 $^2\Sigma^+$ (0,0)

Ca^{37}Cl mass channel

45000   45050   45100   45150   45200

transition energy (cm^{-1})
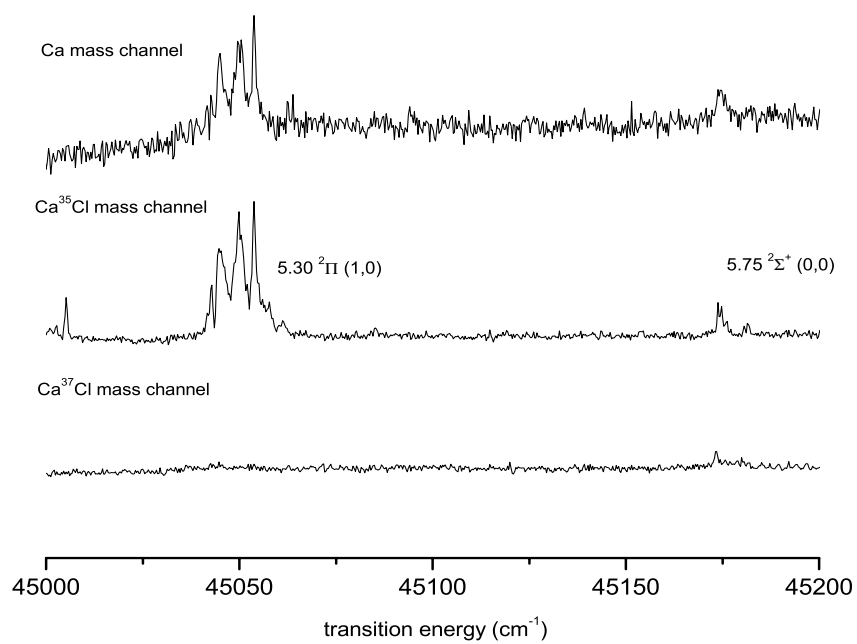
Figure 3-15: Spectrum showing calcium and Ca^{35}Cl mass channels. The molecular features are reproduced in the calcium atomic channel.
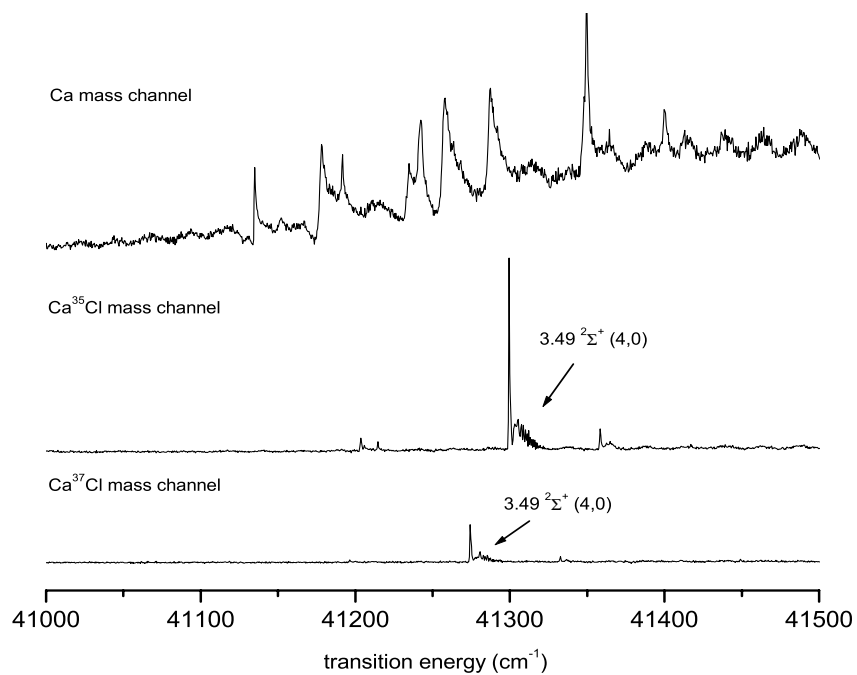
Figure 3-16: Spectrum showing calcium, $Ca^{35}Cl$, and $Ca^{37}Cl$ mass channels. The strong, reproducible features in the Ca channel, while molecular in appearance, could not be assigned to any known CaCl Rydberg series, and are not attributable to a one or two-photon transition in calcium atom.

Table 3.7: Comparison of ω_e values for selected $^2\Sigma^+$ Rydberg states.

Rydberg state	Value of ω_e and uncertainty (cm^{-1})	Highest assigned v' level	Reference
3.16 $^2\Sigma^+$	450.5 (1.3)	3	this work
3.75 $^2\Sigma^+$	437.1 (1.0)	3	this work
1.49 "X" $^2\Sigma^+$	370.201 (8)	9	[6]
2.49 "D" $^2\Sigma^+$	423.254 (7)	13	[6]
3.49 $^2\Sigma^+$	440.5 (.2)	9	this work
4.49 $^2\Sigma^+$	443.4 ($\Delta G_{1/2}$)	1	this work
6.49 $^2\Sigma^+$	450 (2.0)	3	[22]

Table 3.8: Core-penetrating CaCl Rydberg series with calculated quantum defect derivatives.

n* ($mod1$)	terminus state	n*$_{obs}$	ω_e (cm^{-1})	r$_e$ (Å)	$\frac{d\mu}{dR}$ (Å^{-1})	reference
0.49 $^2\Sigma^+$	X	1.509	370.2	2.439	0.160	[6]
0.75 $^2\Sigma^+$	B	1.869	367.2	2.4172	0.231	[51]
0.97 $^2\Pi$	A	1.849	373.2	2.4219	0.239	[52]
0.30 $^2\Pi$	C	2.285	336.9	2.5140	1.012	[53]

Table 3.9: Assignment of observed vibrational band origins for Rydberg electronic states in the $n^* = 4.5$-7.3 region from (1+1) REMPI spectra of CaCl. Band origins are reported in cm^{-1} with absolute uncertainty of $\pm$ 1 cm^{-1} (1-σ).

Ca^{35}Cl			Ca^{37}Cl		
v'	v''	Band origin v_0	v'	v''	Band origin v_0
$n^* = 4.49\ ^2\Sigma^+$					
0	2	42341.9	0	1	42709.2
0	1	42706.4	0	0	43068.8
0	0	43072.1	1	0	43058.2
1	0	43515.5			
$n^* = 4.75\ ^2\Sigma^+$					
0	0	43651.3	0	0	43651.1
$n^* = 4.97\ ^2\Pi$					
			0	0	44917
$n^* = 5.16\ ^2\Sigma^+$					
0	0	44390.0			
0	1	44022.7			
$n^* = 5.30\ ^2\Pi$					
1	0	45048			
1	1	44681			
$n^* = 5.75\ ^2\Sigma^+$					
0	0	45173.6	0	0	45172.8
$n^* = 5.97\ ^2\Pi$					
0	0	45398.7			
$n^* = 6.30\ ^2\Pi$					
0	0	45745.0			
$n^* = 6.49\ ^2\Sigma^+$					
0	1	45118.2	0	1	45522.8
0	0	45885.5	0	0	45884.8
1	0	46335.5	1	0	46328.5
$n^* = 6.75\ ^2\Sigma^+$					
0	0	46093.8	0	0	46093.8
$n^* = 7.30\ ^2\Pi$					
0	0	46444.9			

Chapter 4

Optical-Optical Double Resonance (OODR) in the n* = 5-7 region

4.1 Introduction

Previous studies of CaCl and CaF using Optical-Optical Double Resonance (OODR) techniques have allowed access to all six of the core-penetrating Rydberg series in CaF, while only a subset (four of six) were observed in CaCl [11, 13, 16, 22]. As was discussed in the previous chapter, the observation of Rydberg series in CaCl in the n* = 3 - 7 region is complicated by the presence of repulsive states which predissociate bound Rydberg states in this region. With the single-resonance survey spectra and the OODR experiments in the n* = 6 - 8 region by Li *et al.* serving as guides, further OODR experiments were attempted in this extensively predissociated region.

4.2 Experimental Details

For these experiments, a (1+1'+1') ionization scheme was chosen to access Rydberg states from the $D\ ^2\Sigma^+$ state (see Fig. 4-1). The D state was chosen for several reasons: (1) easily modelled $^2\Sigma^+$ rotational structure; (2) energy location at $\approx 75\%$ of the first IP, which greatly facilitates (1+1) ionization; (3) member of the 0.49 $^2\Sigma^+$ Rydberg series with nominal $(s+d)$ atomic character, which should allow access
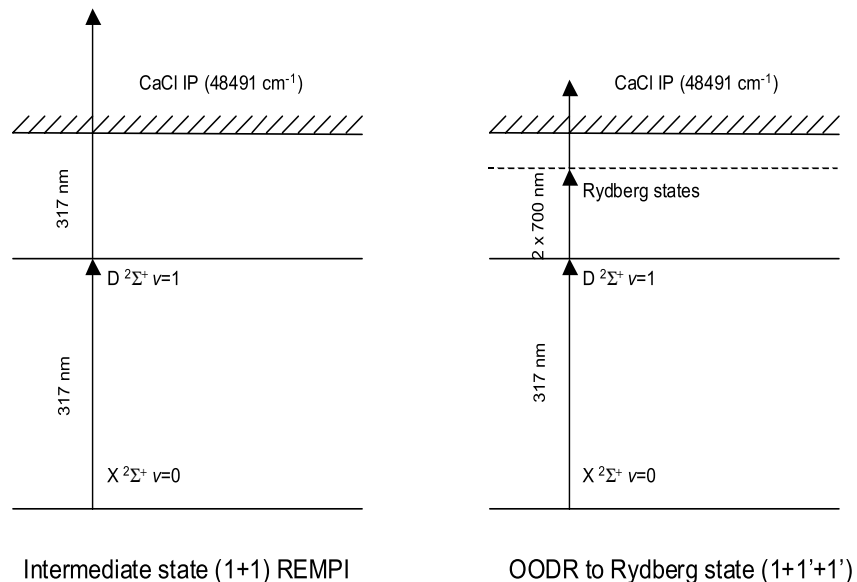
Figure 4-1: Energy level diagram for the D $^2\Sigma^+$ - X $^2\Sigma^+$ (1,0) transition of CaCl and OODR pump-probe scheme for reaching Rydberg state levels.

to other $^2\Sigma^+$ states and $^2\Pi$ Rydberg series.

A spectrum of the intermediate state itself was obtained through a (1+1) ionization scheme identical to that described in Section 2.3.3. In the first step, a level of the D $^2\Sigma^+$ state is excited by a single UV-photon. If the UV-laser flux is high enough, a second photon is simultaneously absorbed, pushing the total energy well above the first ionization limit (see Fig. 2-17). Typical UV pulse energies for acquiring an intermediate state spectrum were $\approx$600 - 1000 μJ/pulse with a collimated beam of $\approx$1 cm diameter. It should be noted that too much UV power can cause power broadening of the D-X lines and should be avoided. A careful balance of UV laser power and beam diameter must be made to allow optimum intermediate state signal acquisition. The UV-wavelength laser light necessary for excitation of the D state was generated in a frequency doubling unit equipped with BBO crystals in a Scanmate 2E dye laser using DCM dye. The $D - X$ transition, which had been previously measured, has an

n*=6.49 $^2\Sigma^+$ v=0
from D R(13)
without delay line

n*=6.49 $^2\Sigma^+$ v=0
from D R(13)
with delay line

45905   45910   45915   45920   45925   45930   45935

term value (cm^{-1})
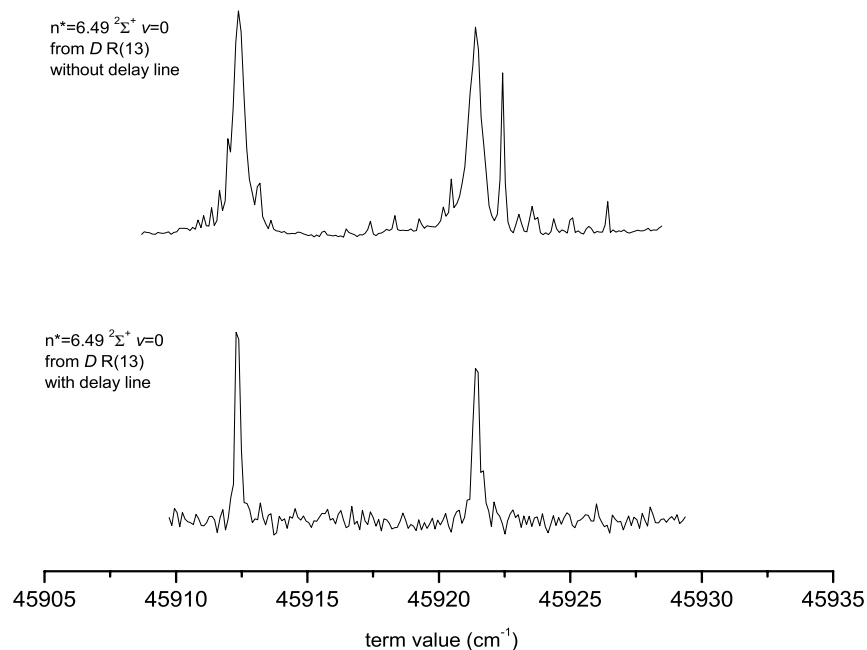
Figure 4-2: OODR spectra showing the need for an optical delay line to eliminate unwanted multiphoton peaks. The lower trace, acquired after the introduction of a 18 ns probe pulse delay line, shows the expected $P - R$ doublet.

extensive R-branch which allows selection of individual N, J components (as shown Fig. 4-4) for subsequent OODR pumping steps.

Once a suitable D-state N via the $D - X$ R branch had been selected, a second laser was overlapped with the UV beam, whose power had been considerably weakened (to <100 μJ/pulse) to inhibit ionization by direct absorption of two UV photons. The wavelength of the second laser was subsequently scanned in the visible and near-IR range from $\approx$550 - 720 nm. Typical pulse energy for the visible pump laser was $\approx$200 - 300 μJ/pulse, and the beam was expanded to the same diameter as the UV pump beam ($\approx$1 cm).

Initial experiments indicated that the probe pulse laser flux was high enough to cause undesired multiphoton transitions in the OODR spectra (see Fig. 4-2). The top trace in the figure shows the expected P and R branch pattern for transitions

terminating in the n* = 6.49 $^2\Sigma^+$ $v = 0$ state with a number of additional peaks in the wings of the lines. No assignments of these "trash" peaks could be made, and experimental parameters were changed to minimize their intensity. The only method which completely eliminated these additional peaks was the introduction of an optical delay of the probe pulse relative to the UV pump pulse which selects the intermediate state N level. Since both dye lasers are pumped by the same Nd:YAG pump laser, the most straightforward method to delay one pulse relative to the other is by forcing the light to make additional mirror passes before being introduced to the molecular beam chamber. In this case the probe beam was multipassed ≈1.5 table-lengths, or 18 ft. Since the speed of light in air is 0.98 ft/ns, the two pulses were separated by a little less than 18 ns, which is ∼ 3x the duration of the earlier laser pulse.

The Time-of-Flight/Mass Spectrometer operating voltages were largely in line with those specified in Table 2.3. The pulsed extraction electric field was not used in these experiments; a constant differential of (≈100 V/cm) between A1 and A2 existed during the laser excitation pulse. The DC electric field is not expected to cause significant changes in the level positions, widths, or lifetimes for states with the relatively low n* values discussed here.

An I_2 fluorescence excitation spectrum was simultaneously captured with the TOF/MS signal, allowing probe laser calibration through visible and near-IR region. The D $^2\Sigma^+$ - X $^2\Sigma^+$ transitions are well known [6].

Franck-Condon Factors were calculated for Rydberg (CaCl$^+$)-D $^2\Sigma^+$ transitions (see Fig. 4-3). The constants used for the Rydberg state are those suggested by previous OODR studies in the n* = 6-7 region [22]. The FCF's have a very diagonal propensity which strongly favors $\Delta v = 0$ transitions.
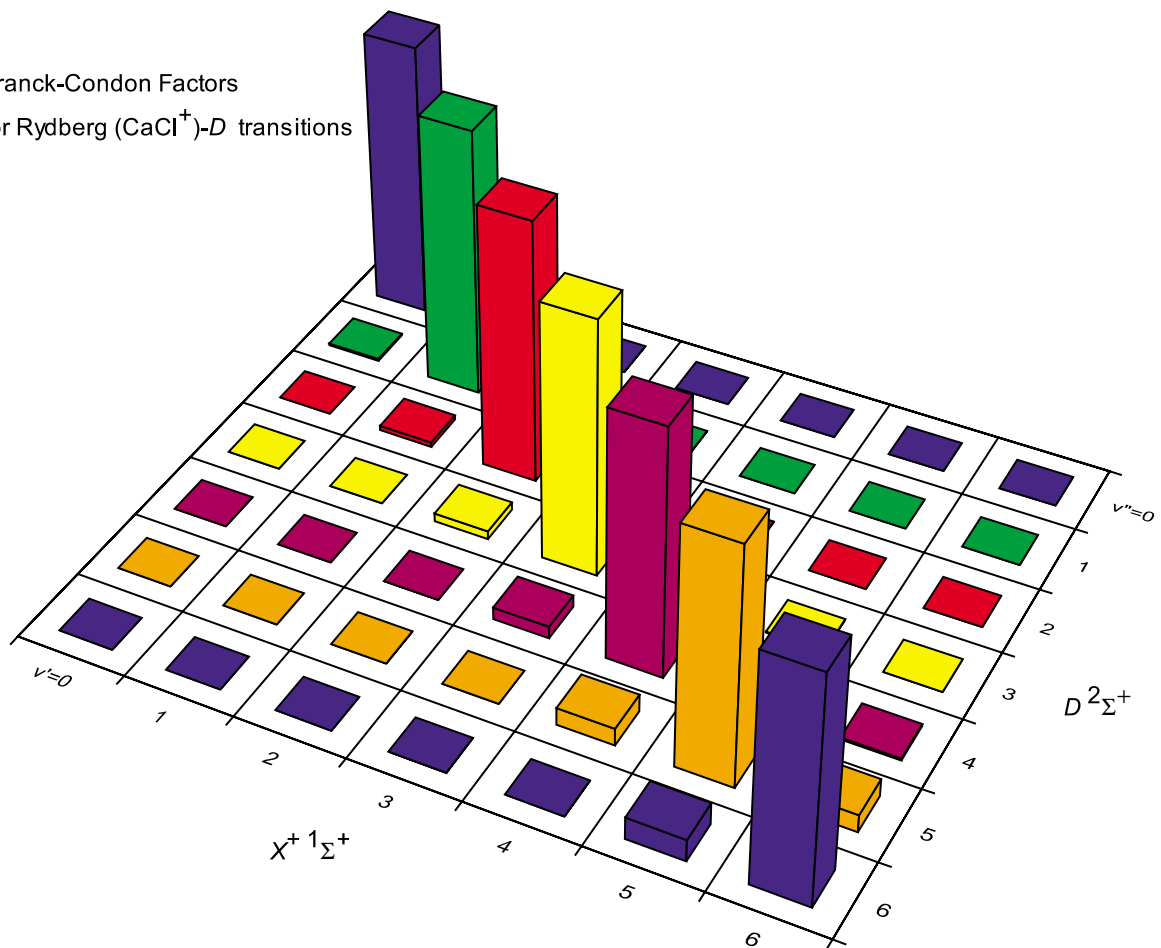
Figure 4-3: Franck-Condon Factors for the Rydberg (CaCl$^+$) - D $^2\Sigma^+$ transition in CaCl exhibit a strong $\Delta v = 0$ propensity. The matrix of FCFs is almost perfectly symmetric, so unseen FCFs can be estimated from foreground values.

4.3 Results and Discussion

4.3.1 Methodology

The most important aspect of OODR experiments is the dramatic reduction in the number of states accessible from a laser-selected intermediate state rovibrational level. From a singly selected N, J level of the D state, we expect to see a recognizable pattern of lines for transitions to various Λ electronic states based on known rules for electronic transitions. For example, from Fig. 4-4 we see that a $^2\Sigma^+$ -$^2\Sigma^+$ transition would manifest itself in a double-resonance spectrum as a two-line pattern corresponding to P and R branches. Similarly, a $^2\Pi$-$^2\Sigma^+$ transition could have as many as six branches for a case (a) $^2\Pi$ state (see Fig. 4-5) or five for a case (b) $^2\Pi$ state (see Fig. 4-6). Transition to states of higher Λ have a similar structure to those for $^2\Pi$ states, but they are forbidden by the $\Delta\Lambda = 0, \pm 1$ selection rule.

In theory, an OODR spectrum should be easily assigned based on the known selection of intermediate state pumping level and the expected pattern formation. In practice, however, a number of OODR scans through a particular energy region are necessary to confirm the presence and character of the excited state. Considerable use is made of the lower-state combination difference technique. This method is effective because branches pumped from different selections of intermediate state J (or in case (b), N) can terminate on the same upper state level (see Fig. 4-8). Our group has developed a method of using "stacked plots" to graphically identify and assign those levels that are reached from different intermediate state rotational levels [14, 16]. An example of such a plot is shown in Fig. 4-12. It is prepared in the following manner: (1) probe laser scans are calibrated via I_2 or similar reference standard; (2) known intermediate state transition energy is added; (3) the appropriate ground state rotational energy is added to reference all energies to the $v = 0$, $N = 0$ level of the $X\ ^2\Sigma^+$ ground state.
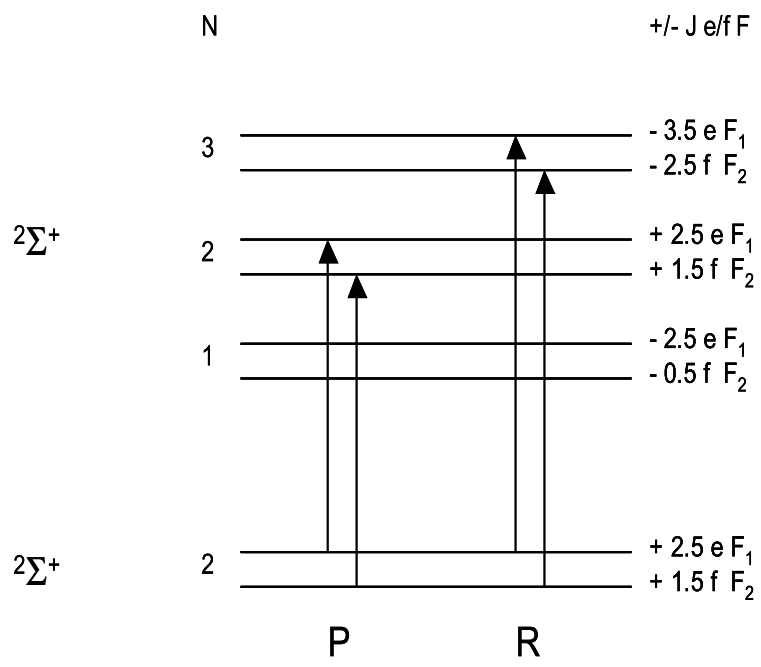
Figure 4-4: Transition level diagram showing rotational branch structure for $^2\Sigma^+$ - $^2\Sigma^+$ transitions. The $J = N+0.5/N\text{-}0.5$ splitting is exaggerated.

$^2\Pi$ (a) $- {}^2\Sigma^+$
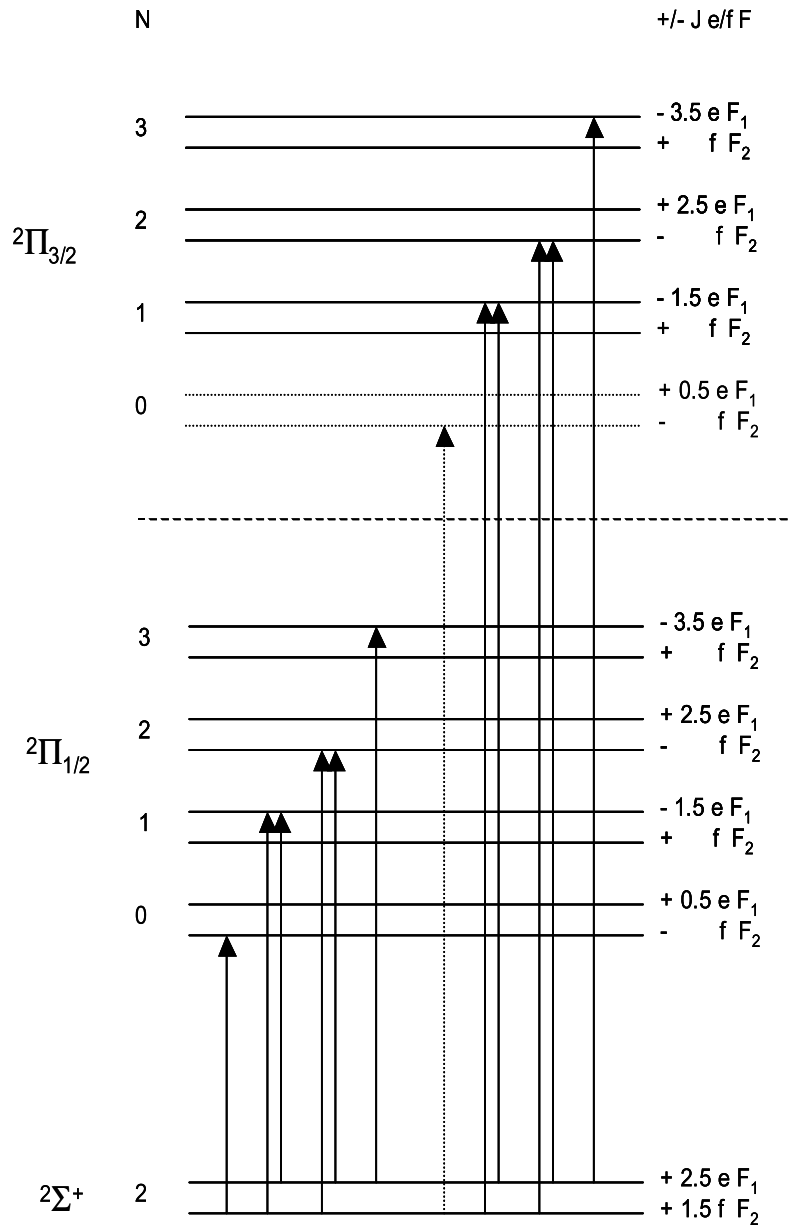
Figure 4-5: Transition level diagram showing rotational branch structure for $^2\Pi$ (a)-$^2\Sigma^+$ transitions. In case (a) the two $^2\Pi$ components are split by the spin-orbit coupling constant, A. Note that the $J=0.5$ level does not exist for the upper spin-orbit component.

114

$^2\Pi$ (b) - $^2\Sigma^+$

$^2\Lambda^+$ $^2\Lambda^-$

N   +/- J e/f F

+ 6.5 e F_1
+ 5.5 f F_2

6

− 6.5 f F_1
− 5.5 e F_2

− 5.5 e F_1

5   − 4.5 f F_2

+ 5.5 f F_1
+ 4.5 e F_2

+ 4.5 e F_1
+ 3.5 f F_2

4

− 4.5 f F_1
− 3.5 e F_2

− 3.5 e F_1

3   − 2.5 f F_2

+ 3.5 f F_1
+ 2.5 e F_2

+ 2.5 e F_1
+ 1.5 f F_2

2

− 2.5 f F_1
− 1.5 e F_2

$^2\Sigma^+$ N=4

+ 4.5 e F_1
+ 3.5 f F_2

S   R   Q   P   O
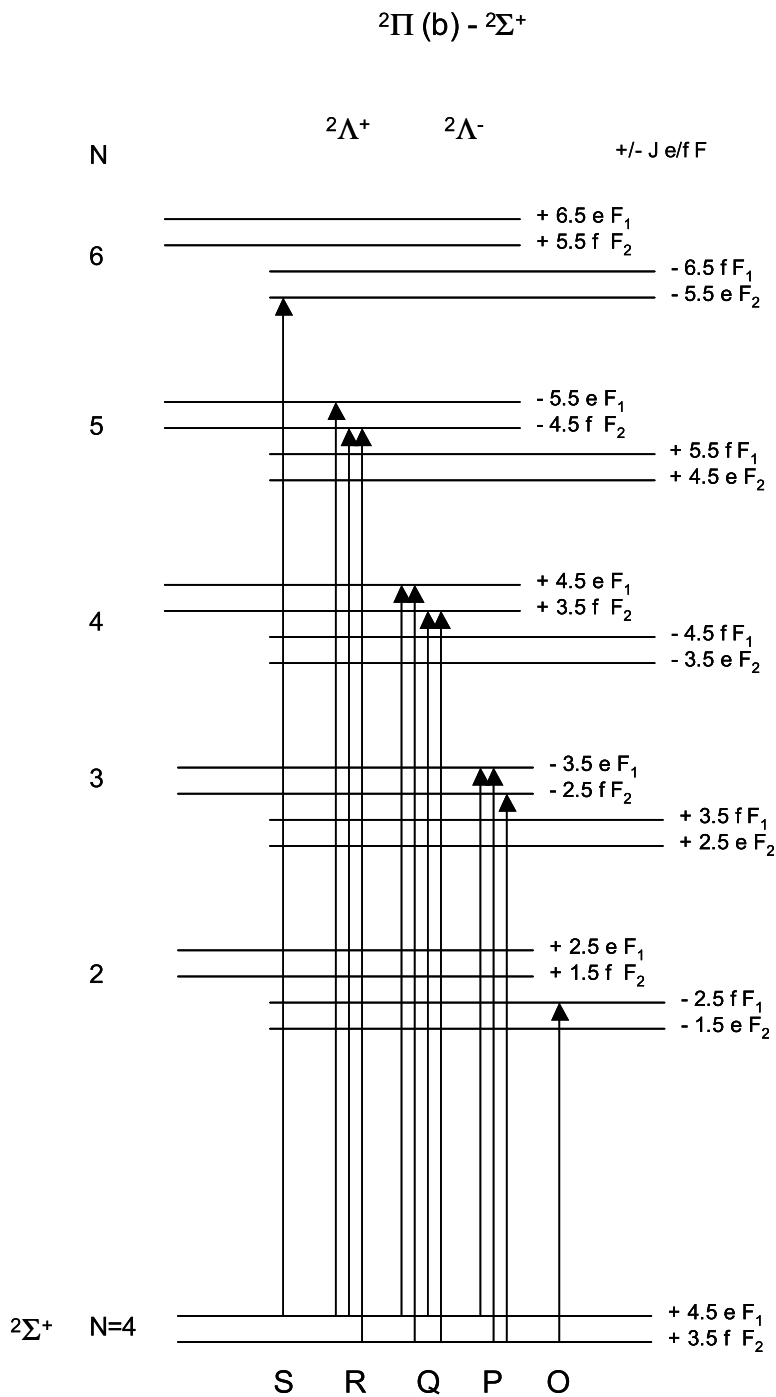
Figure 4-6: Transition level diagram showing rotational branch structure for $^2\Pi$ (b)-$^2\Sigma^+$ transitions. In case (b) $(A < 2BJ)$, the spin-orbit coupling constant, A, is small relative to $2BJ$, so the level structure is greatly collapsed from case (a). Rydberg $^2\Pi$states rapidly approach case (b) for n* > 3, although they will undergo l-uncoupling to case (d) as n* → ∞.

115

4.3.2   Rotational Hamiltonian

The rotational Hamiltonian is given by Hougen as [57]

$$\mathbf{H}^{rot} = \frac{\hbar}{2\mu r^2} \mathbf{R}^2, \tag{4.1}$$

where $\mathbf{R}$ is the pure rotational angular momentum, which by definition is perpendicular to the molecular axis. The total angular momentum $\mathbf{J}$ can be expressed as a vector sum of the rotational, electron-orbital, and electron-spin angular momenta in the molecule,

$$\mathbf{J} = \mathbf{R} + \mathbf{L} + \mathbf{S}. \tag{4.2}$$

which can be easily rearranged to give an expression for $\mathbf{R}$.

Further development of the Hamiltonian requires consideration of the appropriate basis set. For a diatomic molecule, this is determined by the Hund's case for the states involved [56]. Appropriate Hund's cases for Rydberg states with are typically (a), (b), and (d). The criterion for application of a particular Hund's case to a particular state is usually straightforward. $^2\Sigma^+$ states, having $\Lambda = 0$, are either Hund's case (b), or as N,n* $\to \infty$, case (d). In the case of $\Lambda \neq 0$, Hund's case (b) is valid in the limit that $A\Lambda << BJ$. By using the scaling relationships for the spin-orbit parameter, A, noted in section 3.3.2, we can determine a maximum predicted value of A for the n* = 8.30 $^2\Pi$ $v = 0$ state of 1.6 cm^{-1}. A typical value of B for a CaCl Rydberg state is 0.16 cm^{-1}, which corresponds to Hund's case (b) validity for this n* = 8.30 $^2\Pi$ state when $J >> 10$. At low enough n*, spin-orbit coupling effects cannot be ignored, and Hund's case (a) is necessary.

Rydberg states often show crossover behavior from the case (b) to the case (d) limit. This transition occurs when the separation between rotational energy levels becomes large relative to the separation between electronic states having the same l parentage and $\Delta\lambda = \pm 1$ [15, 56]. Since the core-penetrating series of CaCl and CaF are strongly $s \sim p \sim d \sim f$ mixed, Hund's case (d) will begin to apply when the rotational term BJ is large relative to the energy difference of states with $\Delta\lambda = \pm 1$

[15]. For example, the closest neighbor to the n* $= 8.30$ $^2\Pi$ $v = 0$ state mentioned above is the n* $= 8.16$ $^2\Sigma^+$ $v = 0$ state. If we calculate the energy difference between the two states using the Rydberg formula

$$\Delta E = \Re[\frac{1}{8.15^2} - \frac{1}{8.30^2}] = 59.2 \text{ cm}^{-1}, \tag{4.3}$$

and apply the Hund's case (d) criterion $\Delta E << BJ$, then we have a range for which case (b) applies for the n* $= 8.30$ $^2\Pi$ $v = 0$ state of $10.5 << J << 369.5$. Since the accessible J levels in our low-n* experiments range from $2.5 < J < 16.5$, we are much more likely to observe case (a) $\rightarrow$ case (b) crossover behavior than case (b) $\rightarrow$ case (d). We will therefore use the case (b) Hamiltonian as our basis.

Since electron-spin is decoupled from the electron orbital angular momentum, we can simplify Eq. 4.2 by defining a vector $\mathbf{N}$ such that $\mathbf{N} = \mathbf{J} - \mathbf{S}$. The effective rotational Hamiltonian depends on $\mathbf{R}^2$ [57]:

$$\mathbf{R}^2 = (\mathbf{N} - \mathbf{L})^2 = \mathbf{N}^2 + \mathbf{L}^2 - 2\mathbf{N} \cdot \mathbf{L}, \tag{4.4}$$

which can be expressed in terms of raising and lowering operators as

$$\mathbf{N} \cdot \mathbf{L} = \mathbf{N}_z\mathbf{L}_z + \frac{1}{2}(\mathbf{N}^+\mathbf{L}^+\mathbf{N}^-\mathbf{L}^+). \tag{4.5}$$

.

Substituting the last two equations into Eq. 4.1, we find:

$$\mathbf{H}^{rot} = B(r)[\mathbf{N}^2 + \mathbf{L}^2 - 2\mathbf{N}_z\mathbf{L}_z - \mathbf{N}^+\mathbf{L}^+ - \mathbf{N}^-\mathbf{L}^+], \tag{4.6}$$

where $B(r)$ is a function of the internuclear distance but has a dependence on the reduced mass (μ) of the molecule (effectively the rotational operator averaged over r for a particular electronic-vibrational state). We can express $B(r)$ in spectroscopic units (cm^{-1})

$$B(r) = \frac{h}{800\pi^2 c\mu} \cdot \frac{1}{r^2} \tag{4.7}$$

which has the value $16.857630/(\mu r^2)$ amu Å^2 cm^{-1} [14].

Since CaCl and CaF are effectively one-electron systems, the electronic orbital angular momentum in the molecule is effectively that of the Rydberg electron, l. This allows us to restate Eq. :

$$\mathbf{H}^{rot} = B(r)[\mathbf{N}^2 + \mathbf{l}^2 - 2\mathbf{N}_z\mathbf{l}_z - \mathbf{N}^+\mathbf{l}^+ - \mathbf{N}^-\mathbf{l}^+], \qquad (4.8)$$

which is the well known Hund's case (b) rotational Hamiltonian [56, 57].

The use of symmetrized basis functions allows the separation of the case (b) Hamiltonian into blocks of (+) and (-) Kronig symmetry. Kronig symmetry arises from the transformation properties of the electronic wavefunction upon reflection through the molecular plane. This property is especially useful since the case (b) Hamiltonian does not couple basis states which belong to opposite Kronig symmetries [15].

The symmetrized case (b) basis functions themselves are defined for $\Lambda = 0$ as [14, 57]:

$$|l0JN0\rangle, \qquad (4.9)$$

and for $\Lambda > 0$ as

$$|l\Lambda JN\Lambda\pm\rangle = 2^{-1/2}(|l\Lambda JN\Lambda\rangle \pm |l - \Lambda JN - \Lambda\rangle). \qquad (4.10)$$

The diagonal matrix elements take the form

$$\langle l\Lambda JN\Lambda\,|\mathbf{H}|\,l\Lambda JN\Lambda\rangle = B(r)[N(N+1) + l(l+1) - 2\Lambda^2], \qquad (4.11)$$

while the off-diagonal matrix elements are

$$\langle \Lambda JN\Lambda\,|\mathbf{H}|\,l\Lambda{+}1JN\Lambda{+}1\rangle = B(r)\sqrt{\frac{2}{2-\delta_{\Lambda 0}}}\sqrt{N(N+1) - \Lambda(\Lambda+1)}\sqrt{l(l+1) - \Lambda(\Lambda+1)}$$
$$(4.12)$$

If n* or J is low enough, the contribution from spin-orbit interaction to the Hamiltonian cannot be neglected. Kovács [58] gives the diagonal and off-diagonal elements of H^{so} in the case (b) basis. For the diagonal elements in Λ ($\Delta\Lambda = 0$) [14, 58]:

$$\langle l\Lambda JN\Lambda |\mathbf{H}| l\Lambda JN\Lambda\rangle = A\Lambda^2 \frac{J(J+1) - N(N+1) - S(S+1)}{2N(N+1)},$$
(4.13)

and for $\Delta\Lambda = 0, \Delta N = \pm 1$:

$$\langle l\Lambda JN\Lambda |\mathbf{H}| l\Lambda JN + 1\Lambda\rangle = A\Lambda$$
$$\times \frac{\sqrt{[(N+1)^2 - \Lambda^2][(J+N+1)(J+N+2) - S(S+1)][S(S+1) - (J-N)(J-N-1)]}}{2(N+1)\sqrt{(2N+1)(2N+3)}}$$
(4.14)

The off-diagonal elements are slightly more complicated (for $\Delta\Lambda = 1, \Delta N = 0$):

$$\langle l\Lambda JN\Lambda |\mathbf{H}| l\Lambda + 1JN\Lambda + 1\rangle = A\sqrt{\frac{2}{2 - \delta_{\Lambda 0}}}\sqrt{l(l+1) - \Lambda(\Lambda+1)}\sqrt{(N-\Lambda)(N+\Lambda+1)}$$
$$\times \frac{N(N+1) + S(S+1) - J(J+1)}{4N(N+1)},$$
(4.15)

while for $\Delta\Lambda = \pm 1, \Delta N = \pm 1$:

$$\langle l\Lambda JN\Lambda |\mathbf{H}| l\Lambda + 1JN + 1\Lambda + 1\rangle = A\sqrt{\frac{2}{2 - \delta_{\Lambda 0}}}\sqrt{l(l+1) - \Lambda(\Lambda+1)}$$
$$\times \sqrt{\frac{[(J+N+1)(J+N+2) - S(S+1)][S(S+1) - (J-N)(J-N-1)]}{16(N+1)^2(2N+1)(2N+3)}}$$
$$\times \sqrt{\frac{(N+\Lambda+1)(N+\Lambda+2)}{16(N+1)^2(2N+1)(2N+3)}}.$$
(4.16)

4.3.3   Single state fits

The onset of predissociation at relatively low n* (n* ~ 3) in CaCl presents a considerable challenge to OODR signal acquisition. The paucity of data for this low-n*

region is in marked contrast to the vast data sets acquired in this region for both CaF and BaF. This situation changes above the first ($v^+ = 0$) IP, where autoionization becomes the dominant nonradiative pathway and Rydberg series are prominent, as discussed in Chapter 6.

Despite this difficulty, four Rydberg series (three $^2\Sigma^+$ and one state that is either $^2\Pi$ or $^2\Delta$) found in the predissociated region were recorded and fit to a case (b) Hamiltonian. The well-known energy level expressions for $^2\Sigma^+$ states in terms of spectroscopic constants are: [50]

$$E = T_v + B_v \cdot N(N+1) - D_v \cdot N^2(N+1)^2$$
$$+ 1/2(\gamma_{sr,v} + \gamma_D N(N+1)) \cdot N \text{ for } J = N + 1/2$$
$$- 1/2(\gamma_{sr,v} + \gamma_D N(N+1)) \cdot (N+1) \text{ for } J = N - 1/2$$

$$(4.17)$$

with

$$T_v = T_e + \omega_e(v + 1/2) - \omega_e x_e(v + 1/2)^2, \tag{4.18}$$
$$B_v = B_e - \alpha_e(v + 1/2) + \gamma_e(v + 1/2)^2, \tag{4.19}$$
$$D_v = D_e + \beta_e(v + 1/2), \quad \text{and} \tag{4.20}$$
$$\gamma_{sr,v} = \gamma_{sr,e} + \alpha_\gamma(v + 1/2). \tag{4.21}$$

For a fit of rotational levels belonging to a single vibrational state, the vibrational frequency terms in T_v do not apply. While B_v is clearly the most well-defined parameter in fits of this type, other higher-order terms may be necessary. While it is easy enough to include them in a least-squares fit to determine whether if their presence lowers the overall variance, one can make simple *a priori* calculations to determine their relevance before fitting. Two examples are D_v, the centrifugal distortion term, and $\gamma_{sr,v}$, the spin-rotation interaction term. In the case of D_v, the Kratzer relationship can be used to get a first-order estimate [50]:

$$D_e = \frac{4B_e^3}{\omega_e{}^2} \tag{4.22}$$

Using the typical CaCl$^+$ Rydberg values of B_e (0.164 cm^{-1}) and ω_e (450 cm^{-1}), we obtain $D_e = 8.71 \times 10^{-8}$ cm^{-1}. Since this term goes as $(N(N+1))^2$, we can calculate the magnitude of D_v for $N = 2$ and $N = 17$, which are the lowest and highest N levels accessed in these OODR spectra, respectively. This simple calculation shows that D_v contributes to the rotational energy from $\approx 3 \times 10^6$ cm^{-1} for $N = 2$ to 0.008 cm^{-1} for $N = 17$. Since the experimental precision in our spectra is considered to be 0.02 cm^{-1}, this term can be ignored.

It should be noted that no empirical Kratzer-like relationship exists for estimating the magnitude of $\gamma_{sr,v}$, but a reasonable value would be the known value for the D n* $= 2.51$ $^2\Sigma^+$ state ($\gamma_{sr,v} = 0.0013$ cm^{-1}), since there is no n* scaling dependence for $\gamma_{sr,v}$ [6]. A similar calculation for $\gamma_{sr,v}$ shows that the magnitude of contributions from $\gamma_{sr,v}$ range from 0.001 cm^{-1} for $N = 2$ to 0.010 cm^{-1} for $N = 17$. Inclusion of this term as a fixed value improved the fits slightly.

The reduced term value plot for the n* $= 6.49$ $^2\Sigma^+$ $v = 0$ state (see Fig. 4.4) shows that $N = 13$ and $N = 15$ are perturbed by nearby (unseen) states. The reduced term value plot for the n* $= 4.98$ $^2\Sigma^+$ $v = 2$ state (see Fig. 4.4) shows a slight shift at $N = 4$ which is also indicative of a perturbation. The n* $= 5.16$ $v = 3$ state does not appear to be perturbed. The presence of a $v = 3$ state is somewhat surprising considering the highly diagonal ($\Delta v = 0$) Franck-Condon factors expected from the D $^2\Sigma^+$ $v = 1$ intermediate state, and would be an excellent candidate for an isotope shift analysis via Ca^{37}Cl to confirm the assignment.

Rydberg series assignments were difficult to make in two cases. The state with $T_v = 45\ 684.0$ cm^{-1} is clearly not a $\Lambda = 0$ state, as it has a 5 line pattern for each N. According to theoretical calculations by Jungen $et\ al.$, the only non-$^2\Sigma^+$ core-penetrating states expected in this region are the 6.30 $^2\Pi$ $v = 0$ and the 5.12 $^2\Delta$ $v = 3$ states. An assignment from the survey spectra has the position of the 6.30 $^2\Pi$ $v = 0$ state as 45 745.0 cm^{-1}, some $\approx$60 cm^{-1} higher. Unfortunately isotope shift

data is not available for this state, as it would allow unambiguous determination of v. The reduced term value plot (see Fig. 4.4) shows a slight curvature with increasing N, which is indicative of a heterogeneous perturbation (i.e. one that scales with N) with a higher lying state. Several attempts were made to deperturb this state by introducing an off-diagonal matrix element of the form $2B_v(N(N+1)-2)^{1/2}$, which describes the N-dependent interaction between the remote perturber (which must be a $^2\Pi$ state if we consider the $T_v = 45\ 684.0$ cm^{-1} state to be a $^2\Delta$ state and $^2\Delta$ if we consider it to be a $^2\Pi$ state) [56]. No well-determined interaction parameter $2B_v$ was found, nor was the variance of the fit improved with a heterogeneous perturber model exhaustively explored.

The state with $T_v = 45\ 051.2$ cm^{-1} (assigned as n* $= 4.98$ $^2\Sigma^+$ $v = 2$) lies in the same region as the n* $= 5.30$ $^2\Pi$ state as assigned from the survey spectra. Since the 0.98 series is nominally non-penetrating, it is likely that these levels are borrowing some intensity from a nearby bright state, possibly the nearby n* $= 5.30$ $^2\Pi$ state. The OODR spectra in this region clearly show the P-R two line pattern expected from a $^2\Sigma^+$ state. The survey spectrum, however, shows a decidedly non-$^2\Sigma^+$ band contour (see Fig. 3-11) which is definitely affected by predissociation (see Fig. 3-15). The dissimilarity in the two spectra most likely arises from the different experimental techniques used to access these states, and is related to a competition between the ionization and predissociation.

A simple kinetic argument can be used to describe the competition between ionization and predissociation in terms of population and laser flux. Let us consider a two-level system where the population of the launch state is designated N_1 and the Rydberg state population is N_2 (see Fig. 4.3.3). In this schematic, k_1 is defined to be the excitation rate from the launch state N_1 to the Rydberg state N_2, k_2 is the predissociation rate from N_2, and k_3 is the ionization rate from N_2. A rate law can be written for the change in N_2 with respect to time:

$$\frac{dN_2}{dt} = k_1 N_1 - k_2 N_2 - k_3 N_2. \tag{4.23}$$
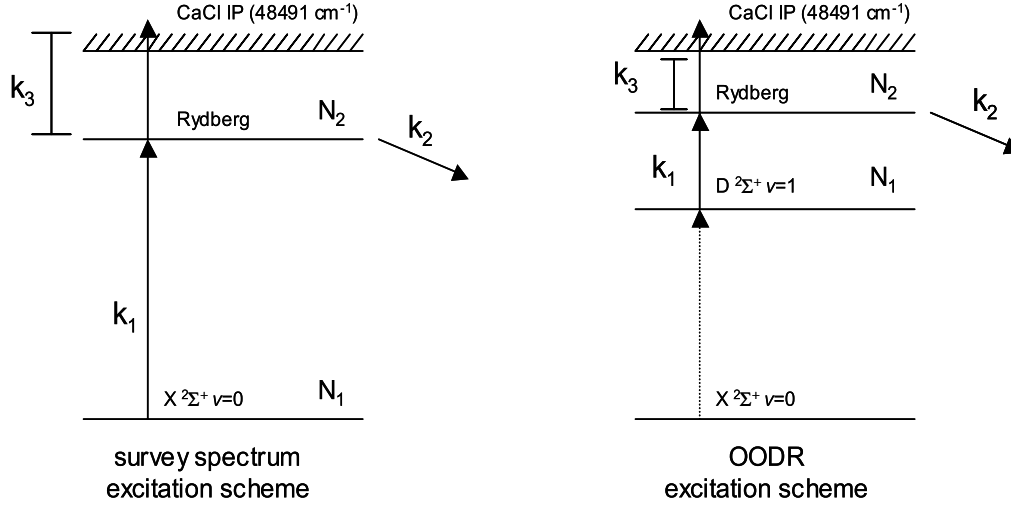
Figure 4-7: Excitation schemes for survey and OODR experiments in terms of rates. The launch state N_1 in the OODR scheme is assumed to have the maximum possible population transfer from the ground state.

assuming that steady state kinetics is valid, we can write

$$0 = \frac{dN_2}{dt} = k_1 N_1 - k_2 N_2 - k_3 N_2. \tag{4.24}$$

and find an expression for N_2:

$$N_2 = \frac{k_1 N_1}{k_2 + k_3}. \tag{4.25}$$

since the ion signal is $k_3 N_2$, which can be combined with Eq. 4.25:

$$\text{ion signal} = k_3 \frac{k_1 N_1}{k_2 + k_3}. \tag{4.26}$$

While we do not know the magnitudes of k_1, k_2, and k_3, we do recognize what

they must be proportional to:

$$k_1 \quad \propto \quad I_{laser1}\frac{1}{\Delta\nu} \tag{4.27}$$

$$k_2 \quad \propto \quad \Delta\nu \tag{4.28}$$

$$k_3 \quad \propto \quad I_{laser2}. \tag{4.29}$$

where I_{laser} is the intensity of laser 1 and 2 and $\Delta\nu$ is the resonant linewidth of the transition. These proportionalities allow us to rewrite Eq. in terms of laser intensity:

$$\text{ion signal} = I_{laser2}\frac{I_{laser1}N_1}{(\Delta\nu)^2 + I_{laser2}\Delta\nu}. \tag{4.30}$$

This equation encapsulates the interplay between ionization and predissociation. If the linewidth becomes large (i.e. indicating an increase in predissociation rate), the increase in $(\Delta\nu)^2$ will make the ion signal small:

$$\text{ion signal}(\Delta\nu \to \infty) \approx \frac{I_{laser1}I_{laser2}N_1}{(\Delta\nu)^2}. \tag{4.31}$$

In the other limit, when $I_{laser2} >> (\Delta\nu)^2$, we have:

$$\text{ion signal}(I_{laser2} \to \infty) \approx I_{laser1}N_1, \tag{4.32}$$

which is the population transferred to level N_2 by the first laser. While this kinetic analysis is admittedly simplistic, it shows that the ion yield is a function of both the predissociation rate and the intensity of the ionizing laser, and is a step toward explaining the paucity of observed states via OODR experiments in the extensively predissociated n* = 5-7 region. Since the laser intensity was much higher when recording the survey spectra than the OODR spectra ($\sim$500 μJ/pulse for the excitation/ionization step vs. 200 - 300 μJ/pulse for the excitation/ionization step in the OODR experiments), it is reasonable to assume that there would be more ion signal from predissociated levels in the survey experiments than from OODR experiments. This finding casts doubt on our ability to record spectra of strongly predissociated

Table 4.1: Results of least squares fits for low-n* OODR data. (1-σ) error in parentheses.

State (n*,v)	T_v (cm^{-1})	B_v (cm^{-1})	$\gamma_{sr,v}$ (cm^{-1})
4.98 $^2\Sigma^+$ $v = 2$	45051.2 (1)	0.1549 (16)	1.3×10^6 (fixed)
5.16 $^2\Sigma^+$ $v = 3$	45687.3 (3)	0.1616 (1)	1.3×10^6 (fixed)
6.49 $^2\Sigma^+$ $v = 0$	45886.3 (1)	0.1672 (9)	1.3×10^6 (fixed)
6.30 $^2\Pi$ $v = 0$	45684.0 (5)	0.153 (2)	1.3×10^6 (fixed)
or			
5.11 $^2\Delta$ $v = 3$			

states using the conventional OODR technique described here, as relatively low powers are necessary to minimize undesirable multiphoton effects. The relatively low laser power in the OODR experiments also precludes the detection of atomic ions produced by non-resonant multiphoton ionization of Ca or Cl, as had been previously detected in the high-power survey studies at UV wavelengths.

4.4   Conclusion

Despite the presence of predissociation in the n* = 5-7 region, a handful of states were detected by OODR techniques and are summarized with their fitted constants in Table 4.1. The vibrational (and hence n*) assignment of at least one of the states is in question, although this ambiguity could easily be dispelled with the recording of data using Ca^{37}Cl isotopomer. The fitted values of B_v are largely in line with the canonical CaCl$^+$ value of 0.164 cm^{-1} [22]. The use of ionization detection for observing predissociated states is called into question by a comparison of results from survey spectra (see Chapter 3) recorded with relatively high laser intensity and results from these OODR experiments using relatively low laser intensity. The competition between ionization and predissociation and its dependence on laser power was explored with a simple kinetic argument.
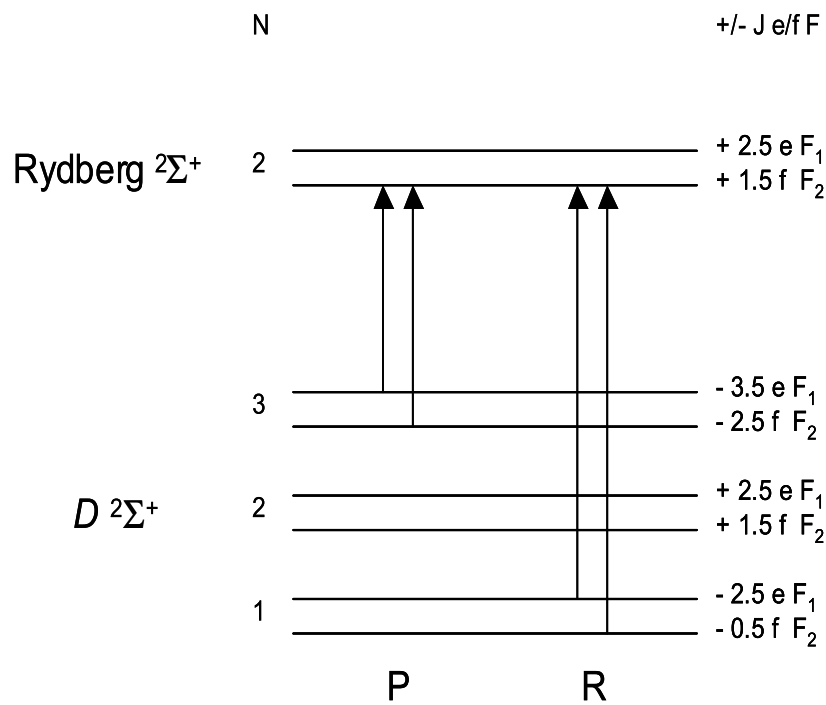
Figure 4-8: Transition level diagram demonstrating lower-state combination differences principle. By pumping successive N components in the intermediate state, the same level in the upper state can be accessed due to the transition selection rules.
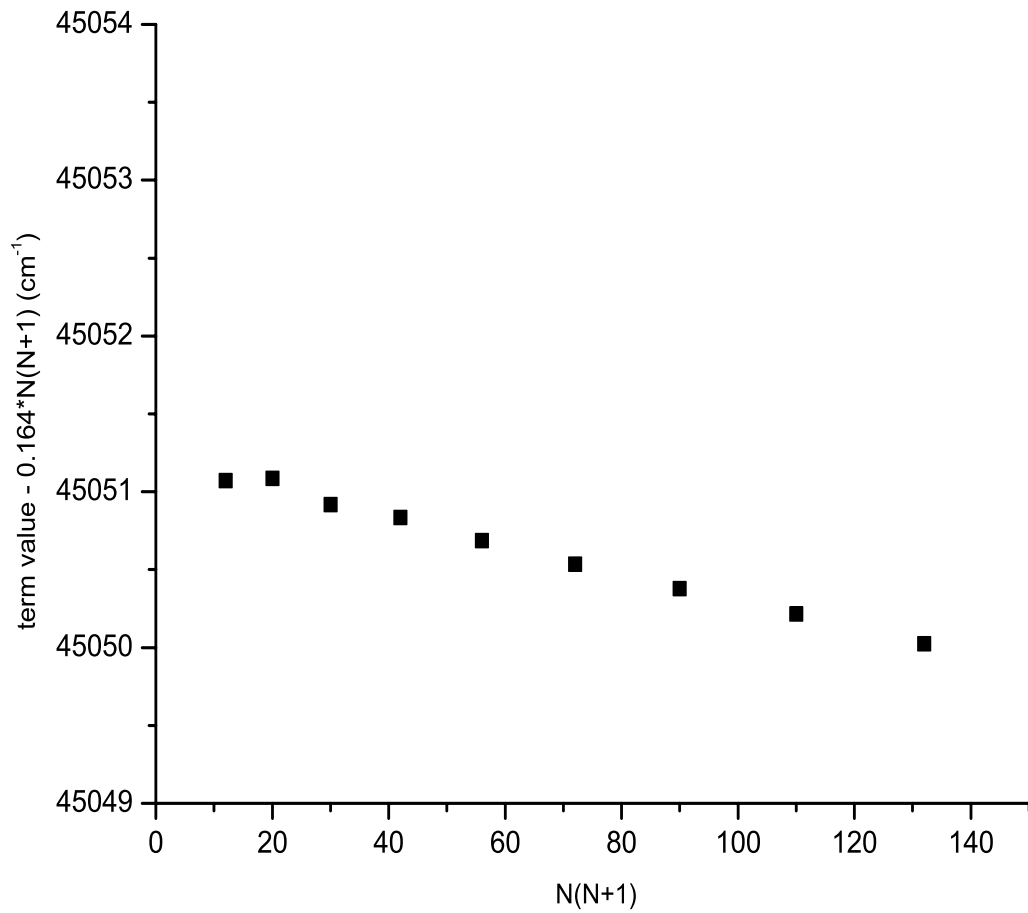
Figure 4-9: Reduced term value plot for the n* = 4.98 $^2\Sigma^+$ $v = 2$ Rydberg state observed via OODR.
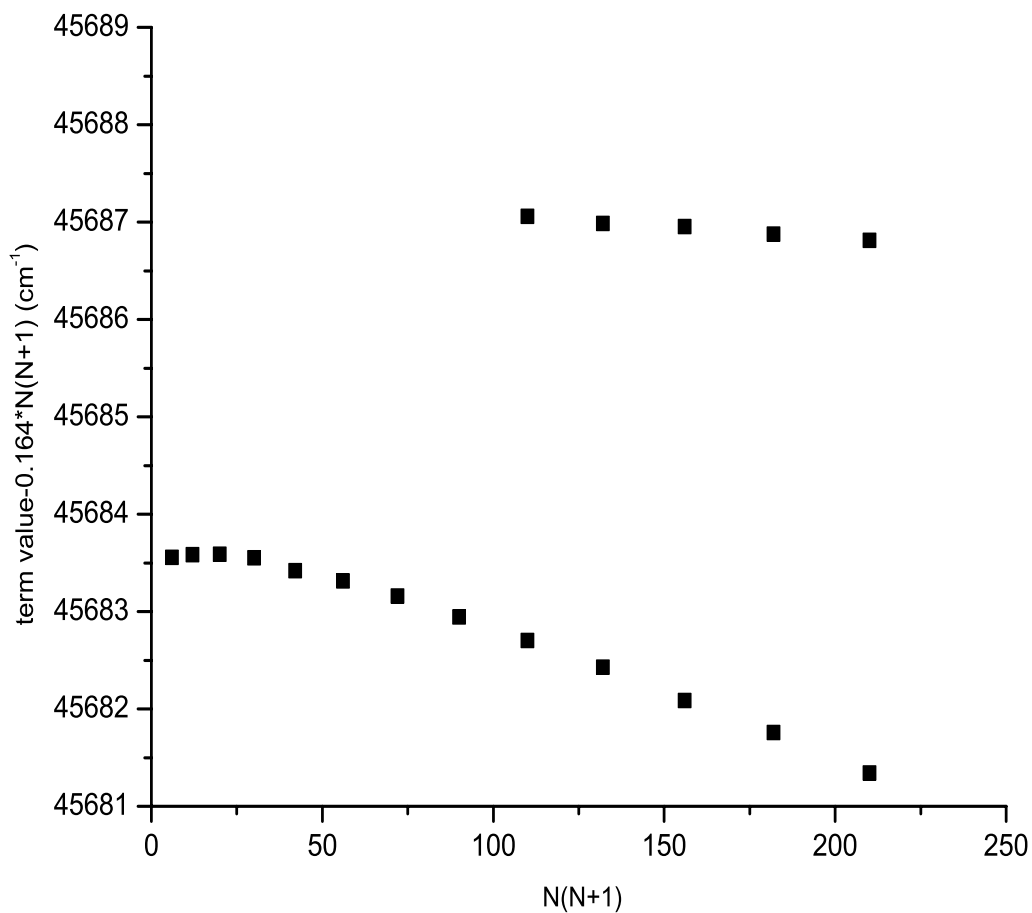
Figure 4-10: Reduced term value plot for the n* = 5.16 $^2\Sigma^+$ $v = 3$ and n* = 6.30 $^2\Pi$ $v = 0$ (or 5.11 $^2\Delta$ $v = 3$ state) observed via OODR.
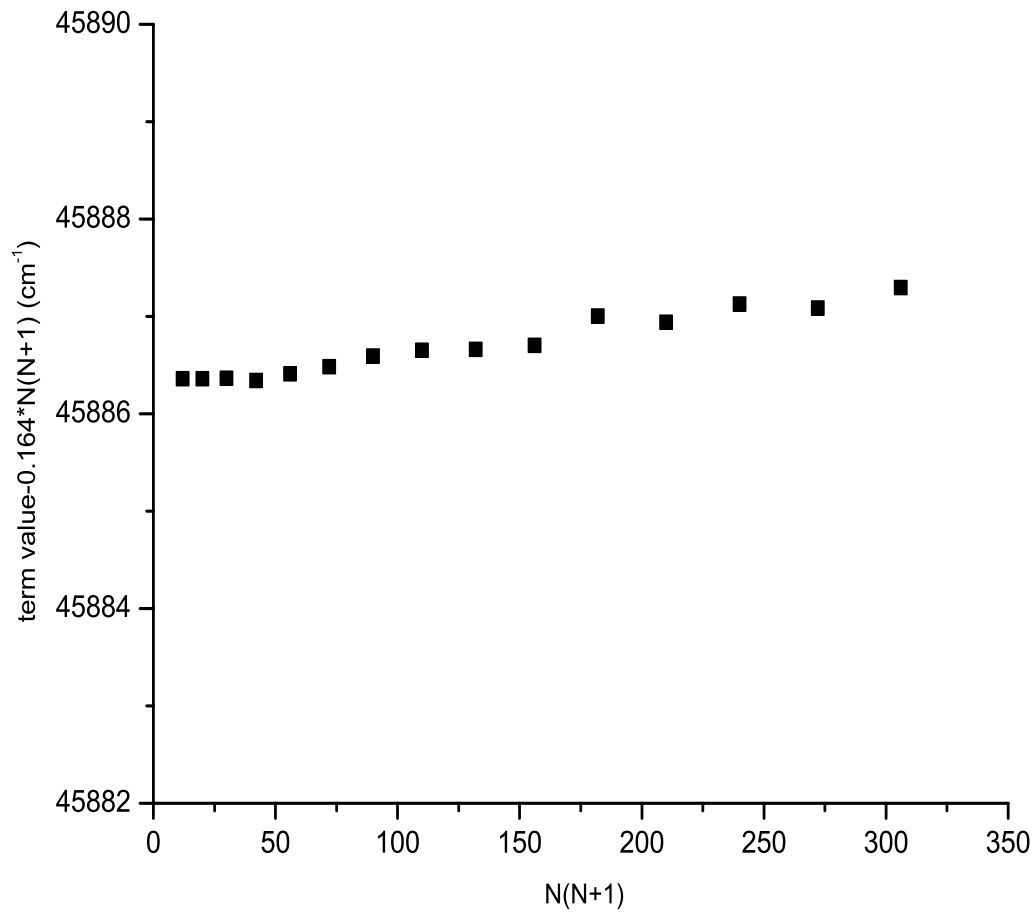
Figure 4-11: Reduced term value plot for the n* = 6.49 $^2\Sigma^+$ $v = 0$ Rydberg state observed via OODR.

Table 4.2: Energy levels of the X $^2\Sigma^+$ $v = 0$ and D $^2\Sigma^+$ $v = 1$ states of CaCl for $J < 25$ calculated from Ref. [6]. All energies in cm^{-1}.

N	X state F$_{1e}$ levels	J F$_{1e}$	X state F$_{2f}$ levels	J F$_{2f}$	D state F$_{1e}$	D state F$_{2f}$
0	0.0	0.5	n/a	n/a	31557.524	n/a
1	0.001	1.5	0.001	0.5	31557.847	31557.846
2	0.304	2.5	0.302	1.5	31558.190	31558.190
3	0.912	3.5	0.909	2.5	31558.554	31558.553
4	1.824	4.5	1.819	3.5	31558.937	31558.936
5	3.039	5.5	3.033	4.5	31559.340	31559.340
6	4.558	6.5	4.551	5.5	31559.763	31559.763
7	6.381	7.5	6.372	6.5	31560.206	31560.206
8	8.507	8.5	8.497	7.5	31560.669	31560.669
9	10.937	9.5	10.925	8.5	31561.151	31561.152
10	13.671	10.5	13.657	9.5	31561.654	31561.655
11	16.708	11.5	16.693	10.5	31562.177	31562.177
12	20.048	12.5	20.032	11.5	31562.719	31562.720
13	23.692	13.5	23.675	12.5	31563.281	31563.282
14	27.640	14.5	27.621	13.5	31563.863	31563.864
15	31.891	15.5	31.871	14.5	31564.465	31564.467
16	36.445	16.5	36.424	15.5	31565.087	31565.089
17	41.303	17.5	41.280	16.5	31565.729	31565.731
18	46.464	18.5	46.440	17.5	31566.391	31566.393
19	51.928	19.5	51.903	18.5	31567.072	31567.074
20	57.696	20.5	57.669	19.5	31567.774	31567.776
21	63.767	21.5	63.738	20.5	31568.495	31568.497
22	70.140	22.5	70.111	21.5	31569.236	31569.239
23	76.818	23.5	76.787	22.5	31569.997	31570.000
24	83.798	24.5	83.765	23.5	31570.778	31570.781
25	91.081	25.5	91.047	24.5	31571.579	31571.582

Table 4.3: OODR from D (1,0) band. Possible assignments are 5.30 $^2\Pi\, v = 0$ or 5.11 $^2\Delta\, v = 3$. All energies in cm^{-1} and referenced to $X\ ^2\Sigma^+ v = 0$, $N = 0$.

J	F_{1e}	F_{1f}	F_{2e}	F_{2f}
2.5	-	45684.54	-	45685.55
3.5	45685.55	45685.55	45686.87	45686.87
4.5	45686.87	45686.87	45688.47	45688.47
5.5	45688.47	45688.47	45690.31	45690.31
6.5	45690.31	45690.31	45692.50	45692.50
7.5	45692.50	45692.50	45694.97	45694.97
8.5	45694.97	45694.97	45697.70	45697.70
9.5	45697.70	45697.70	45700.74	45700.74
10.5	45700.74	45700.74	45704.08	45704.08
11.5	45704.08	45704.08	45707.67	45707.67
12.5	45707.67	45707.67	45711.61	45711.61
13.5	45711.61	45711.61	-	45715.78
14.5	45715.78	-	-	-

Table 4.4: OODR from D (1,0) band. Assignment is n*=5.16 $^2\Sigma^+ v = 3$. All energies in cm^{-1} and referenced to $X\ ^2\Sigma^+ v = 0$, $N = 0$. Quantity in parentheses is observed-calculated from least squares fit in terms of the last digit.

J	F_{1e}	F_{2f}
9.5	-	45705.090 (0)
10.5	45705.090 (0)	45708.644 (-2)
11.5	45708.644 (-2)	45712.527 (2)
12.5	45712.527 (2)	45716.726 (-1)
13.5	45716.726 (-1)	45721.252 (0)
14.5	45721.252 (0)	-

Table 4.5: OODR from D (1,0) band. Assignment is n* = 4.98 $^2\Sigma^+$ v = 2. All energies in cm^{-1} and referenced to X v=0,N=0. Quantity in parentheses is observed-calculated from least squares fit in terms of the last digit.

J	F_{1e}	F_{2f}
2.5	-	45053.04 (-3)
3.5	45053.04 (-3)	45054.37 (6)
4.5	45054.37 (6)	45055.84 (-2)
5.5	45055.84 (-2)	45057.72 (1)
6.5	45057.72 (1)	45059.87 (-1)
7.5	45059.87 (-1)	45062.34 (-2)
8.5	45062.34 (-2)	45065.14 (-1)
9.5	45065.14 (-1)	45068.26 (1)
10.5	45068.26 (1)	45071.67 (1)
11.5	45071.67 (1)	-

Table 4.6: OODR from D (1,0) band. Assignment is n*=6.49 $^2\Sigma^+$ v = 0. All energies in cm^{-1} and referenced to X v = 0,N = 0. Quantity in parentheses is observed-calculated from least squares fit in terms of the last digit.

J	F_{1e}	F_{2f}
2.5	-	45888.33 (5)
3.5	45888.33 (5)	45889.64 (2)
4.5	45889.64 (2)	45891.28 (0)
5.5	45891.28 (0)	45893.23 (-6)
6.5	45893.23 (-6)	45895.59 (-4)
7.5	45895.59 (-4)	45898.29 (-2)
8.5	45898.29 (-2)	45901.35 (2)
9.5	45901.35 (2)	45904.69 (2)
10.5	45904.69 (2)	45908.31 (4)
11.5	45908.31 (4)	45912.29 (-8)
12.5	45912.29 (-8)	45916.85 (13)
13.5	45916.85 (13)	45921.34 (-2)
14.5	45921.34 (-2)	45926.49 (6)
15.5	45926.49 (6)	45931.70 (-7)
16.5	45931.70 (-7)	45937.48 (2)
17.5	45937.48 (2)	-
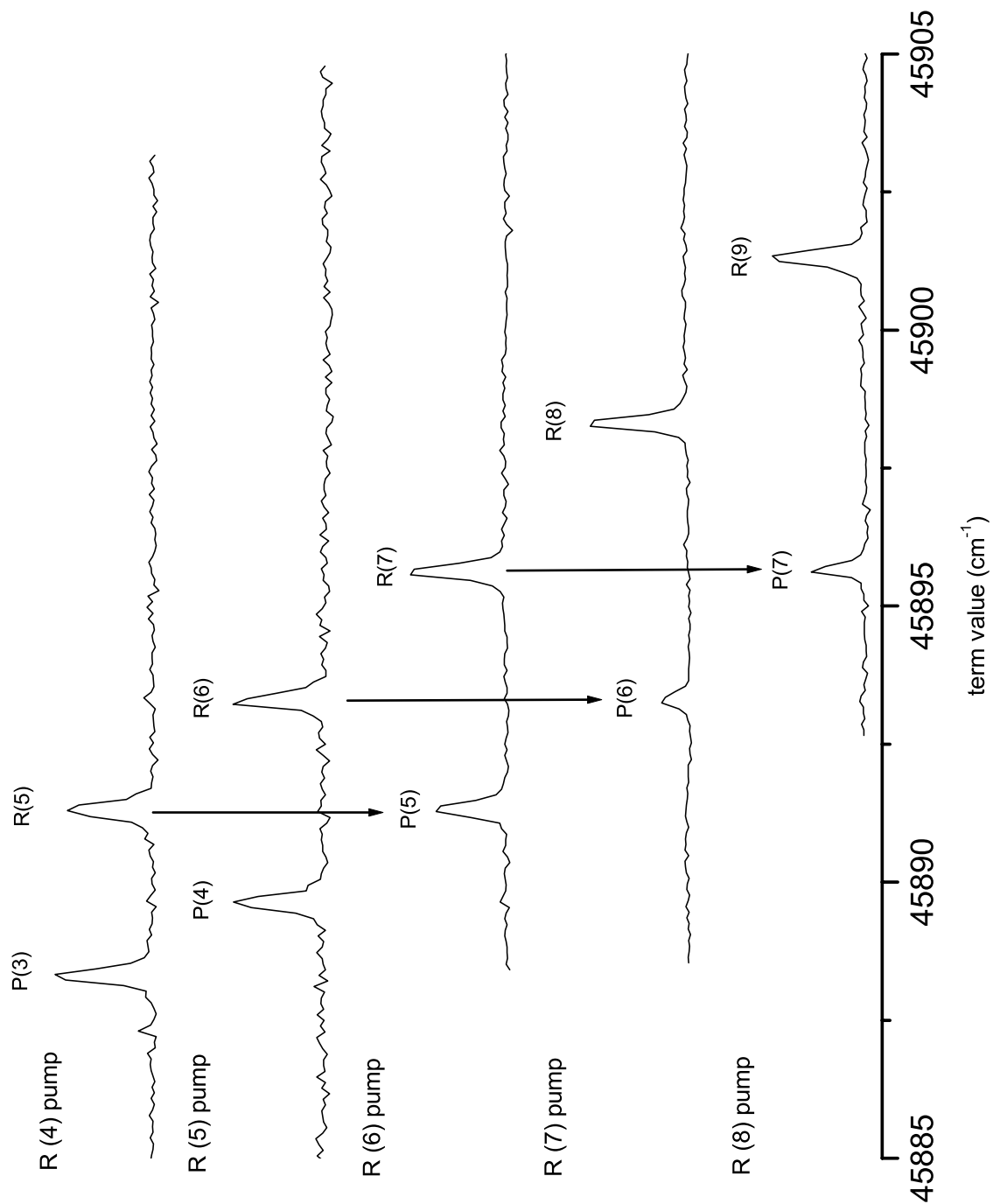
Figure 4-12: Stacked plot for the n* = 6.49 $^2\Sigma^+$ $v = 0$ state showing how successive intermediate state N pumping allows access to the same levels in the excited state. This technique is a powerful tool for the analysis of Rydberg state rotational structure.

Chapter 5

The Predissociation Mechanism for $^2\Sigma^+$ Rydberg States of CaCl

5.1 Introduction

The Rydberg states of the alkaline earth monohalide molecules have been extensively studied by spectroscopic and theoretical means [9–13]. These molecules have highly polar molecular-ion cores (MX$^+$), the properties of which can be understood in terms of two closed-shell polarizable atomic ions, M^{2+} and X$^-$. While the properties of the valence states of these molecules have been treated by Rice *et al.* using a ligand field model [17,18] and by Törring *et al.* [19] using an electrostatic polarization model, the departures of the properties of the molecular Rydberg states from those of hydrogenic one-electron states can be represented by a set of molecular quantum defects derivable from M$^+$ atomic-ion quantum defects [59]. It is convenient to express the energies of molecular Rydberg states in terms of the effective principal quantum number, n*, which is defined by the generalized Rydberg equation

$$IP - E_{n^*} = \frac{RZ^2}{n^{*2}}, \qquad (5.1)$$

where IP is the ionization potential [48 491 cm^{-1} ($v^+ = 0$, $N^+ = 0 \rightarrow v = 0$, $N = 0$) for CaCl], E_{n^*} is the Rydberg energy in cm^{-1}, R is the Rydberg constant, and

Z is the integer charge on the Rydberg ion core [16].

Recent spectroscopic studies of Rydberg states of CaCl have revealed interesting differences between CaCl and its better known homologue, CaF. The main differences in the Rydberg spectra of these two molecules arise from the fact that the dissociation limit of CaCl lies much farther below its first ionization limit than is the case in CaF: (IP$_1$-D$_o$ = 2 800 cm^{-1} (n* $\sim$ 6.3) for CaF [11], 15 300 cm^{-1} (n* $\sim$ 2.7) for CaCl [16]). Thus, unlike CaF, the low-n* Rydberg states of CaCl are expected to be extensively perturbed (predissociated) by two repulsive or weakly-bound $^2\Pi$ and $^2\Sigma^+$ states which dissociate to M(^{1}S) + X (^{2}P) neutral atoms (see Fig. 5-1). This low-n* predissociation onset in CaCl creates considerable difficulties for experimental studies of low Rydberg states by conventional fluorescence and REMPI-TOF (Resonance-Enhanced Multiphoton-Time Of Flight) methods, by which states between n*= 4 and 16 had previously escaped detection [16]. However, recent experimental work by Li *et al.* and this author have provided access to the CaCl Rydberg region strongly affected by predissociation [22]. This chapter presents what is presently known about CaCl Rydberg predissociation dynamics, while the companion chapters detail the experimental schemes employed as well as the locations of the manifold of CaCl $^2\Sigma^+$ Rydberg states.

5.2 Theory

In general, in the diabatic picture, the interaction between bound Rydberg and continuum states is determined by [56]

$$H_{v,J;E,J} = \langle \Psi_{1,v,J} | \mathbf{H} | \Psi_{2,E,J} \rangle \tag{5.2}$$

$$= \langle \Phi_1(r,R)\chi_{v,J}(R) | \mathbf{H} | \Phi_2(r,R)\chi_{E,J}(R) \rangle \tag{5.3}$$

where $H_{v,J;E,J}$ is the interaction matrix element, $\mathbf{H}$ is the coupling operator responsible for the predissociation, $\Psi_{1,v,J}$ and $\Psi_{2,E,J}$ are the total wavefunctions, $\Phi_1(r,R)$
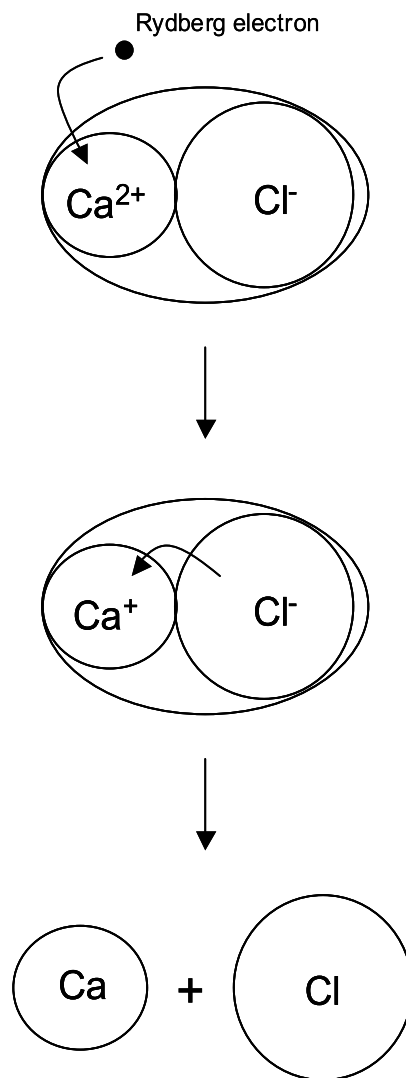
Figure 5-1: Idealized two-step mechanism for predissociation of CaCl. In the first step, the Rydberg electron enters the Ca^{2+} $4s$ spatial region. The second simultaneous step involves transfer of a Cl^{-1} $3p\sigma$ or $3p\pi$ electron to Ca^{+}, producing neutral Ca and Cl atoms. This interaction is governed by a two-electron e^2/r_{12} matrix element. One naively expects that this electronic matrix element will be larger for predissociation of $^2\Sigma^+$ than $^2\Pi$ Rydberg states, and largest for the $^2\Sigma^+$ series with the X $^2\Sigma^+$ ground state as its terminus.

and $\Phi_2(r, R)$ are the diabatic electronic wave functions, and $\chi_{v,J}(R)$ and $\chi_{E,J}(R)$ are the vibrational wavefunctions of the diabatic bound and continuum electronic states respectively (with the condition that $\chi_{E,J}(R)$ is energy-normalized in a manner discussed below) [60]. If we consider the diabatic representation, and assume that the electronic matrix element is either independent of or linear in R, we can factor $H_{v,J;E,J}$ into electronic and nuclear matrix elements:

$$H_{v,J;E,J} = \langle \Phi_1(r, R) \left| \mathbf{H} \right| \Phi_2(r, R) \rangle \langle \chi_{v,J}(R) | \chi_{E,J}(R) \rangle \tag{5.4}$$

$$= H^e \left\langle \chi_{v,J}(R) \mid \chi_{E,J}(R) \right\rangle, \tag{5.5}$$

where H^e is the electronic factor evaluated at $R = R_c$, the location of the crossing between the two potential curves. We can use the Fermi Golden Rule expression for the linewidth Γ, noting that the usual density of states term is unnecessary due to the use of energy-normalized wavefunctions:

$$\Gamma_{v,J} = 2\pi \left| H_{v,J;E,J} \right|^2. \tag{5.6}$$

Combining Eqs. 5.5 and (5.6) we obtain

$$\Gamma_{v,J} = 2\pi \left| H^e \right|^2 \left| \left\langle \chi_{v,J}(R) \mid \chi_{E,J}(R) \right\rangle \right|^2, \tag{5.7}$$

where we recognize that $\left| \left\langle \chi_{v,J}(R) \mid \chi_{E,J}(R) \right\rangle \right|^2$ is the expression for the Franck-Condon Density (FCD) with dimension of E^{-1} (i.e., cm, since spectroscopic units of cm^{-1} are used for E). The interaction between the bound Rydberg state and the repulsive state may be characterized experimentally by taking ratios of linewidths:

$$\frac{\Gamma(v = m)}{\Gamma(v = n)} = \frac{\langle \chi_{m,J}(R) \mid \chi_{E',J}(R) \rangle^2}{\langle \chi_{n,J}(R) \mid \chi_{E'',J}(R) \rangle^2}, \tag{5.8}$$

where m and n are different vibrational levels of the bound Rydberg electronic state and E' and E'' refer to the continuum nuclear wavefunction appropriate for overlap with the m and n vibrational levels, respectively. In this way the value of the observ-

able, Γ, is directly related to a calculable quantity (the FCD) that is dependent on the exact locations and shapes of the two potential curves. If approximate molecular constants for the bound Rydberg states are known, it is then possible to determine the location of the intersection of each Rydberg state with the repulsive curve as well as the slope of the repulsive curve at the intersection point, R_c.

5.3   Calculations and Discussion

From ion-dip experiments in the n* = 4-8 energy range we measured linewidths, which varied reproducibly and systematically in two Rydberg states for $v = 0, 1$, and 2, spanning a range of rotational quantum numbers, $6 < N < 25$ (see Fig. 5-3) [22]. In our calculations we applied Eq. (5.8) with the bound Rydberg series described by the following molecular constants: ω_e=452.81 cm^{-1}, $\omega_e x_e = 1.35$ cm^{-1}, B_e=0.167 cm^{-1}, $r_e = 2.327$ Å (for Ca^{35}Cl) [1]. We assumed a one-parameter form for the repulsive curve,

$$E(cm^{-1}) = \frac{C_{12}}{R^{12}} + D_e \qquad (5.9)$$

where C_{12} has the units Å^{12} cm^{-1} and $D_e = 33\ 171$ cm^{-1} +/- 1048 cm^{-1} for CaCl [47]. The nuclear wavefunctions were calculated by a numerical integration method with appropriate energy normalization of the continuum wavefunctions [60]. Since this method is extensively described in Ref. [60] we will only mention here that the asymptotic amplitudes of the continuum wavefunctions were normalized to $0.2788(\mu/E)^{1/4}$ in units of cm^{-1} Å, where μ is the reduced mass of CaCl and E is the asymptotic kinetic energy in cm^{-1}. Parametric adjustment of C_{12} was carried out to give the best agreement between the calculated ratios of FCDs and the observed ratios of linewidths for three vibrational levels in each of two electronic Rydberg series. As can be seen in Fig. 5-3, there was an optimum choice of C_{12} which minimized the disparity between the observed and calculated linewidth ratios for each Rydberg state.

---

[1]These are fitted constants from least squares analysis of three vibrational levels of the n* = 6.49 series from both Ca^{35}Cl and Ca^{37}Cl (6 levels total).
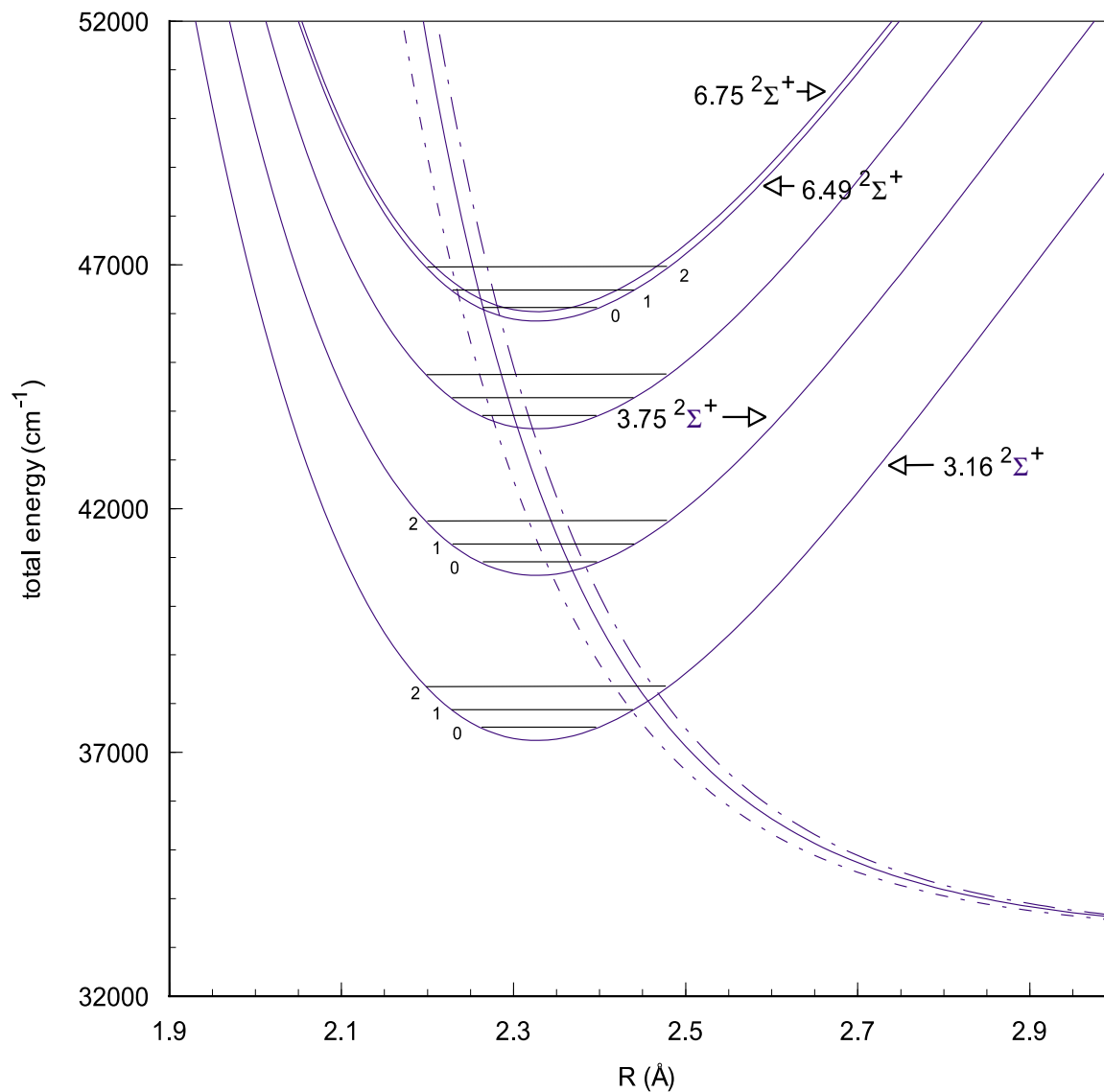
Figure 5-2: Diabatic potential energy curves for $^2\Sigma^+$ Rydberg states and the repulsive $^2\Sigma^+$ state. The dashed lines represent confidence limits for the position of the repulsive state (See Fig. 5-3 and text). The $^2\Pi$ repulsive curve is expected to be considerably steeper, and its intersection of the $^2\Pi$ Rydberg potential curves may never approach R_e^+, even as n*$\to \infty$.

state (n*)	v	Γ_{obs}[a] (cm^{-1})	range of N	ratio	observed ratio[a]	calculated ratio with C$_{12}$ parameter ($\times 10^{-8}$)								
						1.750	2.000	2.061	**2.335**	**2.354**	**2.374**	2.573	2.750	3.250
6.49	0	0.6(2)	16-25	$\Gamma(v=0)\,/\,\Gamma(v=1)$	0.7(2)	0.2	0.3	0.3	**0.5**	**0.5**	0.5	0.8	1.4	30.4
	1	1.0(1)	6-15	$\Gamma(v=1)\,/\,\Gamma(v=2)$	0.8(2)	0.4	0.6	0.7	**1.4**	**1.4**	1.6	4.4	5.9	0.1
	2	1.2(2)	16-25	$\Gamma(v=0)\,/\,\Gamma(v=2)$	0.6(2)	0.1	0.2	0.2	**0.6**	**0.7**	0.8	3.7	82.1	2.8
6.75	0	0.6(1)	16-25	$\Gamma(v=0)\,/\,\Gamma(v=1)$	0.6(1)	0.2	0.1	0.3	0.4	**0.5**	**0.5**	0.8	1.2	16.9
	1	1.0(2)	7-15	$\Gamma(v=1)\,/\,\Gamma(v=2)$	0.9(2)	0.4	0.1	0.5	1.2	**1.3**	**1.4**	3.4	21.8	0.2
	2	1.1(2)	16-25	$\Gamma(v=0)\,/\,\Gamma(v=2)$	0.6(1)	0.1	0.1	0.2	0.5	**0.6**	**0.7**	2.6	26.9	3.2

[a] Standard errors (1σ) in parentheses.

Figure 5-3: Observed Linewidths and Calculated Linewidth Ratios for $v = 0\text{-}2$ of Rydberg- $^2\Sigma^+$ Repulsive State Interactions

The highlighted value of C_{12}, $2.354 \times 10^8 \text{Å}^{12}$ cm^{-1}, is offered as the value which gives the best agreement when considering levels from both Rydberg series simultaneously.

As uncertainty in an analysis of this type comes mainly from the measurements of linewidths, we adjusted C_{12} to reflect the ranges of the ratios consistent with the 1σ uncertainty of the linewidth measurements. In this manner we were able to determine a confidence limit for the position of the repulsive state, which is illustrated in Fig. 5-2. The values of the C_{12} parameter, which represent the lower and upper limits of the confidence range, are 2.061×10^8 Å^{12} cm^{-1} and 2.573×10^8 Å^{12} cm^{-1} respectively. From our derived repulsive curve we calculated the electronic matrix element H^e for both Rydberg series by substituting the observed Γ and calculated FCD into Eq. (5.7).

It is not immediately obvious that the location of a repulsive state determined in this manner (i.e., only quantitatively valid over the $\sim$400 cm^{-1} sampled, $6.4 < $ n* < 6.8) will yield accurate computed linewidths for a considerably wider range of n*. There is, however, qualitative evidence which supports the accuracy of the derived repulsive curve at lower energies (n* = 3 - 4). Several years ago Nicole Harris recorded direct fluorescence spectra of CaCl in the energy region 38 000 - 43 000 cm^{-1} (n* = 3 - 5) and found only isolated fragments of Rydberg states [16]. One $^2\Sigma^+$ state, n* = 3.75, was observed through fluorescence from the $v = 1$ vibrational level exclusively. Attempts to observe fluorescence from the $v = 0$ and $v = 2$ levels were unsuccessful. The presently derived position of the repulsive potential curve shown in Fig. 5-2 offers an explanation for this behavior in that the repulsive curve passes very close to the single node of the $v = 1$ wavefunction for the n* = 3.75 state. If the overlap between the repulsive and bound state gets very small, as one would expect for a repulsive curve which crosses near the $v = 1$ node (as shown in Fig. 5-2), the predissociation rate will pass through a minimum and the fluorescence quantum yield should recover sufficiently to allow detection via the fluorescence channel.

To explore this idea further, Fig. 5-4 shows the FCD as a function of n* and N of the bound Rydberg state evaluated at a fixed value of the C_{12} parameter, which in this case represents the lower confidence limit of our derived repulsive curve. From

Table 5.1: Calculated Franck-Condon Density (FCD), fluorescence quantum yield, and predicted linewidth for two low n* $^2\Sigma^+$ states.

	v	FCD$\times 10^6$	quantum yield[3]$\Phi_f \times 10^6$	Γ_{nr} (cm^{-1})[4]
n*=3.75[1]	0	217	5	15
	1	0	3475	0.02
	2	101	11	7
n*=3.16[2]	0	1	668	0.09
	1	22	23	3
	2	134	4	16

[1] Computed at C_{12} value of 2.061×10^8 cm^{-1} Å^{12}.
[2] Computed at C_{12} value of 2.573×10^8 cm^{-1} Å^{12}.
[3] Defined via fluorescence, $\Phi_f = \tau/\tau_r$ (see text).
[4] Predicted via Eq. 5.6.

Table 5.2: Calculated and predicted values of the electronic matrix element H^e for various $^2\Sigma^+$ Rydberg states, which belong to two Rydberg series (0.49 $^2\Sigma^+$ (X terminus) and 0.75 $^2\Sigma^+$ (B terminus).)

n*	7.49[1]	6.49[1]	7.75[1]	6.75[1]	5.75[1]	3.75[2]
H^e (cm^{-1})	40 (2)	46 (7)	47 (6)	45 (7)	49 (6)	105
$H^e \times n*^{-3/2}$ (cm^{-1})	820 (40)	760 (120)	1014 (130)	789 (120)	670 (80)	762

[1] Experimentally derived (1σ) in parentheses.
[2] Predicted using n*$^{-3/2}$ scaling.

the figure it is clear that a state in this region would have a FCD between two and five orders of magnitude smaller than a typically "large" overlap (O 10^{-4}). We can estimate the magnitude that this effect would have on the fluorescence quantum yield Φ_f in a relatively straightforward manner. Since only the total decay rate $1/\tau$ of a level can be measured, τ is related to the rate of decay of excited CaCl molecules via both radiative and nonradiative routes. If we let k_r be the radiative rate constant (the probability per unit time that a molecule will leave the level as a result of emission of a photon) and k_{nr} the predissociation rate (the dissociation probability per unit time), we can write in the zero collision limit [56]

$$1/\tau = k_r + k_{nr} = 1/\tau_r + 1/\tau_{nr}. \tag{5.10}$$

As is common for predissociation, $\tau_{nr} << \tau_r$, and the experimental linewidth Γ is dominated by Γ_{nr} and is related to τ_{nr} by

$$\Gamma_{nr}(cm^{-1}) = 5.3 \times 10^{-12}/\tau_{nr}(s). \tag{5.11}$$

By combining Eq. 5.10 with Eq. (5.6) we find a relation between τ_{nr} and the FCD:

$$\tau_{nr} = 8.4 \times 10^{-13}/(|H^e|^2 \, |\langle \chi_{v,J}(R) \mid \chi_{E,J}(R) \rangle|^2). \tag{5.12}$$

If the fluorescence quantum yield is defined as

$$\Phi_f = \tau/\tau_r \tag{5.13}$$

only a plausible estimate for τ_r is necessary for us to estimate how Φ_f varies with the FCD, as all other quantities can be measured or directly calculated. Dagdigian *et al.* determined τ_r for several CaCl valence electronic states, of which one, B $^2\Sigma^+$ (n* $\sim$ 2.86, $\tau = 38$ ns), is the series terminus for the n* = 3.75 state presently under discussion [61]. By using the intraseries scaling factor for transition probabilities $(v^3 n^{*3})$, we estimate τ_r for the n* = 3.75 state to be 6.6×10^{-8} s, see Footnote 3.

The bottom half of Fig. 5-4 shows the result of evaluating Eqs. 5.9,5.10,5.11,5.12 with the same FCDs used to generate the top half of the figure as well as the appropriate values of Γ and H^e (where H^e was estimated by scaling the experimentally derived value at n*=6.49 by n*$^{(-3/2)}$) [2]. We note that in the region with the smallest FCD (i.e. near the v=1 node) Φ_f reaches a maximum of 97%. Table 5.3 shows the FCD, Φ_f, and Γ_{nr} for the n*=3.75 state calculated with N=0 at the lower limit of the confidence range ($C_{12} = 2.061 \times 10^8$ Å^{12} cm^{-1}) of the repulsive state. A question that arises from this analysis is just how fortunate an observer would have to be to see fluorescence from a Rydberg state in this region. The uncertainty in the experimentally observed energy of the observed Rydberg state is just a few thousandths of a unit in n*, while the uncertainty in the actual position of the repulsive curve is much larger. The fluorescence quantum yields shown in Fig. 5-4 imply a rather small window of fluorescence detectability in terms of n* and N. More sensitive experiments in this region should be able to capture the sharp N dependence of predissociation caused by the accidental crossing of the repulsive state with a node in the bound state wavefunction. Calculations do not indicate the presence of a similar fluorescence channel at larger values of C_{12}, presumably because a more strongly repulsive curve would miss the node of the Rydberg $v = 1$ wavefunction (at least not until considerably higher-n* values).

Another group of direct-fluorescence observations provides indirect support for the presently determined position of the repulsive curve. Levels assigned to $N = 10$ and 22 of $v = 0$ and 1 for the n* $= 3.16$ $^2\Sigma^+$ state were observed around $\sim$38 000 cm^{-1}, and are also shown in Fig. 5-2 [16]. The observation of fluorescence only from $v = 0$ and 1 of the n* $= 3.16$ $^2\Sigma^+$ state is consistent with the intersection of the repulsive state occurring just above the $v = 1$ level, which implies low FCDs (and high Φ_f) for $v = 0$ and 1 relative to $v \geq 2$ levels. FCDs and values of Φ_f, computed at the upper limit of the confidence range ($C_{12} = 2.573 \times 10^8 \mathring{A}^{12}$ cm^{-1}) for the interaction of the repulsive state with the n* $= 3.16$ Rydberg state (see Table 5.3), show that

---

[2]As a radial matrix element, H^e is expected to scale as $n^{*(-3/2)}$ due to its dependence on the amplitude of the innermost lobe of the Rydberg wavefunction.

explanation is plausible for $v = 0$, which has an FCD ~ 130 times smaller (hence a Φ_f ~ 150 times larger) than for $v = 2$. The value of Φ_f for the $v = 1$ level, however, is not dramatically different than that for $v = 2$.

This discrepancy with respect to the too small predicted Φ_f value for $v = 1$ is of greater concern and suggests that the position of the repulsive state in this energy region should be somewhat to the right of the upper limit of the confidence range, which was derived from linewidth measurements for higher energy ($n^* \sim 6$) Rydberg states.

The number and variety of observations which sample the location of the repulsive $^2\Sigma^+$ potential curve may suggest a deficiency with a one-parameter representation, i.e. the optimum representation is near the lower confidence limit for $n^* = 3.75$, but just outside the upper limit for $n^* = 3.16$. However, what must be remembered is that the confidence ranges are based on quantitative measurements only in the energy range sampled in the ion-dip experiment ($\sim 46\ 100$ - $47\ 200$ cm^{-1}), and it is remarkable that the $^2\Sigma^+$ potential appears to be qualitatively valid at lower energy. As for the confidence range itself, it could be narrowed considerably by using a technique with inherently higher signal-to-noise than the ion-dip scheme, such as REMPI-TOF. Unfortunately REMPI-TOF data often suffers from the effects of power-broadening, and such was the case with REMPI-TOF spectra recently collected in the same region [22]. While the superior S/N of the REMPI-TOF data allowed refinement of the Rydberg state energies, the linewidths were usually 15% broader than in the ion-dip spectra and were therefore not used in the linewidth analysis. Considering the quality of the experimental data presently at hand, we do not believe use of a multiparameter model is justified.

The lack of N,J-dependence in the measured linewidths strongly suggests that the symmetry of the dissociating state is $^2\Sigma^+$, as matrix elements governing the interaction with a $^2\Pi$ state are strongly N,J-dependent.[13] The $^2\Sigma^+ \sim {}^2\Sigma^+$ interaction is also consistent with consideration of the possible σ or π orientation of the $3p$ electron hole on the Cl$^-$, which can be oriented in the direction of the Ca$^+$ to form a sigma hole (σ^{-1}) $^2\Sigma^+$ state or perpendicular to the Ca$^+$Cl bond axis to form a pi-hole (π^{-1})
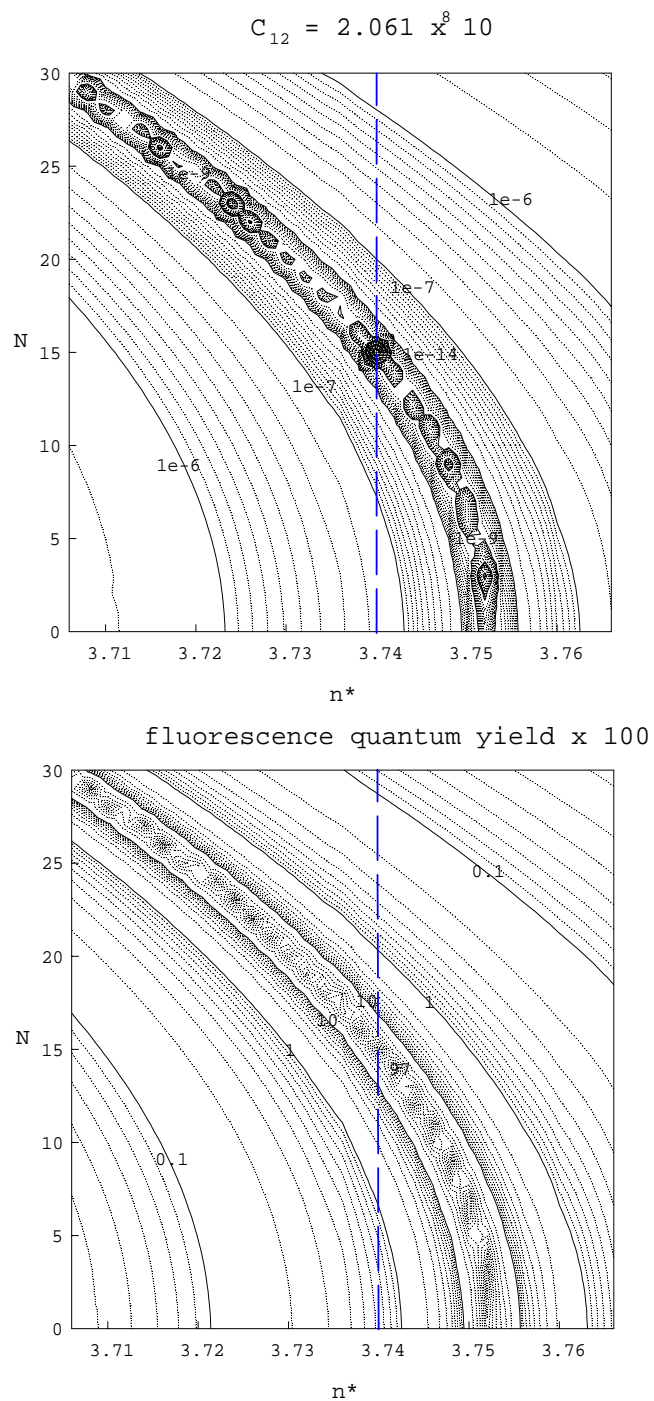
Figure 5-4: Franck-Condon Density (top) and fluorescence quantum yield (bottom) versus N and n* computed at the left confidence limit of the repulsive state location ($C_{12} = 2.061 \times 10^8$ Å^{12} cm^{-1}).

147

$^2\Sigma^+$
(σ-hole)

pπ

Ca^+ pσ Cl^-

$^2\Pi$
(π-hole)

pπ

Ca^+ pσ Cl^-
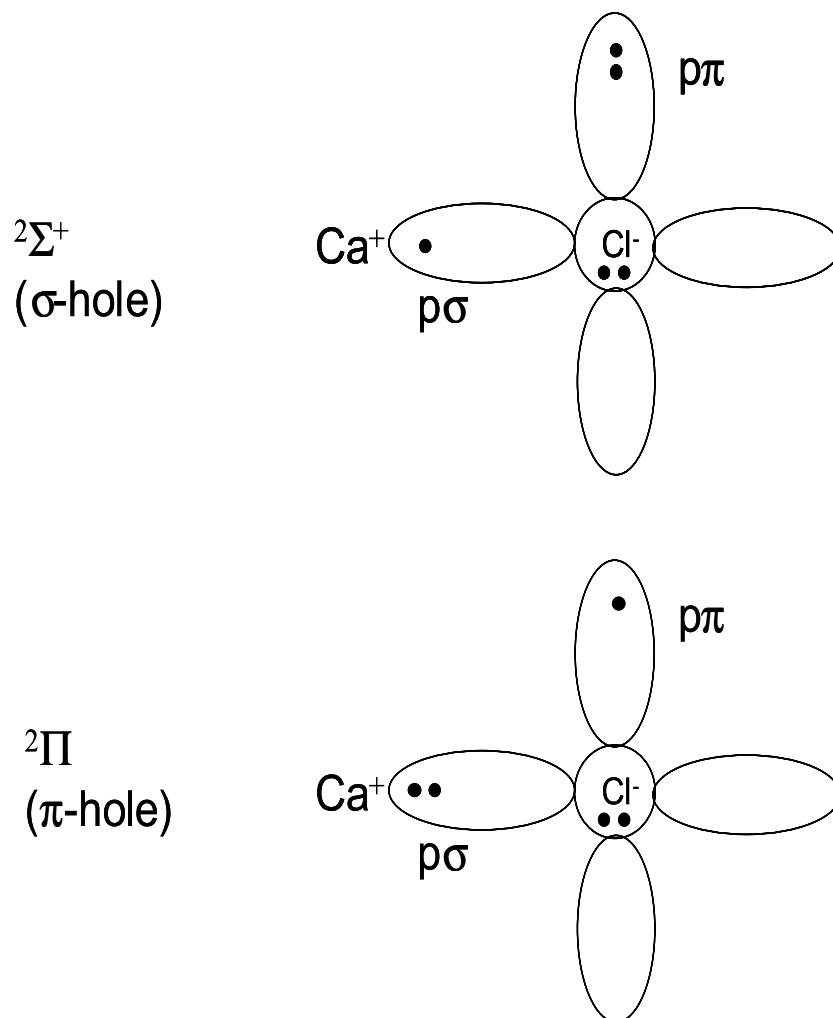
Figure 5-5: Molecular orbital representation of $3p\pi^{-1}$ and $3p\sigma^{-1}$ hole configurations of CaCl giving rise to $^2\Pi$ and $^2\Sigma^+$ repulsive states which dissociate to $M(^1S)$ + X (^2P) neutral atoms. The $^2\Pi$ repulsive state is expected to be more repulsive than the $^2\Sigma^+$ repulsive state in the n* = (3 - 8) region since the electron density pointing toward Ca $4s^2$ is larger for the π^{-1} configuration and "overlap repulsion" of two electrons in F centered pσ orbitals with the filled Ca $4s^2$ shell is 2× as large as that for the single F^- pσ electron for the σ^{-1} states.

$^2\Pi$ state (see Fig. 5-5. It is reasonable to expect that in the Rydberg energy region, the π^{-1} state would be more repulsive (i.e., the repulsive potential curve would lie at large R_e) than the σ^{-1} state, due to the fact that the π^{-1} state has two electrons in $p\sigma$ orbitals pointed directly toward the closed-shell electron density of the Ca^+ rather than only a single electron in the case of the σ^{-1} state. Thus the π^{-1} $^2\Pi$ repulsive state would be expected to miss the low n* (and low-v) manifold of all Rydberg states converging to the X $^1\Sigma^+$ state of $CaCl^+$.

With the position of the $^2\Sigma^+$ repulsive curve on a firm footing, the subsequent use of Eq. 5.7 allows the determination of the interaction matrix element H^e (see Table 5.3). Since matrix elements involving Rydberg wavefunctions are largely dependent on the intra-core amplitude, which has a scaling factor of n*$^{-3/2}$, multiplying the values of H^e by n*$^{3/2}$ effectively removes the energy dependence (n*) in the matrix element[3]. Examination of Table 5.3 shows that the descaled values of H^e for two $^2\Sigma^+$ Rydberg series are similar. The most significant implication of this result is the validity of the inverse operation, that by multiplying H^e by n*$^{-3/2}$, the experimentally determined matrix element can be scaled to any desired energy.

It had been expected that the fractional s, p, and d characters of the Rydberg wavefunctions (as constructed from Ca^+ atomic basis states) would be sufficiently different among the three $^2\Sigma^+$ Rydberg series to have an effect on H^e; however, examination of Table 5.3 shows no obvious differences in the descaled H^e values.

5.4 Conclusion

Using linewidths from ion-dip spectra involving the $v = 0$, 1, and 2 levels of members of two Rydberg $^2\Sigma^+$ series (n* = 6 - 8), the n*-reduced values of the e^2/r_{12} interaction matrix element were determined and the position of the repulsive potential state

---

[3]The Einstein A coefficient is proportional to $\nu^3 |\langle n'l' |r| nl\rangle|^2$, where ν is frequency and $|\langle n'l' |r| nl\rangle|^2$ is a radial (transition moment) matrix element. Most matrix elements that involve Rydberg states are dominated by the innermost lobe of the Rydberg wavefunction, the amplitude of which scales as n*$^{-3/2}$. Therefore the A coefficient for transitions to a common lower state (e.g. the X $^2\Sigma^+$ state) is expected to scale as $\nu^3 n^{*-3}$.

was located and assigned as due to the $3p\sigma$-hole $^2\Sigma^+$ state. The position of the derived repulsive curve at lower energy (n* = 3 - 4) was shown to be qualitatively consistent with previously unexplained direct-fluorescence observations. In order to completely characterize the Rydberg $^2\Sigma^+$ predissociation dynamics in CaCl, future work is necessary and would include further fluorescence and ion-dip studies in the (n* = 3-7) range as well as Multichannel Quantum Defect Theory (MQDT) treatments of Rydberg-valence interactions.

5.5 Acknowledgement

Chapter 6

OODR experiments in the n* = 15 - 20 region

6.1 Introduction

As was discussed in Chapter 4, the observation of Rydberg states by ionization in the low-n* region is hampered by the onset of predissociation, leading to the observation of only a handful of states with high (0.02 cm^{-1}) resolution in the n* = (5 - 7) region. The $^2\Sigma^+$ predissociation is expected to turn off as n*$\to \infty$, as the repulsive curve moves through the manifold of $^2\Sigma^+$ Rydberg states to smaller r_e, while the $^2\Pi$ predissociation is expected affect $^2\Pi$ Rydberg states throughout the Rydberg manifold (see Fig. 3-1). This expectation has been borne out by observations of a large number of $^2\Sigma^+$ states above the $v^+ = 0$ IP (n* = 15 - 20), in the 'autoionizing' region. Autoionization is a type of interaction between an excited neutral molecule state and the continuum of an ionized molecule:

$$\text{CaCl} + hv \longrightarrow \text{CaCl}^{**} \longrightarrow \text{CaCl}^+ + e^-. \tag{6.1}$$

Autoionization was called "preionization" by Herzberg, who compared it to pre-dissociation by noting that while predissociation is the interaction of a discrete state with a vibrational continuum, autoionization is the mixing of a discrete state with

the electronic continuum of the ion [56]. Autoionization can occur for Rydberg states anywhere above the first ionization threshold (48 491 cm^{-1} for CaCl $v = 0$), and can also lead to line broadening for the autoionizing resonances. Autoionizing states are relatively easy to produce and detect in the laboratory, and with the density of states increasing as n^2 in the Rydberg manifold, a relatively short laser scan can sweep through a large range of Rydberg series.

6.2   Experimental Details

The experimental details for this experiment were almost identical to those described in Chapter 4 for OODR in the low-n* region. Individual N levels (4-15) of the R-branch of the $D\,^2\Sigma^+ v = 1$ level were used as intermediate states. The probe laser was scanned with Rhodamine 101 dye over the 580 - 590 nm range, covering n* = 15 - 20 (see Fig. 6-1). Laser pulse energies for the pump and probe steps were $\approx$100 μJ/pulse and $\approx$50 - 200 μJ/pulse, respectively. Very low probe laser powers are necessary to achieve an adequate signal/noise ratio as compared with other experiments described in this thesis. Indeed, the necessary power level was often reached without using the amplifier stage of the dye laser. Careful pump/probe beam alignment is necessary for optimal signal acquistion, but this can be easily achieved by using the probe laser at high power (>1 mJ/pulse) and manually tuning its output until a resonance is seen. The pump/probe laser power can then be titrated to allow maximum autoionization signal with a minimum of background nonresonant multiphoton ionization signal. The HV pulser circuit described in Chapter 2 was employed for these experiments to allow laser excitation to take place in the absence of an electric field, and was timed to occur some 100 ns after the 5-ns long laser pulse. An I$_2$ fluorescence excitation spectrum was simultaneously captured with the TOF/MS signal, allowing probe laser calibration through visible and near-IR region.
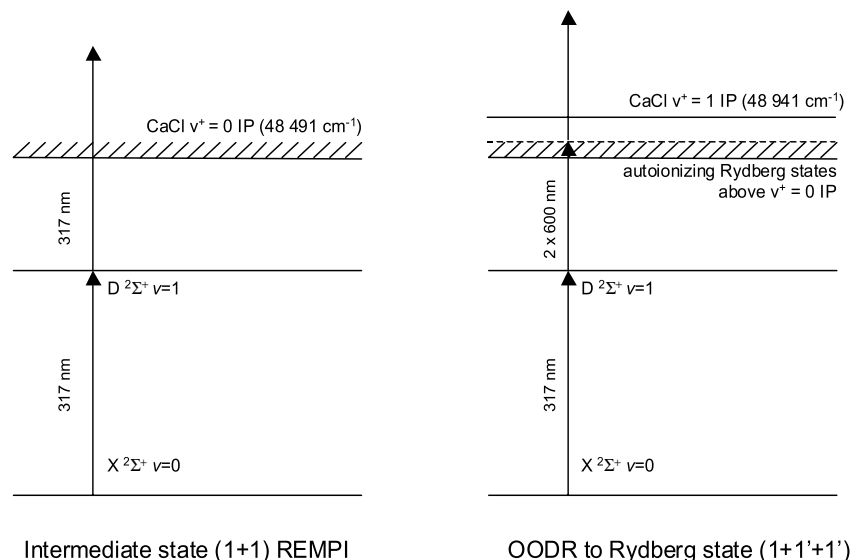
Figure 6-1: Energy level diagram for the $D\ ^2\Sigma^+$ - $X\ ^2\Sigma^+$ (1,0) transition of CaCl and OODR pump-probe scheme for reaching Rydberg state levels in the autoionizing region above the $v^+ = 0$ IP. Absorption of a second photon can also occur if the autoionizion rate is slow.

6.3 Results and Discussion

The spectra in this region have a much greater line density than any other region yet explored. One of the striking features of the spectra is the abrupt 'turn-on' of the features above the first ionization limit. No Rydberg series convergence was seen at the $v^+ = 0$ ionization limit (48 491 cm^{-1}), which was initially a surprising finding. This can be partly explained by the highly diagonal ($\Delta v = 0$) FCFs for the $D\ ^2\Sigma^+$ state $v = 1$ - Rydberg transition (see Fig. 4-3). This $\Delta v = 0$ propensity is actually beneficial in a congested spectral region, since we *a priori* know that most of the states seen in the ionizing region correspond to $v^+ = 1$. All of the states assigned so far are $^2\Sigma^+$ states belonging to the 0.49 and 0.75 series. No $^2\Pi$ states have been assigned in this region, which indicates the $^2\Pi \sim ^2\Pi$ predissociation mechanism discussed in previous chapters must still be in effect, with the predicted position of

153
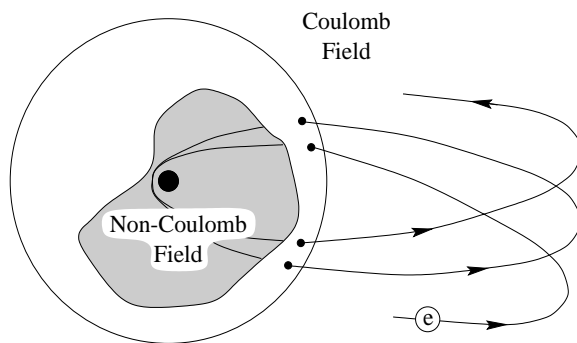
Figure 6-2: Representation of non-hydrogenic ion-core. MQDT treats Rydberg electron - ion core interaction as a scattering problem which is related to a phase differential for the entering and exiting wavefunction. (courtesy of Dr. Sergey Panov)

the $^2\Pi$ repulsive curve affecting the entire $^2\Pi$ Rydberg state manifold (see Fig. 3-9). By contrast, the predicted position of the $^2\Sigma^+$ repulsive curve suggests that it will pass through the Rydberg state manifold at a moderate n* (see Fig. 5-2), allowing recovery of ionization quantum yield for $v \geq 1$. The lack of observation of $v = 0$ series below the first IP suggests that predissociation also plays a role, since $v = 0$ levels, having wavefunction density localized at shorter R_e, are likely to be affected by the predissociation over a larger n* range than higher v states with wavefunction density at larger R_e (i.e., the outer turning point).

6.3.1   Single-state Fits

The $^2\Sigma^+$ states in the n* = 15 - 20 region displayed a prominent two-line P-R branch pattern. A case (b) Hamiltonian was used to find the values for T_v and B_v in the same fashion as that described in Chapter 4 for lower n* data. The results from those fits are summarized in Table 6.3. The most surprising finding is a systematically lower value ($\sim 5\%$) of B_v between the two $^2\Sigma^+$ series. These values of B_v agree well with the previously determined value of B_v^+ (0.164 cm^{-1}) determined from work in the n* = 6 - 7 region [22], although the ones presented here are more precise.

The line positions (and fitting errors) for observed transitions are tabulated throughout the rest of the chapter.
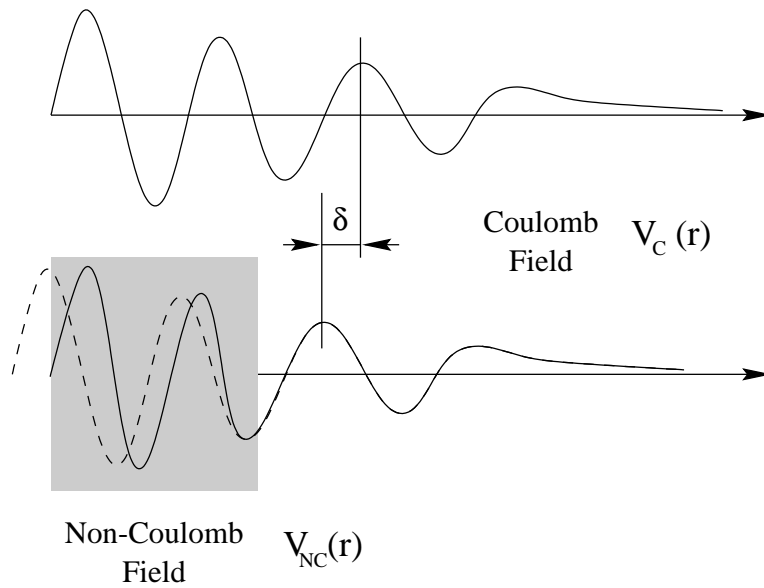
Figure 6-3: Representation of the phase differential for Rydberg wavefunction in a Coulombic and non-Coulombic field. (courtesy of Dr. Sergey Panov)

6.3.2 MQDT fitting

Multichannel Quantum Defect Theory (MQDT) is a powerful theoretical tool that has recently proven quite useful in describing the Rydberg spectra of CaF [62]. The application of MQDT to the alkaline earth monohalides represents the fruit of an extensive collaboration with Prof. Christian Jungen and his group at CNRS in Orsay, France [5,12,49,63]. Their work has not only provided *ab initio* values for the quantum defects of all Rydberg series [5, 63], but also allows fitting of the experimentally observed states to quantum defect parameters [62], which can be compared to the previously determined *ab initio* values.

A large data set acquired by Dr. Chris Gittins for CaF was analyzed using MQDT [21, 62]. The MQDT fitting procedure used 491 rovibronic levels of CaF observed through a similar experiment to the one presently described for CaCl. The quantum defect parameters determined in the CaF analysis were used as a starting point for MQDT fits of the $^2\Sigma^+$ data for CaCl presented here.

The theory of MQDT is extensively reviewed in other works, so only a summary

will be presented here [62,64]. The most important idea in MQDT is that the molecular wavefunction needs to have a different representation depending on its proximity to the ion-core. Often, it is convenient to define two regions (I and II), where region I defines the region of ion-core interaction and region II is everywhere beyond the limit of ion-core interaction. In region I the motion of the Rydberg electron is characterized by Λ (the orbital angular momentum projection along the internuclear axis) and R (the internuclear distance) [8]. In such a region, we can write the wavefunction as:

$$\Psi_{\Lambda R}^{I} = X_{\Lambda R}^{core}[f_v cos\pi\mu_\Lambda(R) - g_v sin\pi\mu_\Lambda R], \tag{6.2}$$

where f is a regular Coulomb function and g is the irregular Coulomb function which lags f by 90 degrees [8]. This construction is useful since the electron emerges from the ion-core with a phase shift of $\pi\mu_\Lambda(R)$ relative to the Coulombic region (see Figs. 6-3 and 6-2). This phase shift for molecular-core interaction is encoded in each $\mu_\Lambda(R)$, and represents the difference between an electron experiencing a complicated potential from a multi-electron core vs. the simple one of a single proton in the case of the Hydrogen atom.

Outside the core in region II we can write the wavefunction as

$$\Psi_{N+,l+}^{I} = \Phi_{N+,l+}^{ion}[f_{\nu N+l+} cos\pi\mu_{N+l+} - g_{\nu N+l+} sin\pi\mu_{N+l+}] \tag{6.3}$$

where the quantum defect functions are the ones coupling the Rydberg electron to the ionic dissociation channels [8]. The molecular wavefunctions for regions I and II can be related in terms of coefficients which effectively joins the two regions:

$$\Psi = \sum_\Lambda \int dR \ A_\Lambda(R)\Psi_{\Lambda R}^{A} = \sum_{N+l+} B_{N+l+}\Psi_{N+l+}^{B}, \tag{6.4}$$

where A and B refer to functions in regions I and II, respectively. Since in region I the Coulomb energy is large compared to the rotational and vibrational quanta, the f and g functions for different channels differ only slightly, allowing the derivation of the following linear system:

$$\sum_{N^{+\prime}l^{\prime}} [sin\pi\nu_{N+l+}C_{N+l+,N^{+\prime}l^{\prime}+\prime} + cos\pi\nu_{N+l+}S_{N+l+,N^{+\prime}l^{\prime}+\prime}]B_{N^{+\prime}l^{\prime}+\prime}, \tag{6.5}$$

where $B_{N^{+\prime}l^{\prime}+\prime}$ are channel mixing amplitudes which give the decomposition of each eigenstate in terms of the channels l and N^+ [62]. The C and S matrices are symmetric, nondiagonal in l and N^+, which take into account the short-range inelastic scattering of the Rydberg electron by the ion-core [62]. These matrices are related to the quantum defect matrix by

$$\mu = \pi^{-1}arctan(SC^{-1}) \tag{6.6}$$

The C matrix contains the necessary frame transformation elements which relate the space-fixed coordinate frame (i.e. Hund's case (d)) to the molecular-fixed one (Hund's case (b)). The frame transformation elements are essentially Clebsch-Gordon coefficients. The linear system of Eq. 6.5 has solutions at values ν_{N+l+} which should correspond to observed lines in the spectrum. The coefficients $B_{N^{+\prime}l^{\prime}+\prime}$ then describe the relative intensities of the observed lines [8]. In practice, the equations are solved in an iterative fashion based on reasonable initial values for the quantum defect parameters. This is a highly non-linear fitting procedure and can be quite time-intensive. Nevertheless, MQDT's ability to encapsulate the entire spectrum in a handful of quantum defects is remarkable, and it had great success in the application for CaF, representing the entire 491 line data set with a deviation of 0.68 cm^{-1}.

The current MQDT fit results must be considered preliminary. They are summarized in Table 6.3.2, while the residuals and data subset used is listed in Table 6.2. The deviation in the fit currently is 1.07 cm^{-1}, but it is expected that this could be lowered significantly with additional effort. The results within each series show systematic deviations with increasing N, which suggests that B_v^+ for the ion should be unclamped. After a fit variance of approximately 0.5 is obtained, the remainder of the data for the n*= 15 - 20 $^2\Sigma^+$ states will be entered into the fit.

Table 6.1: MQDT parameters determined from fitting process, with standard deviation in parentheses.

Parameter	Value and uncertainty (cm^{-1})
$CaCl^+$ $v = 0$ (IP)	48493.67 (7)
ss $^2\Sigma^+$	0.501 (10)
B_v^+	0.1669 (fixed)
ω_e	450 (fixed)
$\omega_e x_e$	1.5 (fixed)

6.4   Conclusion

The autoionization region is a fruitful one for quickly recording relatively large amounts of Rydberg state data. In the case of CaCl, the predissociation interaction for $^2\Pi$ states described in previous chapters prevented their detection by ionization methods employed here. In CaF, $^2\Sigma^+$, $^2\Pi$, and $^2\Delta$ states were observed [21].

Eight $^2\Sigma^+$ states assigned to the 0.49 and 0.75 Rydberg series of CaCl were recorded in the n* range 15 - 20. All of these data were fit to a case (b) Hamiltonian, while a subset was fit using an MQDT model. The goals of each type of fitting are complementary yet distinct; while the goal of the effective Hamiltonian approach long used by our group is to find the molecular constants and perturbation parameters which describe a set of molecular transitions, the goal of an MQDT fit is to refine the values of the quantum defects and the values for the ionization limits of the $CaCl^+$ ion. Effective Hamiltonian modelling allows a quick detection of perturbed lines, which is used to refine an MQDT fit for a particular series. Both approaches yield insight into the spectroscopy and dynamics of Rydberg molecules, and one is not sufficient without the other.

Table 6.2: Results of MQDT fits for n* = 15-16 $^2\Sigma^+$ $v = 1$ OODR data.

level (cm^{-1})	N value	observed - calculated (cm^{-1})
n* = 15.49 $^2\Sigma^+$ data		
48484.12	4	-1.7
48487.82	6	-1.02
48490.14	7	-0.70
49492.92	8	-0.35
48495.75	9	-0.09
48499.13	10	0.28
48502.78	11	0.59
48506.80	12	0.94
48511.13	13	1.26
48515.82	14	1.61
48520.93	15	2.05
n* = 15.75 $^2\Sigma^+$ data		
48498.75	4	-1.48
48500.52	5	-1.04
48502.28	6	-0.94
48504.63	7	-0.58
48507.15	8	-0.38
48510.06	9	-0.13
48512.95	10	-0.22
48516.63	11	0.15
48520.40	12	0.27
48524.64	13	0.54
48529.27	14	0.86
n* = 16.49 $^2\Sigma^+$ data		
48537.76	4	-1.78
48539.47	5	-1.40
48541.44	6	-1.10
48543.79	7	-0.75
48546.47	8	-0.48
48549.42	9	-0.13
48552.78	10	0.23
48556.50	11	0.61
48560.52	12	0.96
48564.91	13	1.34
48569.82	14	1.91
48574.89	15	2.31

Table 6.3: Results of least squares fits for n* = 15-18 $^2\Sigma^+$ $v = 1$ OODR data. (1-σ) error in parentheses.

State (n*,v)	T_v (cm^{-1})	B_v (cm^{-1})	$\gamma_{sr,v}$ (cm^{-1})
15.49 $^2\Sigma^+$ $v = 1$	48480.77 (2)	0.1670 (1)	1.3×10^6 (fixed)
16.49 $^2\Sigma^+$ $v = 1$	48534.33 (3)	0.1685 (2)	1.3×10^6 (fixed)
17.49 $^2\Sigma^+$ $v = 1$	48579.34 (3)	0.1686 (3)	1.3×10^6 (fixed)
18.49 $^2\Sigma^+$ $v = 1$	48617.15 (3)	0.1705 (6)	1.3×10^6 (fixed)
15.75 $^2\Sigma^+$ $v = 1$	48495.63 (3)	0.1596 (2)	1.3×10^6 (fixed)
16.75 $^2\Sigma^+$ $v = 1$	48546.70 (1)	0.1585 (2)	1.3×10^6 (fixed)
17.75 $^2\Sigma^+$ $v = 1$	48588.53 (4)	0.1605 (9)	1.3×10^6 (fixed)
18.75 $^2\Sigma^+$ $v = 1$	48625.97 (2)	0.1553 (2)	1.3×10^6 (fixed)
11.49 $^2\Sigma^+$ $v = 2$	48556.29 (1)	0.1660 (1)	1.3×10^6 (fixed)

Table 6.4: OODR from D (1,0) band. Assignment is n*=15.49 $^2\Sigma^+$ $v = 1$. All energies in cm^{-1} and referenced to X $^2\Sigma^+$ $v = 0$, $N = 0$. Quantity in parentheses is observed-calculated from least squares fit in terms of the last digit.

J	F_{1e}	F_{2f}
3.5	-	48484.12 (1)
4.5	48484.12 (1)	-
5.5	-	48487.82 (4)
6.5	48487.82 (4)	48490.14 (2)
7.5	48490.14 (2)	48492.82 (3)
8.5	48492.82 (3)	48495.75 (-5)
9.5	48495.75 (-5)	48499.13 (-1)
10.5	48499.13 (-1)	48502.78 (-3)
11.5	48502.78 (-3)	48506.80 (-2)
12.5	48506.80 (-2)	48511.13 (-3)
13.5	48511.13 (-3)	48515.82 (-2)
14.5	48515.82 (-2)	48520.93 (8)
15.5	48520.93 (8)	-

Table 6.5: OODR from D (1,0) band. Assignment is n*=15.75 $^2\Sigma^+$ $v = 1$. All energies in cm^{-1} and referenced to X $^2\Sigma^+$ $v = 0$, $N = 0$. Quantity in parentheses is observed-calculated from least squares fit in terms of the last digit.

J	F_{1e}	F_{2f}
3.5	-	48498.75 (-8)
4.5	48498.75 (-8)	48500.52 (9)
5.5	48500.52 (9)	48502.28 (-6)
6.5	48502.28 (-6)	48504.63 (6)
7.5	48504.63 (6)	48507.15 (3)
8.5	48507.15 (3)	48510.06 (6)
9.5	48510.06 (6)	48512.95 (-24)
10.5	48512.95 (-24)	48516.63 (-7)
11.5	48516.63 (-7)	48520.40 (-12)
12.5	48520.40 (-12)	48524.64 (-4)
13.5	48524.64 (-4)	48529.27 (12)
14.5	48529.27 (12)	-

Table 6.6: OODR from D (1,0) band. Assignment is n*=16.49 $^2\Sigma^+$ $v = 1$. All energies in cm^{-1} and referenced to X $^2\Sigma^+$ $v = 0$, $N = 0$. Quantity in parentheses is observed-calculated from least squares fit in terms of the last digit.

J	F_{1e}	F_{2f}
3.5	-	48537.76 (6)
4.5	48537.76 (6)	48539.47 (8)
5.5	48539.47 (8)	48541.44 (3)
6.5	48541.44 (3)	48543.79 (2)
7.5	48543.79 (2)	48546.47 (0)
8.5	48546.47 (0)	48549.42 (-8)
9.5	48549.42 (-8)	48552.78 (-8)
10.5	48552.78 (-8)	48556.50 (-8)
11.5	48556.50 (-8)	48560.52 (-10)
12.5	48560.52 (-10)	48564.91 (-9)
13.5	48564.91 (-9)	48569.82 (11)
14.5	48569.82 (11)	48574.89 (12)
15.5	48574.89 (12)	-

Table 6.7: OODR from D (1,0) band. Assignment is n*=16.75 $^2\Sigma^+$ $v = 1$. All energies in cm^{-1} and referenced to X $^2\Sigma^+$ $v = 0$, $N = 0$. Quantity in parentheses is observed-calculated from least squares fit in terms of the last digit.

J	F_{1e}	F_{2f}
3.5	-	48549.88 (2)
4.5	48549.88 (2)	48551.48 (3)
5.5	48551.48 (3)	48553.34 (-1)
6.5	48553.34 (-1)	48555.56 (-1)
7.5	48555.56 (-1)	48558.07 (-4)
8.5	48558.07 (-4)	48560.93 (-3)
9.5	48560.93 (-3)	48564.16 (3)
10.5	48564.16 (3)	48567.66 (4)
11.5	48567.66 (4)	48571.41 (-2)
12.5	48571.41 (-2)	-

Table 6.8: OODR from D (1,0) band. Assignment is n*=17.49 $^2\Sigma^+$ $v = 1$. All energies in cm^{-1} and referenced to X $^2\Sigma^+$ $v = 0$, $N = 0$. Quantity in parentheses is observed-calculated from least squares fit in terms of the last digit.

J	F_{1e}	F_{2f}
3.5	-	48582.77 (6)
4.5	48582.77 (6)	48584.40 (1)
5.5	48584.40 (1)	48586.45 (3)
6.5	48586.45 (3)	48588.72 (-5)
7.5	48588.72 (-5)	48591.43 (-4)
8.5	48591.43 (-4)	48594.51 (0)
9.5	48594.51 (0)	48597.78 (-1)
10.5	48597.78 (-1)	48601.61 (2)
11.5	48601.61 (2)	48605.71 (7)
12.5	48605.71 (7)	-

Table 6.9: OODR from D (1,0) band. Assignment is n*=17.75 $^2\Sigma^+$ $v = 1$. All energies in cm^{-1} and referenced to X $^2\Sigma^+$ $v = 0$, $N = 0$. Quantity in parentheses is observed-calculated from least squares fit in terms of the last digit.

J	F_{1e}	F_{2f}
3.5	-	48591.73 (0)
4.5	48591.73 (0)	48593.34 (0)
5.5	48593.34 (0)	48595.32 (5)
6.5	48595.32 (5)	48597.43 (-9)
7.5	48597.43 (-9)	48600.12 (4)
8.5	48600.12 (4)	-

Table 6.10: OODR from D (1,0) band. Assignment is n*=18.49 $^2\Sigma^+$ $v = 1$. All energies in cm^{-1} and referenced to X $^2\Sigma^+$ $v = 0$, $N = 0$. Quantity in parentheses is observed-calculated from least squares fit in terms of the last digit.

J	F_{1e}	F_{2f}
3.5	-	48620.59 (3)
4.5	48620.59 (3)	48622.23 (-4)
5.5	48622.23 (-4)	48624.26 (-4)
6.5	48624.26 (-4)	48626.73 (6)
7.5	48626.73 (6)	-
8.5	-	48632.48 (-1)
9.5	48632.48 (-1)	-

Table 6.11: OODR from D (1,0) band. Assignment is n*=18.75 $^2\Sigma^+$ $v = 1$. All energies in cm^{-1} and referenced to X $^2\Sigma^+$ $v = 0$, $N = 0$. Quantity in parentheses is observed-calculated from least squares fit in terms of the last digit.

J	F_{1e}	F_{2f}
3.5	-	48629.06 (-1)
4.5	48629.06 (-1)	48630.59 (-3)
5.5	48630.59 (-3)	48632.47 (-2)
6.5	48632.47 (-2)	48634.66 (-1)
7.5	48634.66 (-1)	48637.22 (6)
8.5	48637.22 (6)	48639.95 (8)
9.5	48639.95 (8)	-
10.5	-	48646.43 (-2)
11.5	48646.43 (-2)	48650.18 (-1)
12.5	48650.18 (-1)	-

Table 6.12: OODR from D (1,0) band. Assignment is n*=11.49 $^2\Sigma^+$ $v = 2$. All energies in cm^{-1} and referenced to X $^2\Sigma^+$ $v = 0$, $N = 0$. Quantity in parentheses is observed-calculated from least squares fit in terms of the last digit.

J	F_{1e}	F_{2f}
3.5	-	48559.59 (-2)
4.5	48559.59 (-2)	48561.26 (-1)
5.5	48561.26 (-1)	48563.26 (0)
6.5	48563.26 (0)	48565.60 (2)
7.5	48565.60 (2)	48568.25 (1)
8.5	48568.25 (1)	48571.24 (1)
9.5	48571.24 (1)	48574.55 (0)
10.5	48574.55 (0)	48578.17 (-3))
11.5	48578.17 (-3)	48582.23 (5)
12.5	48582.23 (5)	48586.45 (-2)
13.5	48586.45 (-2)	48591.23 (9)
14.5	48591.23 (9)	48596.05 (-8)
15.5	48596.05 (-8)	-

Chapter 7

Conclusions

7.1 General Remarks

From the experimental and theoretical efforts described in this thesis, we have confirmed that the Rydberg spectrum of CaCl is very similar to that of its better-known homologue, CaF. The challenge for the acquisition of CaCl Rydberg spectra is the early onset of predissociation (n* $\sim$ 3). From the survey and OODR experiments carried out in this work we have determined the position of the $^2\Sigma^+$ state manifold in the n* = 3 - 7 and 15 - 20 regions. From a linewidth analysis of ion-dip spectra previously recorded in the n* = 6 - 7 region, the position of the $^2\Sigma^+$ repulsive curve responsible for the $^2\Sigma^+ \sim^2\Sigma^+$ predissociation was determined. Observations of $^2\Pi$ states in the survey spectra from the X $^2\Sigma^+$ ground state allowed a qualitative determination of the $^2\Pi$ state repulsive curve position which is responsible for the $^2\Pi \sim^2\Pi$ state predissociation. For CaCl the $^2\Pi$ states are particularly difficult to observe, as the position of the repulsive curve all but ensures low ionization quantum yield from n* = 5 $\longrightarrow \infty$. The dissimilarity between the low-n* OODR and survey scan experiments was rationalized by a kinetic argument that describes the competition between ionization and predissociation. It is now apparent that OODR experiments at low laser power are not sufficient for observation of predissociating levels, but OODR experiments in the autoionizing region above the $v^+ = 0$ ionization limit are quite successful in recording a large number of Rydberg states.

7.2 Current Work

Several projects are scheduled for near-term (Spring 2002) completion. Among these are the recording of OODR data from the $D\ ^2\Sigma^+$ intermediate state of calcium monofluoride (CaF) in its autoionizing region above the $v = 0$ ionization potential (46 998 cm^{-1}). The aims of this project are to compare the results of OODR data accessed via different intermediate states from both CaF and CaCl. D state data presently being recorded for CaF will allow a direct comparison to the spectra presented in the previous chapter for CaCl. It is expected that p-character $^2\Sigma^+$ and $^2\Pi$ states will be more prevalent in the CaF spectra due to the lack of any obvious predissociation mechanism for these states, since they have been observed previously by experiments accessing the A and $C\ ^2\Pi$ states [21].

A related experiment involves the $C\ ^2\Pi$ state of CaCl. This state, like its counterpart in CaF, is "reverse" polarized (see discussion in Section 3.3.2). Reverse-polarized states have dramatically different values of ω_e and the quantum defect derivative than the typical Rydberg state. Not only does this favor non-diagonal FCFs ($\Delta v \neq 0$), but its large partial d character also allows direct access to non-penetrating series, as was observed in CaF [21]. Experiments involving the C state of CaCl are complicated by a few technical details. As can be seen from the energy level diagram in Fig. 7-1, the pump laser requires 374 nm light, which is easily generated by BBO-doubled infrared dye (Pyridine 2 @ 748 nm). The probe laser, however, requires generation of 460 nm light (Coumarin 460) which will not absorb sufficient light to lase at the 532 pump wavelength necessary for the Pyridine 2. In this case, the Infinity Nd:YAG can be used to pump the Lambda Physik OPPO in order to produce the necessary wavelengths. There is no *a priori* reason not to expect to observe the same type of f-complex structures in CaCl as was previously seen in CaF [21], since any predissociation process will not affect higher l, Λ states than $^2\Pi$.

Another experiment involves the excitation of autoionizing $v = 1$ levels through the D state in the presence of an electric field. Spectra have already been recorded (though not yet completely analyzed) with a constant electric field of ~ 120 V/cm.
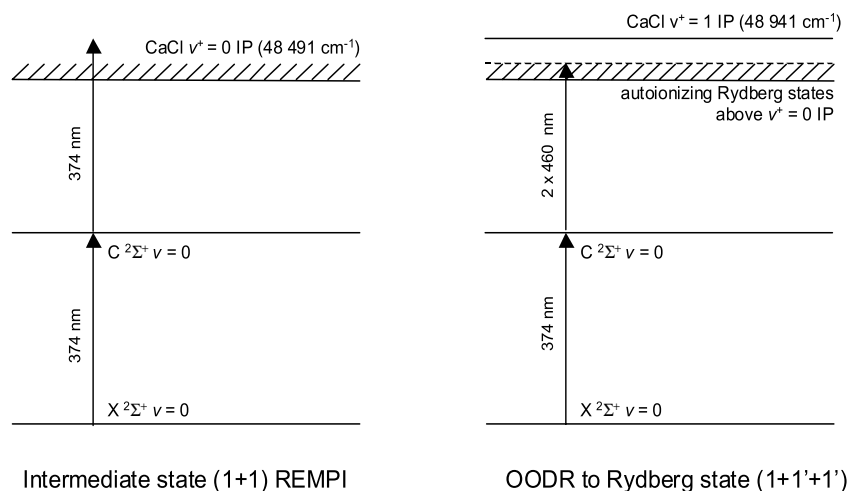
Figure 7-1: Energy level diagram for the $C\ ^2\Sigma^+$ - $X\ ^2\Sigma^+$ (0,0) transition of CaCl and OODR pump-probe scheme for reaching Rydberg state levels in the autoionizing region above the $v^+ = 0$ IP. Absorption of a second photon can also occur if the autoionizion rate is slow.

The resultant spectra show pronounced differences with spectra recorded at zero field (as described in Chapter 6). The presence of extra lines in the presence of an electric field shows that N mixing has been allowed to take place in the absence of parity. Several nominally parity-forbidden transitions are observed, allowing in some cases quite high signal.
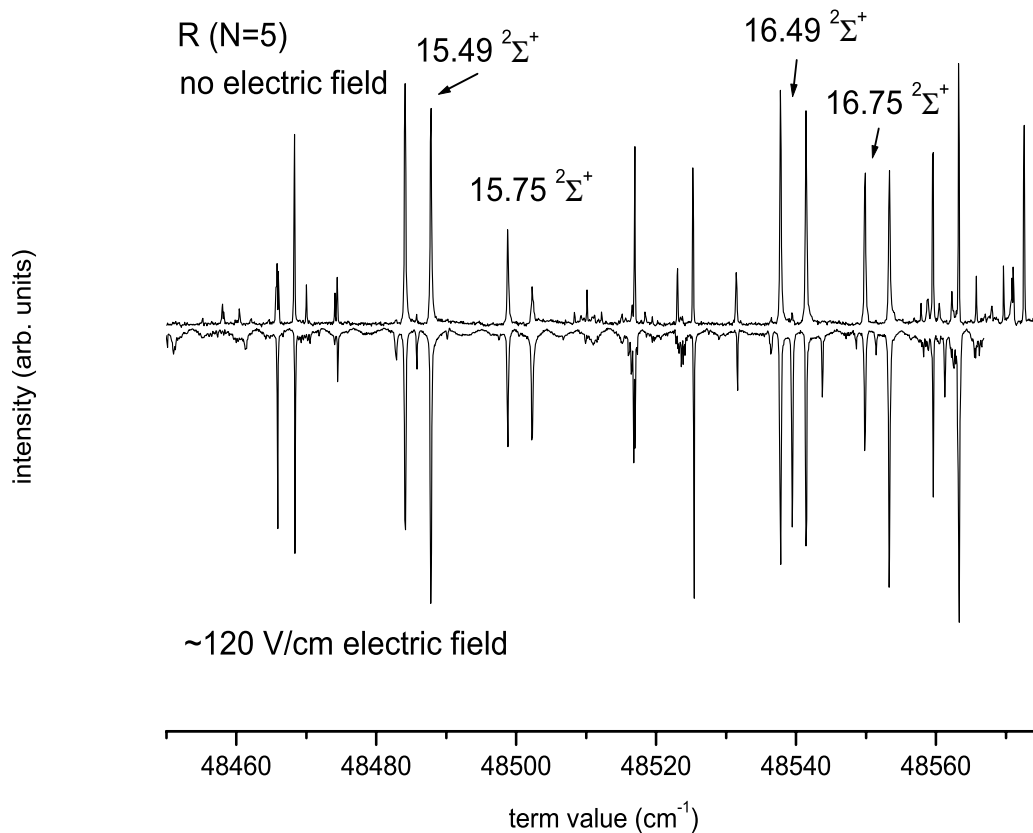
Figure 7-2: Spectra recorded in the autoionizing region of CaCl via the $D\ ^2\Sigma^+$ (1,0) $N = 5$ level. The top trace was recorded in the absence of a DC electric field, while the inverted bottom trace shows a spectrum of the same energy region recorded with a constant DC electric field of $\approx$120 V/cm. Nominally parity-forbidden transitions to Rydberg state $^2\Sigma^+$ state rotational levels are observed in the presence of the electric field.

Bibliography

[1] V. V. Technologies, *Product Catalog 2000* (Varian Vacuum Technologies, Lexington, Ma, 1999).

[2] NIST, *NIST Standard Reference Database 69: NIST Chemistry Webbook (http://webbook.nist.gov)* (National Insitute of Standards and Technology (NIST), Washington, DC, 2001).

[3] T. A. Gallagher, *Rydberg Atoms* (Cambridge University Press, Cambridge, 1994).

[4] S. Raouafi, Ph.D. thesis, Universite Paris XI, 2001.

[5] S. Raouafi, G. Jeung, and C. Jungen, J. Mol. Spec. **196**, 248 (1999).

[6] L. Berg *et al.*, Phys. Scr. **24**, 34 (1981).

[7] R. Mulliken, J. Am. Chem. Soc. **86**, 3183 (1964).

[8] D. Dill and C. Jungen, J. Phys. Chem. **84**, 2116 (1980).

[9] J. E. Murphy *et al.*, Phys. Rev. Lett. **65**, 1861 (1990).

[10] J. E. Murphy, Ph.D. thesis, Massachusetts Institute of Technology, 1992.

[11] J. M. Berg, J. E. Murphy, N. A. Harris, and R. W. Field, Phys. Rev. A **48**, 3012 (1993).

[12] N. A. Harris and C. Jungen, Phys. Rev. Lett. **70**, 2549 (1993).

[13] N. A. Harris and R. W. Field, J. Chem. Phys. **98**, 2642 (1993).

[14] Z. J. Jakubek, Ph.D. thesis, Massachusetts Institute of Technology, 1995.

[15] C. M. Gittins, Ph.D. thesis, Massachusetts Institute of Technology, 1995.

[16] N. A. Harris, Ph.D. thesis, Massachusetts Institute of Technology, 1995.

[17] S. F. Rice, J. Martin, and R. W. Field, J. Chem. Phys. **82**, 5023 (1985).

[18] R. W. Field and C. Gittins, J. Chem. Phys. **106**, 10379 (1997).

[19] T. Törring, W. E. Ernst, and S. Kindt, J. Chem. Phys. **81**, 4614 (1984).

[20] Z. J. Jakubek, J. Mol. Spec. **205**, 197 (2001).

[21] C. Gittins, N. Harris, M. Hui, and R. W. Field, Can. J. Phys. **79**, 247 (2001).

[22] J. Li *et al.*, J. Mol. Spec. **193**, 403 (1999).

[23] A. R. Skinner and D. W. Chandler, Am. J. Phys. **48**, 8 (1980).

[24] R. E. Smalley, L. Wharton, and D. H. Levy, Acc. of Chem. Rsch. **10**, 139 (1977).

[25] A. Kantrowitz and J. Grey, Rev. Sci. Inst. **22**, 328 (1951).

[26] M. D. Morse, Exp. Meth. Phys. Sci. **29B**, 21 (1996).

[27] J. H. Moore, C. C. Davis, and M. A. Coplan, *Building Scientific Apparatus: A Practical Guide to Design and Construction* (Addison Wesley, Reading, Ma, 1989).

[28] J. Hopkins, P. Langridge-Smith, M. Morse, and R. Smalley, J. Chem. Phys. **78**, 1627 (1983).

[29] O. Almen, W. Hartmann, K. Frank, and J. Christiansen, J. Phys. E: Sci. Inst. **22**, 382 (1989).

[30] B. E. optics Inc., *Burle Long-life MCP Selection Guide (http://www.burle.com)* (Burle Electro-optics Inc., Sturbridge, Ma, 2001).

[31] W. C. Wiley and I. H. McLaren, Rev. Sci. Inst. **26**, 1150 (1955).

[32] D. M. Lubman and R. M. Jordan, Rev. Sci. Inst. **56**, 373 (1985).

[33] R. M. J. Co., *Product Catalog 2001 (http://www.rmjordran.com)* (R. M. Jordan Co., Grass Valley, Ca, 2001).

[34] R. Signorell and F. Merkt, in *The Role of Rydberg States in Spectroscopy and Photochemistry*, edited by C. Sandorfy (Kluwer Academic Publishers, Amersterdam, 1999), p. 479.

[35] F. Merkt *et al.*, J. Phys. B: At. Mol. Opt. Phys. **31**, 1705 (1998).

[36] P. Stech, private communication.

[37] Lambda Physik, Inc., private communication.

[38] S. Gerstenkorn and P. Luc, *Atlas du Spectre D'Absorption de la Molécule D'Iode* (Centre National de la Recherche Scientifique, Paris, 1978).

[39] M. Duncan, private communication.

[40] S. Arepalli, N. Presser, D. Robie, and R. J. Gordon, Chem. Phys. Lett. **118**, 88 (1985).

[41] C. E. Moore, *NBS Standard Reference Data Series 35: Atomic Energy Levels As Derived From the Analyses of Optical Spectra Vol. 1* (U.S. Government Printing Office, Washington, DC, 1971).

[42] V. S. Letokhov, *Laser Photoionization Spectroscopy* (Academic Press, Inc., Orlando, Fl, 1987).

[43] D. C. Jacobs, R. J. Madix, and R. N. Zare, J. Chem. Phys. **85**, 5469 (1986).

[44] J. C. Miller and R. N. Compton, J. Chem. Phys. **84**, 675 (1986).

[45] M. Hippler and J. Pfab, Chem. Phys. Lett. **243**, 500 (1995).

[46] S. Panov (unpublished).

[47] K. P. Huber and G. Herzberg, *Molecular Spectra and Molecular Structure IV: Constants of Diatomic Molecules* (Van Nostrand-Reinhold, New York, 1979).

[48] V. L. Stakhursky (unpublished).

[49] S. Raouafi, G. Jeung, and C. Jungen, Submitted **XX**, XX (2002).

[50] G. Herzberg, *Molecular Spectra and Molecular Structure I: Diatomic Molecules* (Krieger, Malabar, Fl, 1986).

[51] L. Berg, L. Klynning, and H. Martin (unpublished).

[52] L. Berg, L. Klynning, and H. Martin, Phys. Scr. **21**, 173 (1980).

[53] A. Pereira, Phys. Scr. **34**, 788 (1986).

[54] G. Herzberg and C. Jungen, J. Mol. Spec. **41**, 425 (1972).

[55] P. Bündgen, B. Engels, and S. D. Peyerimhoff, Chem. Phys. Lett. **176**, 407 (1991).

[56] H. Lefebvre-Brion and R. Field, *Perturbations in the Spectra of Diatomic Molecules* (Academic Press, Orlando, Fl, 1986).

[57] J. T. Hougen, *NBS Monograph 115* (U.S. Government Printing Office, Washington, DC, 1970).

[58] I. Kovács, *Rotational Structure in the Spectra of Diatomic Molecules* (Elsevier, New York, 1969).

[59] C. Jungen and E. Miescher, Can. J. Phys. **47**, 1769 (1969).

[60] J. Tellinghuisen, Adv. Chem. Phys. **60**, 299 (1985).

[61] P. J. Dagdigian, H. W. Cruise, and R. N. Zare, J. Chem. Phys. **60**, 2330 (1974).

[62] C. Jungen and A. L. Roche, Can. J. Phys. **79**, 287 (2001).

[63] M. Arif, C. Jungen, and A. L. Roche, J. Chem. Phys. **106**, 4102 (1997).

[64] C. Jungen, *Molecular Applications of Quantum Defect Theory* (Institute of Physics Publishing, Bristol, 1996).

Appendix A

Data Acquisition Filetypes

These input files are used by the program SPSCAN developed by Dr. Sergey Panov to control the data collection process. A sample output file is also provided here. For a detailed description of the data acquisition procedure, see Section 2.2.8.

File *scanrc*:

```
#————————————
# test iodin + CaCl scan (V=600)
# —————————————
average = 40                    %number of shots that scope will average
steps = 2168                    %number of steps in Scanmate Burstscan mode
range = 603.5:610                   %scan range in nm
```

File *gatesrc*:

```
# ——————————————————————
# Ca(A1), CaCl 35(A2), CaCl 37(A3), I_2(B1)
# ——————————————————————
A_gates = 3                    %number of mass gates for scope channel A
B_gates = 1                    %number of mass gates for scope channel B
A_gate1 = 9.29e-6:9.35e-6          %start and stop time for chan. A mass gate 1
A_gate2 = 10.93e-6:11.00e-6           %start and stop time for chan. A mass gate 2
A_gate3 = 11.43e-6:11.56e-6          %start and stop time for chan. A mass gate 3
A_background = 9.7e-6:10.2e-6           %start and stop time for chan. A background gate
B_gate1 = 9.18e-6 : 10.28e-6          %start and stop time for chan. B mass gate 1
B_background = -2.6e-7 : 0.9e-7           %start and stop time for chan. B background gate
```

Sample Datafile - abridged

Jul 31 17:44:43
#————————————————
Ca(A1), CaCl 35(A2), CaCl 37(A3), I_2(B1)
————————————————————
——————————————————-
test iodin scan (V=600)
——————————————————-
#
Gates Settings
#
A_gates = 3
B_gates = 1
A_gate1 = 7.63e-06 : 7.76e-06
A_gate2 = 1.045e-05 : 1.055e-05
A_gate3 = 1.06e-05 : 1.07e-05
A_bckgr = 9.84e-06 : 1.036e-05
B_gate1 = 1.85e-07 : 2.25e-07
B_bckgr = 3e-08 : 0.7
#
Scan Settings
#
average = 40
steps = 501
range = 710 : 710.5
#
LeCroy
#
Channal A time = 5.515e-06 : 1.5525e-05
Channal B time = -8.45e-07 : 9.165e-06
#
Laser A1 A2 A3 B1
#
710.00000 -436.636 -23.4751 211.51 45881.6
710.00100 -258.226 -19.7191 -181.462 48735
710.00200 -294.612 -16.902 -53.5231 52908.3
710.00299 240.032 109.511 72.8901 51714.3
710.00399 -270.55 72.1858 -4.10814 51981.3
710.00499 26.4094 297.077 278.766 53766.6
710.00599 -150.24 -345.083 -55.1664 55403.1
710.00699 36.9732 148.949 185.57 58992.7
710.00798 -339.801 140.733 354.356 53057.1
710.00898 -71.5989 -130.756 -72.7727 51206.9
710.00998 -50.4714 278.884 342.971 45736.7

710.01098 -266.442 91.5527 -21.3623 35360.7
710.01198 -241.793 -122.305 -103.995 25957.4
710.01297 -509.409 -155.405 49.0629 21273
710.01397 -352.126 146.719 -192.026 17973.3
710.01497 62.7958 20.0712 -135.568 16512.3
710.01597 -349.192 -411.4 -469.384 16897.5
710.01697 -72.7727 31.2218 342.501 18633.2
710.01796 -251.183 -60.8004 235.22 20418.5
710.01896 75.1202 235.455 119.488 24202.7
710.01996 -318.087 145.076 -205.876 26811.9
710.02096 -41.0814 -133.338 -191.322 28860.4
710.02196 -355.06 -173.363 -75.7071 34918.2
710.02295 -338.041 250.714 49.2976 42925.2
710.02395 -184.866 227.591 -181.345 49543.7
710.02495 -311.631 -159.044 -162.095 58626.5
710.02595 -118.549 315.505 -17.1368 60385.1
710.02695 -227.121 88.1489 185.805 62139.8
710.02794 -443.679 -28.1701 289.213 62651
710.02894 -818.693 -419.147 -104.816 61895.7
710.02994 -306.35 -248.601 26.0573 48960.1
710.03094 -508.822 -259.047 149.888 48738.8
710.03194 -650.846 -547.791 -349.426 48662.5

Curriculum Vitae

BIRTH DATE: December 8, 1972.

EDUCATION: Vanderbilt University, BA *magna cum laude with High Honors* (1995); Massachusetts Institute Of Technology, Ph.D. expected February 2002.

AWARDS AND HONORARY SOCIETIES: Goldwater Foundation Fellowship, 1995; Phi Beta Kappa; Omicron Delta Kappa; Senior Research Award, Chemistry Department, Vanderbilt University, 1995; Breckenridge Scholarship, Vanderbilt University, 1995.; D. E. Pearson Award, Vanderbilt University, 1995; T.W. Martin Award, Vanderbilt University, 1995.

PUBLICATIONS AND PRESENTATIONS:

Li Li, X. Dai, Y. Liu, J. O. Clevenger, R. W. Field, G.-H. Jeung, N. Geum, and A. M. Lyyra. and "The Predissociation of the $1^3\Sigma_g^-$ state of ^{7}Li$_2$." Journal of Molecular Spectroscopy, 205, 139 (2001).

X. Dai, J. O. Clevenger, Y. Liu, Min Song, J. Shang, D. Chen, R. W. Field, and Li Li. "The $2\,^3\Delta_g$ State of Li$_2$." Journal of Molecular Spectroscopy 200, 120-122 (2000).

J. O. Clevenger, N. A. Harris, R. W. Field, and J. Li. "The Predissociation Mechanism for $^2\Sigma^+$ Rydberg States of CaCl." Journal of Molecular Spectroscopy 193, 412 (1999).

J. O. Clevenger and J. Tellinghuisen. "The B $\rightarrow$ X Transition in XeBr." Journal of Chemical Physics 103, 9611 (1995).

J. O. Clevenger and J. Tellinghuisen. "High-resolution Spectroscopy with a CCD-array Detector. The B $\rightarrow$ X Transition in XeBr." Chemical Physics Letters 231, 515 (1994).

J. O. Clevenger, Q. P. Ray, X. Zheng, M. C. Heaven, and J. Tellinghuisen. "Spectroscopy of Metastable Species in a Free-Jet Expansion: The b $\leftarrow$ A Transition in IBr." Canadian Journal of Physics 72, 1294 (1994).

D. T. Radzykewycz, C. D. Littlejohn, M. B. Carter, J. O. Clevenger, J. M. Purvis, and J. Tellinghuisen. "The $D' \rightarrow A'$ Transition in IBr: A Deperturbation Analysis." Journal of Molecular Spectroscopy 166, 287 (1994).

Presented research at conferences and symposia in USA, Canada, Japan, France, and China.